Single-electron wave packets for quantum metrology: concepts, implementations, and applications

Vyacheslavs Kashcheyevs
Departments of Physics, University of Latvia, Riga LV-1002, Latvia

Pascal Degiovanni[1] and Benjamin Roussel[1,2]
[1] *Univ. Lyon, ENS de Lyon, Université Claude Bernard Lyon 1, CNRS, Laboratoire de Physique, F-69342 Lyon, France and* [2] *Department of Applied Physics, Aalto University, 00076 Aalto, Finland*

Masaya Kataoka and Jonathan D. Fletcher
National Physical Laboratory, Hampton Road, Teddington, Middlesex TW11 0LW, United Kingdom

Lars Freise and Niels Ubbelohde
Physikalisch-Technische Bundesanstalt, Bundesallee 100, 38116 Braunschweig, Germany

Gwendal Fève and Hugo Bartolomei
Laboratoire de Physique de l'Ecole normale supérieure, ENS, Université PSL, CNRS, Sorbonne Université, Université de Paris, Paris, France

François Couëdo, Aleksandr Kadykov and Wilfrid Poirier
Laboratoire national de métrologie et d'essais, 29, avenue Roger Hennequin, 78197 Trappes, France

Preden Roulleau and François D. Parmentier
Université Paris-Saclay, CEA, CNRS, SPEC, 91191, Gif-sur-Yvette, France

Frank Hohls
Physikalisch-Technische Bundesanstalt, Bundesallee 100, 38116 Braunschweig, Germany

(Dated: February 28, 2022)

Harnessing the quantum properties of single-electron wave packets for quantum metrology has been the goal of the European EMPIR research project SEQUOIA (17FUN04). This encompassed the further development of concepts and theoretical methods of electron quantum optics as well as the development of new experimental methods and techniques for and demonstrations of single-electron-based quantum metrology. This white paper provides an educational introduction into the state-of-the-art theoretical concepts and methods of electron quantum optics as the foundation for single-electron wave packet quantum metrology. Furthermore, it showcases new techniques and applications, to be used in and to inspire both basic research and quantum metrology and technology applications.

EMPIR
EURAMET
The EMPIR initiative is co-funded by the European Union's Horizon 2020 research and innovation programme and the EMPIR Participating States

SEQUOIA

EMPIR project SEQUOIA (17FUN04)

Coordinator contact: Frank Hohls, email: Frank.Hohls@ptb.de

Project website: `https://www.ptb.de/empir2018/sequoia/home/`

CONTENTS

INTRODUCTION

The development of scalable quantum technology is of particular importance for applications such as quantum computation and simulation. Semiconductor quantum devices promise good potential for scaling up and the practical realisation of integrated quantum circuitry. They also form a natural platform for the realisation of in-situ quantum sensors for electrical properties in technology applications. Recent years have seen large efforts to harness the quantum properties of single or few electrons for quantum technologies [1, 2], largely devoted to electrons that are spatially localized at a physical site, *e.g.* in a quantum dot or a dopant in a semiconductor nanostructure. Single electrons have also been moved in a controlled manner between such sites, typically by effectively moving a quantum dot confinement potential, e.g., by potentials induced by surface acoustic waves [3] or by changing the gate voltages in quantum dot arrays [4, 5]. This white paper offers an introduction to a so far less researched unique hardware resource for potential quantum advantage: the controlled generation, manipulation, interaction, and measurement of single-electron wave packets targeting the quantum state of their continuous degree of freedom. The basic-science foundations for this field have been inspired by analogies with photonic quantum optics and have been named solid-state electron quantum optics [6]. Exploring and extending the potential of electron quantum optics for quantum metrology has been the goal of the European research project SEQUOIA (17FUN04), carried out within the European Metrology Programme for Innovation and Research (EMPIR). The physical idea behind the project is to use the extreme sensitivity of charged particles to their electromagnetic environment to design quantum sensors of the electromagnetic field and to develop quantum metrology for single electrons. In this perspective, the SEQUOIA project sets out to extend the range of experimental and theoretical methods, protocols and applications available for single-electron wave packet technologies, spanning several orders of magnitude in energy, and also the exploring the potential of a new material platform, graphene, in addition to the most researched so far GaAs semiconductor platform. Starting with a fundamental connection of a single-electron quantum mechanics to electrical metrology (section I), and drawing from the results of the project SEQUOIA, this white paper offers an extensive educational introduction to the concepts of electron quantum optics, providing the theoretical tools needed to describe, characterize and harness the coherence of single-electron wave packets (section II). This is followed by showcasing a collection of different technologies and applications of single-electron wave packet quantum metrology (section III) and quantum sensing (section IV), all developed within the project SEQUOIA, that demonstrate and inspire further use and uptake of single-electron quantum optics techniques in quantum metrology and quantum technology.

I. THE QUANTUM OF ELECTRICITY: SINGLE-ELECTRON PHYSICS IN ELECTRICAL METROLOGY

Masaya Kataoka and Vyacheslavs Kashcheyevs

Electrical measurements are ubiquitous processes that are essential in our modern human life. One can make a long list of examples such as smart meters monitoring your electrical usage at home, tyre pressure sensors on your car, touch screen sensors on your smartphones, and so on. The development of new measurement methods expanding measurement ranges (e.g. magnitude and frequency) and their usage scene (e.g. miniaturisation) have been continuously improving the quality of our life. In exploring new technologies for advanced electrical measurement, it is important to be aware that all electrical phenomena arise from the movement and interactions of individual elementary charged particles, such as electrons. Developing single-electron transport technologies opens up new opportunities to harness the fundamental physical phenomena for practical applications.

One example of such application is to establish a new traceability in electrical metrology. For electrical measurements to be meaningful, the measured electrical quantities must be traceable to the definition of electrical units. Prior to 2019, the realisation of electrical units was based on conventional units, under international agreement adopted in 1990 [7], to use the Josephson effect [8] and quantum Hall effect [9] as primary quantum standards for the realisation of volt and ohm. (With regard to the ampere, while it is one of the seven base units in SI, accurate quantum standards based on single-electron transport have not been realised yet.) Primary standards were maintained by national metrology/measurement institutes (NMIs) and electrical units were disseminated to end users through traceable chains provided by calibration laboratories. Following the redefinition of SI units in 2019 [10], the ampere is now defined in terms of the fixed value of elementary charge e. The volt and ohm are also defined in terms of the fundamental constants e and h (Planck constant). While these changes have barely affected how electrical units are currently realised by the Josephson and quantum-Hall experiments at NMIs, this new SI opens up new possibilities in electrical metrology. Since the definition of electrical units is no longer tied to a particular realisation experiment, we can envisage a creation of new types of primary standards as long as the new methods follow the definition of SI units [11, 12]. These new primary standards do not necessarily have to sit within NMIs. The traceability chain can start from anywhere in the world, or even from the space (e.g. on the satellite, on the Moon, or on Mars...). While the existing primary standards, that require to be cooled down at least to a liquid helium temperature and require a large magnetic field, may be impractical for such extreme applications, a new class of primary standards could be developed, which may not achieve the ultimate accuracy of the existing standards, but offer relaxed operation requirements. For example, a device (current/voltage/resistance standard) achieving the accuracy of 1 part in 10^5 may not be suitable for use as a primary standard at an NMI, but if it can be operated at a relatively high temperature (e.g. 77 K), it could be placed on a satellite providing in-situ calibration in order to prolong the lifetime of detectors [13].

In order to show the background behind this vision, in this section, we will describe the fundamental single-electron transport that ultimately forms the basis of all electrical conductivity. We show that all three electrical units, volt, ohm, and ampere, can be derived from this phenomenon without considering the intricate physics of Josephson and quantum Hall effects. The following three equations link the current I, voltage V, and resistance R to clocked single-electron transfer at frequency $f_{\rm s}$, Josephson effect under microwave radiation with frequency $f_{\rm J}$, and quantum Hall effect:

$$I = ef_{\rm s}, \tag{1}$$

$$V = \frac{f_J}{2e/h}, \tag{2}$$

$$R = \frac{h}{e^2}. \tag{3}$$

This link is often called a quantum metrological triangle [14]. These three equations form the basis of present electrical metrology and describe the operation of primary standards. In the following, we show that we can deduce these equations (or their equivalent ones) without invoking the Josephson and quantum-Hall physics.

We consider a system of a conductor connecting two reservoirs as shown in Fig. 1(a) [15–19]. We do not fix the nature of the conductor such as its dispersion relation, but we assume that there is a single mode in the transverse direction (y) to the current flow in x direction (an example is one-dimensional conductor with only the lowest subband occupied). We also ignore electron spin and assume that the conductor is a spin-less system. The left and right reservoirs are biased by voltages V_1 and V_2, respectively ($V_1 < V_2$). The energy structure of this system in the x direction of is illustrated in Fig. 1(b). The potential energy of the left contact is raised by $-eV = -e(V_1 - V_2)$. We consider the zero-temperature limit, and the left contact emits electrons within this energy window $-eV$. Now, since the energy is merely the frequency scaled by the Planck constant, i.e. $E = hf$, we can redraw Fig. 1(b) in the frequency domain as shown in Fig. 1(c) using $f_j = -eV_j/h$ ($j = 1$ or 2). We write the wavefunction of the state at frequency f in the time

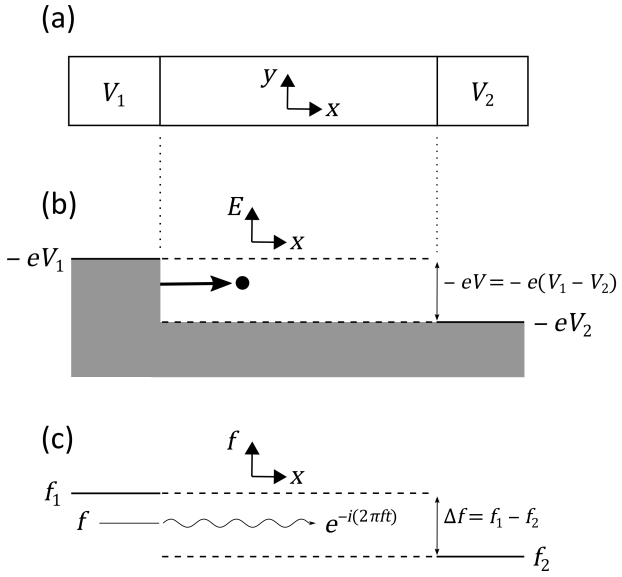

FIG. 1. (a) One-dimensional perfect conductor connected to two reservoirs at potentials V_1 and V_2 ($V_2 > V_1$). (b) The excess current arising from the unbalance of chemical potentials between the two reservoirs involves single electron states with energies in the $[-eV_2, -eV_1]$ interval. (c) It can be described in terms of a maximally compact train of Martin Landauer Shannon wave packets with $h\Delta f = e(V_2 - V_1)$ (see Fig. 2).

domain as $\psi_f(t) \propto e^{-i(2\pi ft)}$. We then consider one-electron wavefunction as a superposition of these states within the bandwidth $\Delta f = f_1 - f_2$ as

$$\Psi(t) = \frac{1}{\sqrt{\Delta f}} e^{i\pi(f_1+f_2)t} \int_{f_2}^{f_1} \psi_f(t)\, df, \tag{4}$$

$$= \frac{\sin(\pi \Delta f t)}{\pi t \sqrt{\Delta f}}. \tag{5}$$

This wavefunction takes a form of Shannon-Martin-Landauer wave packet [21, 22] as shown by the solid line in Fig. 2(a). We define a timescale τ as a minimal time such that a copy of the wave packet shifted by τ [dashed line in Fig. 2(a)] is orthogonal to the original, i.e.

$$\int_{-\infty}^{+\infty} \Psi^*(t)\Psi(t-\tau)dt = 0 \Rightarrow \tau = (\Delta f)^{-1} \tag{6}$$

This state can be interpreted as an electron wave packet, emitted from the contact into the conductor, travelling in the x direction and becoming orthogonal after the time duration τ. The Wigner function of $\Psi(t)$ is defined as

$$W(f,t) = \int_{-\infty}^{+\infty} \Psi^* \left(t - \frac{\delta_t}{2}\right) \Psi \left(t + \frac{\delta_t}{2}\right) e^{-2\pi i f \delta_t} d\delta_t = \frac{\sin[2\pi(\Delta f - 2|f|)]}{\pi t \Delta f} \tag{7}$$

Fig. 3 is a plot of this Wigner distribution function in terms of $t\,\Delta f$ and $2\pi f/\Delta f$. It shows that the Wigner function is zero outside the energy band and that it decays in time beyond it. Oscillations ensure the orthogonality of two wave packets that are translated by a multiple of $\tau = (\Delta f)^{-1}$. Note that $\iint W\, df\, dt = \iint W^2\, df\, dt = 1$ which suggests to associate each of these wavefunction to a rectangular cell of unit area in the frequency-time phase space, *i.e.* reflecting the fact that $\Delta f \cdot \tau = 1$ [see the grey-filled box in Fig. 2(b)]. The neighbouring state, shifted by τ, associated with the dashed box in Fig. 2(b), corresponds to the orthogonal state $\Psi(t-\tau)$ introduced in Fig. 2(a). This fundamental process forms a basis of electron transport, and can be called as the "quantum of electricity". In the maximum occupancy limit, this process is repeated at a rate of $\Delta f = 1/\tau$, and the electron wave packets $\Psi_n(t) = \Psi(t - n\tau)$, where n is an integer, are emitted one by one periodically as shown in Fig. 2(d). In the frequency-time phase space, electrons fill up the bandwidth of Δf following the Pauli principle [Fig. 2(d)]. Mathematically, the quantum saturation of the current within the voltage bias window is expressed by the identity satisfied by the Wigner representation (7) of the Shannon-Martin-Landauer wavelets, $\sum_n W(f, t - \tau\, n) = 1$ for $f \in [-\Delta f/2, +\Delta f/2]$ and zero otherwise. As a result, the current produced is $I = e/\tau = e\Delta f$.

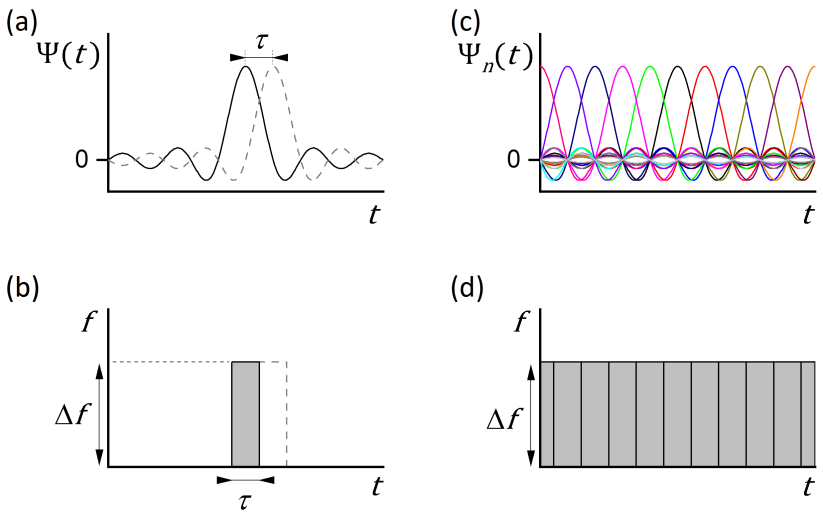

FIG. 2. Cellular decomposition of the phase plane associated with Martin-Landauer-Shannon wave packets: (a) Two Martin Landauer Shannon wave packets translated by $\tau = (\Delta f)^{-1}$ are orthogonal, (b) Each of these wave packets is associated with a rectangle of unit area in the (f, t) plane (see also Fig. 3), (c) Visualization of the wavefunctions of many Martin Landauer Shannon wave packets translated by $\tau = (\Delta f)^{-1}$, (d) Equivalent representation in the (t, f) plane.

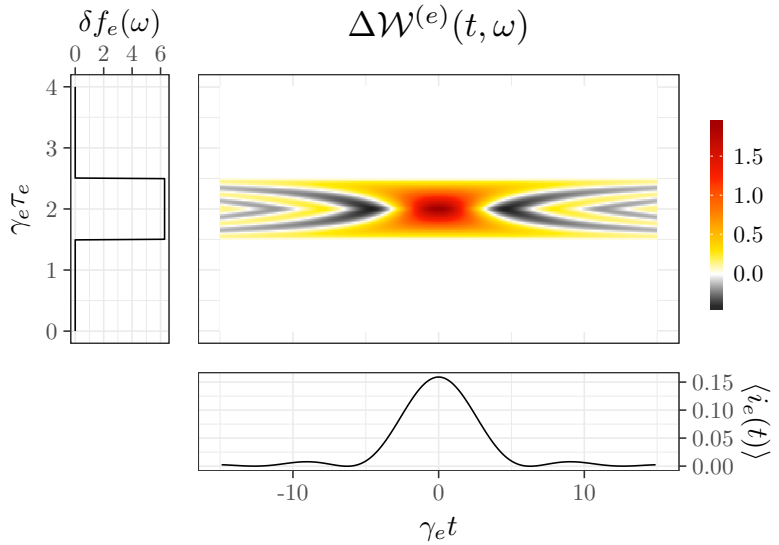

FIG. 3. (Figure reproduced from [20]) Wigner representation of a Shannon–Martin–Landauer wave packet. Note the typical sinc^2 current shape. The Wigner function spreads close to the boundaries of the energy window of width hf as a consequence of the Heisenberg time/energy uncertainty relation. The marginal distributions correspond to the avertage time dependent current and electron distribution function associated with this single electron wave packet.

Now, rewriting Δf as f and recalling that $-eV = hf$, we can produce three equations equivalent to Eqs. 1-3:

$$I = ef, \tag{8}$$

$$V = \frac{f}{e/h}, \tag{9}$$

$$R = \frac{V}{I} = \frac{h}{e^2}. \tag{10}$$

The only difference is an omission of a factor of 2 in Eq. 9 due to the difference in the type of carriers (electrons with charge $-e$ versus Cooper pairs with charge $-2e$). Note that we did not introduce the physics of Josephson effect or quantum Hall effect in the derivation of Eqs. 8-10. What this shows is that the fundamental physics of single-electron transport includes all necessary ingredients to realise the three electrical units from fundamental constants [15–19]. One can expect that the control and measurement of single-electron dynamics would provide fundamental tools in electrical metrology. Furthermore, such a single-electron-based metrology tools could tap into the measurement ranges (e.g. in terms of signal strength and bandwidth) that are not attainable by Josephson or quantum Hall systems.

One example of this is an exploitation of ultra-short electron wave packet [23]. When a short voltage pulse $V(t)$ is applied to a conductor (single-mode as in the one shown in Fig. 1), the number of charged particles excited depends on the phase accumulated during the voltage pulse. The resulting excited charge becomes $Q = Ne$ with an integer N if the phase $2\pi\frac{e}{h}\int_{-\infty}^{+\infty} V(t)dt$ is an integer N multiple of 2π [24–26]. This description can be expressed by the following three equations:

$$Q = Ne, \tag{11}$$

$$\int_{-\infty}^{+\infty} V(t)dt = N\frac{h}{e}, \tag{12}$$

$$\frac{\int_{-\infty}^{+\infty} V(t)dt}{Q} = \frac{h}{e^2}. \tag{13}$$

Above equations can be interpreted as an ac version of Eqs. 8-10. We can see that the link between the charge, the integral of voltage pulse, and fundamental constants h and e is maintained in the ac domain. The state of the art technologies can generate voltage pulses and single-electron wave packets as short as a few picoseconds. This gives a scope for establishing SI tracability at such a fast timescale. Moreoever, these fast pulses/wave packets could be used for sensing electromagnetic fields at fast timescales, using interferometry (such as in Mach-Zehnder geometry [27]).

This prospect calls for deep understanding of single-electron transport physics. Electron quantum optics is a tool to study such physics, as well as providing methods for metrological and quantum-sensing applications.

II. THEORETICAL CONCEPTS OF ELECTRON QUANTUM OPTICS

Pascal Degiovanni, Benjamin Roussel and Vyacheslavs Kashcheyevs

Definition, characterization and exploitation of single-electron properties of electrical current calls for a consistent theoretical framework that properly incorporates the basic notions of quantum many-body physics. We cannot underestimate the extent to which it is necessary for theory to provide predictions and guidance for the design of experimental implementations of single-electron devices. Our proposal for a coherent theoretical framework is motivated by the knowledge that the sensing and quantum information processing capabilities that may be possible with single electron technologies cannot be arrived at by experimentation alone. For example, the creation of elementary excitations using voltage pulses alone is a sufficiently unexpected result that this could not have been anticipated to arise without predictions based on the exact accumulation of the phase of electrons for pulses of a very specific shape. The decoherence of quasiparticles in edge states via charge fractionalisation is a similarly subtle phenomenon, one that is related to the fundamental physics of interactions the quantum Hall regime and of real relevance to the limitations on coherent transport in practical single electron optics implementations.

The electrical current as a flow of individual electrons is conceptually similar to the the beam of light as a collection of photons. Section II A captures this analogy rigorously and defines the core theoretical concept of electron quantum optics — the notion electronic coherence (correlation) functions. The most relevant components of electron coherence are classified in Section II B: (i) a uniform coherent flow, defined by a constant and sharp Fermi energy, forms a background with respect to which electron and hole excitations can be created; (ii) these excitations contribute to the excess first order coherence of electron, hole and electron-hole types; and (iii) intrinsic two-particle coherence, which is crucial for HOM-based interferometry.

The excess first order (single-electron/hole) coherence $\Delta\mathcal{G}^{(e)}$ stands out as the key quantity characterizing electronic waves, and Section II C is devoted to different representations of $\Delta\mathcal{G}^{(e)}$. As function of two times, $\Delta\mathcal{G}^{(e)}$ describes correlations in the quantum amplitude at a fixed reference cross-section of the conductor, as the electronic excitations travel through. As function of two spatial coordinates, $\Delta\mathcal{G}^{(e)}$ captures spatial coherence at a frozen moment in time and can be expressed in terms of real-space electron wavefunctions. Section II C explains equivalence between these two pictures and introduces the Wigner representation for both. Wigner representation of excess coherence in time-frequency domain, already sketched in Figs. 2 and 3 for the special case of Shannon-Martin-Landauer wave packet, offers a visual generalization to the quantum domain of the intuitive notions of time-dependent current and voltage. Interpreted in the language of spatial coherence, the same pictures relate quantitatively to the statistical distribution of electrons as point particles in phase space (Wigner quasi-probability distribution) and the density matrix of quantum statistical mechanics. These concepts, along with illustrative examples of electronic Wigner distributions are explained in Section II C 1.

Unlike amplitude of an optical (bosonic) field, $\Delta\mathcal{G}^{(e)}$ is limited in magnitude by the Pauli principle which prohibits occupation of the same spatio-temporal mode by more than one particle. (We have already sketched out in Section I how this principle leads to the quantum electrical metrology relations). Hence decomposition of a general multi-electron $\Delta\mathcal{G}^{(e)}$ into orthogonal modes or "atoms of signal" is an important instrument for representing electronic coherence, as discussed in Section II C 2, which is based on the recently introduced perspective on electron quantum optics as "quantum signal processing" [28, 29].

Having established the language of electron coherences and Wigner distributions to describe the quantum state of electrical current, we examine in Section II D how this state is transformed as the electron wave packets propagate through circuit elements. We focus first on interactions-free coherent propagation which can be described as linear unitary transformation of electronic coherence, starting with free propagation and dispersion (Section II D 1), discuss different representations of the general time-dependent single-particle scattering (Section II D 2), and the important case of photoassisted propagation (Section II D 3). These theoretical instruments are then used in Section II D 4 to discribe modulation of the Fermi sea by time-dependent voltages, and introduce an important class of single-electron excitations: the quantized Lorentzian pulses or levitons.

In Section II E we use the formalism of electron quantum optics to describe the working principles of three quantum devices: (i) electronic Mach-Zehnder interferometer; (ii) modulated energy-selective beamsplitter, and (iii) Hong-Ou-Mandel two-particle interferometer. Section II E describes the idealized models of these devices in a unified way as "quantum signals processors": local time-dependent electrical and/or magnetic fields determine a coherent transformation of the single-electron wave packets such that the relevant information becomes accessible to a macroscopic measurement.

We conclude the discussion of the theoretical framework by an overview of interaction effects in Section II F. First we consider of capacitive interaction between two electronic wave packets and derive estimates for phase-sensitive and single-shot interactions-based sensing in Section II F 1. This is followed by a brief review of interaction-induced decoherence in the context of electron quantum optics in Section II F 2. Finally, we explain how considerations of capacitive interaction naturally lead to the idea of using electronic interferometers for probing rapidly varying electromagnetic fields, and briefly sketch open theoretical challenges in this direction in the concluding Section II F 3.

Again we emphasize that the creation of an expanding toolkit of measurement techniques (Section III) and delivery of quantum-enabled sensing capability (Section IV) directly relies on our success in capturing the physics of elementary excitations and properly formulating very fundamental question about the nature of electricity at its most 'granular' level.

A. How to describe a quantum coherent beam of electrons?

From a quantum technologies perspectives, on-demand single to few electron sources generate a quantum beam of electricity with controlled many-body state, involving only one to few electronic or hole excitations on top of the reference state. Depending on the experimental context, this reference state could be a Fermi sea at a given reference chemical potential as in many experiments performed in edge channels of the integer quantum Hall effect [6] but it could also an empty band of a depleted wave-guide as in experiments with on demand single electron excitations in the meV range [30–32], or experiments conducted in depleted 1D quantum wires [3, 33–35].

Characterizing this many-body state is a difficult experimental problem and, whenever interactions play an important role, even theoretically, but an operational characterization via experimentally accessible correlators can be envisioned. This approach is very similar to the one developed and promoted by Glauber in his pioneering work on electron quantum optics [36–38].

Exactly as in photonic quantum optics, the idea is to describe a quantum electron beam through correlation functions of elementary excitation creation and destruction operators. However, because electrons are fermions, the

parity superselection rule applies and drastically reduces the number of correlators. This rule, originally formulated in relativistic quantum field theory [39], which can indeed be derived from the no-signaling principle [40], states that for fermions there is no quantum coherences between quantum states with an odd difference of the total fermion number. In condensed matter, the BCS state involves quantum coherences between many-body states with electron numbers differing by 2. In a metal, such quantum superpositions are even not allowed: there are no coherences between many-body states of different fermion numbers.

As a consequence, the only non-vanishing correlation functions within a quantum electron beam are the Glauber coherences of the form

$$\mathcal{G}^{(Ne)}(X_1 \cdots X_N | X'_1 \cdots X'_N) = \mathrm{Tr}\left(\psi(X_N) \cdots \psi(X_1)\, \rho\, \psi^\dagger(X'_1) \cdots \psi^\dagger(X'_N)\right) \tag{14}$$

in which $X_k = (\mathbf{r}_k, t_k)$ denotes space time coordinates within the circuit under consideration (same for the X'_k) and ρ is the many-body density operator describing the state of the electron fluid. The $N = 1$ correlator is called the single electron coherence. Single electron coherence contains the information about all single electron wavefunctions present within the electron beam. Any single particle observable such as the electrical current and the heat current can be computed from single electron coherence. The $N = 2$ correlator is called the two-electron coherence and contains the information about all two-electron wavefunctions present in the electron fluid and gives access to all two-particle observables such as current or charge fluctuations, as well as heat current fluctuations.

It should be noted that such correlators are familiar in condensed matter physics: the commonly used Green functions [41] are defined as properly ordered two field correlators. For example, in the Schwinger-Keldysh formalism designed to deal with non-equilibrium physics [42], the correlator $G_\rho^{(+-)}(X, X') = -i\langle\psi(X)\,\psi^\dagger(X')\rangle_\rho = -i\mathrm{Tr}(\psi^\dagger(X')\,\rho\,\psi(X))$ corresponds to the first order coherence for holes in our language. In standard approaches to quantum transport [43], these Green functions are often interpreted as propagators, in terms of which theoretical techniques of many-body physics such as diagrammatic expansions, equations-of-motion hierarchies, and path integrals, can be applied. By contrast, in the approach presented here, we focus on these correlators as carriers of information on the many-body state of the system. The point of view adopted here is indeed closer to quantum optics blended, as we shall see, with the scattering approach of quantum transport developed by Markus Büttiker and his numerous collaborators across decades [44].

So far, this discussion is very general and could be used to describe any quantum beam of fermions. For example, Glauber himself, with Cahill had indeed introduced these notions at the end of last century in a somehow overlooked paper, having in mind cold gases of fermionic atoms [45]. Beyond the case of fermionic cold atoms, the introduction of electronic coherences is directly relevant for the emerging field of quantum electron microscopy, which exploits coherent beams of electrons propagating in vacuum to improve electronic microscopy [46, 47]. However, in this white paper, we will restrict ourselves to the study of quantum electrical currents which are quantum beams of electrons within a conductor.

In contrast to what happens in an electron microscope with all the electron sources switched off, the electron fluid in a usual metallic conductor is not in the true vaccuum state but, at zero temperature, in a reference vacuum state, which is a Fermi sea $|F_\mu\rangle$ at a given chemical potential as long as strong correlations such as the one present in the fractional quantum Hall effect are not present. Switching the current sources "on" introduces excitations on top of this Fermi sea which involve electronic or hole single particle excitations, depending on their energies with respect to the Fermi energy. This is the typical situation encountered within quantum Hall edge channels: at low temperature and high enough magnetic field, a 2DEG becomes a bulk-insulator and conduction happens at the edges which then play the role of 1D conductors with ν conduction channels, where $\nu \in \mathbb{N}^*$ denotes the filling fraction of the corresponding integer quantum Hall phase. Because the energy of excitations with respect to the Fermi level is typically of the order of μeV in these experiments (see [6, 48] for a review), only one to two orders of magnitude above from $k_B T_{\mathrm{el}}$ where $T_{\mathrm{el}} \simeq 10$ to 100 mK, these situations are often referred as *low energy electron quantum optics*.

However, electron quantum optics experiments have also been performed with on-demand injection of electron into otherwise empty edge states of a 2DEG with the Fermi sea far removed in energy and/or real space away from the ballistic wave packet [30, 32, 49, 50]. In this case, the electrical current is much more similar to the electron beam of an electronic microscope: electrons are only present when the source is switched "on". In these experiments, the electronic excitations are propagating alone, without the Fermi sea, and are therefore called "solitary excitations". In some part of the sample, the electronic system is not fully depleted but electronic excitations are propagating at a much higher energy (typically tens of meV) from the Fermi level than in "low energy" quantum optics experiments. This is the domain of *high energy electron quantum optics* experiments.

B. Electronic coherences

1. Single and two electron coherences of Slater determinants

To begin with, let us consider the case where the reference state is the vacuum state $|\emptyset\rangle$. We consider that an N-electron Slater determinant has been introduced in the system at time $t = 0$, based on N mutually orthogonal[1] normalized wave packets $\varphi_1, \cdots, \varphi_N$:

$$|\Psi_N\rangle = \prod_{k=1}^{N} \psi^\dagger[\varphi_k] \; |\emptyset\rangle \; . \tag{15}$$

Denoting by $\mathcal{G}^{(e)}_{|\Psi_N\rangle,t=0}(x|y)$ the equal time single electron coherence taken at $t = 0$, a straightforward computation leads to:

$$\mathcal{G}^{(e)}_{|\Psi_N\rangle,t=0}(x,x') = \sum_{k=0}^{N} \varphi_k(x)\, \varphi_k(x')^* \tag{16}$$

The single electron coherence therefore appears as the sum of the contributions of each of the individual electronic wavefunction involved in the state $|\Psi_N\rangle$. Each wavefunction φ_k contributes by $\varphi_k(x)\varphi_k(x')^*$, thereby showing that information on the phase of the wavefunction $\varphi_k(x)$ is present for $x \neq x'$.

It is interesting to use this to compute the single electron coherence within a Dirac sea corresponding to an infinite filling of single electron plane wave $\varphi_k(x) = e^{ikx}$ along a line from $k = -\infty$ to $k = k_F$. A similar computation leads to the following expression:

$$\mathcal{G}^{(e)}_{F,t=0}(x,x') = \frac{1}{2\pi} \frac{e^{ik_F(x-x')}}{x'-x+i0^+} \, . \tag{17}$$

The same quantity can also be computed for the equilibrium state of these fermions, at a chemical potential $k_F(\mu)$ dependent on the chemical potential μ and electronic temperature $T_{\rm el}$:

$$\mathcal{G}^{(e)}_{\mu,T_{\rm el},t=0}(x,x') = \frac{1}{2\pi l_{\rm th}(T_{\rm el})} \frac{e^{ik_F(\mu)(x-x')}}{\sinh\left(\frac{x'-x}{l_{\rm th}(T_{\rm el})}+i0^+\right)} \, . \tag{18}$$

which now reveals the thermal coherence length $l_{\rm th}(T_{\rm el}) = \hbar v_F/k_B T_{\rm el}$ of the electrons at non-zero temperature $T_{\rm el}$. The $1/T_{\rm el}$ dependence of this coherence length can be traced back to the linear dispersion relation of the fermions close to the Fermi point. By contrast, when considering non-relativistic particles with dispersion relation $E(k) = \hbar^2 k^2/2m$ at vanishing chemical potential, the corresponding coherence length would exhibit the scaling of the De Broglie thermal length $l_{\rm dB}(T_{\rm el}) = h/\sqrt{2\pi m k_B T_{\rm el}}$.

2. Single and two electron coherences the presence of a Fermi sea

Let us now turn to the case of usual metallic conductors in which excitations are present within the electron fluid on top of this reference vaccum state $|F_\mu\rangle$. These corresponds to the excitations emitted by the electron sources present in the circuit when they are switched on at zero temperature. As of now, only first order electronic coherence has been measured within a quantum conductor [32, 51, 52] and only second order electronic coherence seems to be within reach of experimental characterization [53], we will therefore focus the discussion on these quantities with a stronger emphasis on single electron coherence.

At the single particle level, the appropriate notion that contains information on the single particle excitations is the excess single electron coherence $\Delta_0\mathcal{G}^{(e)}(X_1|X_1')$ defined by

$$\mathcal{G}^{(e)}_\rho = \mathcal{G}^{(e)}_{|F_\mu\rangle} + \Delta_0\mathcal{G}^{(e)}_\rho \tag{19}$$

---

[1] This condition is indeed quite generic: because of the fermionic statistics, any Slater determinant can be seen as built from mutually orthogonal wave packets.

Before moving to the discussion of simple examples, let us make the kinematic framework more specific. Within quantum conductors and circuits, we are usually interested in local observable measured at a given spatial position, such as for example current correlators. It is therefore common to fix the position x within the conductor or circuit and consider the electronic coherence at this position but at various times. We thereby introduce the "local" single electron coherence $\mathcal{G}^{(e)}_{\rho,x}(t,t') = \mathcal{G}^{(e)}_{\rho}((x,t)|(x,t'))$. Sometimes, the spin degree of freedom or some orbital degrees of freedom, corresponding for example to different edge channels in quantum Hall systems, are present and must be taken into account, upgrading the local single electron coherence to a (t,t')-dependent single electron coherence matrix. The local single electron coherence $\mathcal{G}^{(e)}_{\rho,x}$, or its excess, can be viewed as the single particle "quantum signal" accessible at position x.

Within a 1D chiral system, relating $\mathcal{G}^{(e)}_{\rho,x+\Delta x}(t,t')$ to $\mathcal{G}^{(e)}_{\rho,x}(t,t')$ corresponds to computing the evolution of single-electron coherence during propagation along the chiral channel under consideration. This is a dynamical problem that will be discussed in a forthcoming section. However, it has a trivial expression in the case of ballistic propagation at velocity v_F:

$$\mathcal{G}^{(e)}_{\rho,x+\Delta x}(t,t') = \mathcal{G}^{(e)}_{\rho,x}(t-\Delta x/v_F, t'-\Delta x/v_F) \tag{20}$$

which corresponds to delaying $\mathcal{G}^{(e)}_{\rho,x}$ by the time of flight $\Delta x/v_F$.

Several important examples in the context of electron quantum optics can be discussed which involve single electron and single hole excitations on top of the Fermi sea.

- One single electron excitation on top of the Fermi sea with wavefunction φ_e: the many body state is $\psi^\dagger[\varphi_e]\,|F\rangle$ in which $\psi^\dagger[\varphi_e]$ creates a single electron excitation in the normalized single particle state $|\varphi_e\rangle$. Such a state would be generated by an ideal single electron source operated one time only. The excess single electron coherence is then:

$$\Delta\mathcal{G}^{(e)}(t,t') = \varphi_e(-v_F t)\,\varphi_e(-v_F t')^* \tag{21}$$

- One single hole excitation on top of the Fermi sea with wavefunction φ_h: the many body state is $\psi[\varphi_h]\,|F\rangle$ in which $\psi[\varphi_h]$ destroys a single electron excitation in the normalized single particle state $|\varphi_h\rangle$. Such a state would be generated by an ideal single hole source operated one time only. The excess single electron coherence is then:

$$\Delta\mathcal{G}^{(e)}(t,t') = -\varphi_h(-v_F t)\,\varphi_h(-v_F t')^* \tag{22}$$

  where the minus sign comes from the removal of one electron with from the Fermi sea.

- A single electron hole pair, obtained by transfering a single electron from the hole single particle state φ_h to the electronic single particle state φ_e corresponds to the the many-body state $\psi^\dagger[\varphi_e]\psi[\varphi_h]\,|F\rangle$. This state would ideally be generated during one period by an ideal AC source emitting exactly one electronic and one hole excitation per period. It has an excess single electron coherence given by

$$\Delta\mathcal{G}^{(e)}(t,t') = \varphi_e(-v_F t)\,\varphi_e(-v_F t')^* - \varphi_h(-v_F t)\,\varphi_h(-v_F t')^* \tag{23}$$

  Finally it is possible to generate a quantum superposition involving a pristine Fermi sea and the state that we have just considered, thereby leading to

$$|\Psi\rangle = \left(u + v\psi^\dagger[\varphi_e]\psi[\varphi_h]\right)|F\rangle \tag{24}$$

  in which $|u|^2 + |v|^2 = 1$. Then, the corresponding excess single electron coherence is

$$\Delta\mathcal{G}^{(e)}(t,t') = |v|^2\left(\varphi_e(-v_F t)\,\varphi_e(-v_F t')^* - \varphi_h(-v_F t)\,\varphi_h(-v_F t')^*\right) \tag{25a}$$
$$+\, uv^*\varphi_e(-v_F t)\,\varphi_h(-v_F t')^* + u^* v\varphi_h(-v_F t)\,\varphi_e(-v_F t')^* \tag{25b}$$

  The second line in the r.h.s which involves products of φ_e and φ_h^* or its complex conjugate arises from the coherent superposition between the presence and the absence of the electron-hole pair. These terms correspond to electron-hole coherences and play an important role in the discussion of HOM interferometry experiments.

Of course, in experiments, electron sources are rarely ideal. Due to difficulties in tuning their parameters, finite temperature effects, as well as interactions in some setups, the idealized forms we have just discussed do not correspond to the general form of the excess single electron coherence.

At the two-electron level, the situation starts to become more involved because a two-electron detection event can be viewed as arising from several physical processes [53]. More specifically, both detected electrons can be seen as coming from the Fermi sea, or one from the Fermi sea and one from the electron sources. But we also have to take into accounts two-electron interferences involving the Fermi sea and the electronic excitations emitted by the electron source. In the end, what remains when all these processes are taken out is the intrinsic two-electron coherence, that contains the information on the two-electron excitations emitted by the sources. This leads to the following definition of the intrinsic two-electron coherence [53]:

$$\mathcal{G}_\rho^{(2e)}(1,2|1',2') = \mathcal{G}_F^{(2e)}(1,2|1',2') \tag{26a}$$
$$+ \mathcal{G}_F^{(e)}(1|1')\,\Delta\mathcal{G}_\rho^{(e)}(2|2') + \mathcal{G}_F^{(e)}(2|2')\,\Delta\mathcal{G}_\rho^{(e)}(1|1') \tag{26b}$$
$$- \mathcal{G}_F^{(e)}(1|2')\,\Delta\mathcal{G}_\rho^{(e)}(2|1') - \mathcal{G}_F^{(e)}(2|1')\,\Delta\mathcal{G}_\rho^{(e)}(1|2') \tag{26c}$$
$$+ \Delta\mathcal{G}_\rho^{(2e)}(1,2|1',2')\,. \tag{26d}$$

in which a compact notation for space and time coordinated has been used. Note the presence of the $-$ sign in Eq. (26c) which is associated with the fermionic statistics of electrons.

As expected, the intrinsic second order coherence vanishes for a state involving a single electron excitation on top of the Fermi sea $\psi^\dagger[\varphi_e]\,|F_\mu\rangle$ or a single hole excitation $\psi[\varphi_h]\,|F_\mu\rangle$. The situation becomes more interesting when a source introduces two electronic excitations into two mutually orthogonal electronic states φ_1 and φ_2. Then, considering $|\Psi_{12}\rangle = \psi^\dagger[\varphi_2]\psi^\dagger[\varphi_1]\,|F\rangle$, we have [53]:

$$\Delta\mathcal{G}^{(e)}(t,t') = \varphi_1(-v_F t)\varphi_1(-v_F t')^* + \varphi_1(-v_F t)\varphi_1(-v_F t')^* \tag{27a}$$
$$\Delta\mathcal{G}^{(2e)}(t_1,t_2|t_1',t_2') = \mathrm{Sl}[\varphi_1,\varphi_2](t_1,t_2)\,\mathrm{Sl}[\varphi_1,\varphi_2](t_1',t_2')^* \tag{27b}$$

in which

$$\mathrm{Sl}[\varphi_1,\varphi_2](t_1,t_2) = \varphi_1(-v_F t_1)\varphi_2(-v_F t_2) - \varphi_1(-v_F t_2)\varphi_2(-v_F t_1) \tag{28}$$

denotes the (unnormalized) Slater determinant[2] built from the two single particle states $\varphi_{1,2}$.

More generally, any excitation involving two single particle states will lead to a contribution to the intrinsic two-electron coherence. As explained in Ref. [53], the intrinsic two-electron coherence of a Slater determinant built from $N > 2$ mutually orthogonal single electron wave packets of the form (15) involves all the contributions from two-electron states present[3]:

$$\Delta\mathcal{G}^{(2e)}(1,2|1'2') = \sum_{\text{pairs }\{i,j\}} \mathrm{Sl}[\varphi_i,\varphi_j](1,2)\,\mathrm{Sl}[\varphi_i,\varphi_j](1',2')^* \tag{29}$$

which is the direct generalization of Eq. (16). Exactly as for the single electron expression, this formula only involves diagonal contributions, that is a sum of two-particle wave packets contributions $\Psi_{i,j} \times \Psi_{i,j}^*$: there are no two-electron coherences between different two particle wave packets exactly as in Eq. (16), there are no single electron coherences between two different single particle wave-functions.

In order to obtain such contributions, one has to generate coherent superpositions of two different two-particle excitations which is, for example, the case in the following linear combination of two distinct two-electron excitations on top of the Fermi sea[4]:

$$\frac{1}{\sqrt{2}}\left(\psi^\dagger[\varphi_a]\psi^\dagger[\varphi_b] + \psi^\dagger[\varphi_c]\psi^\dagger[\varphi_d]\right)\,|F\rangle\,. \tag{30}$$

In this case, the intrinsic excess two-electron coherence will involve coherences between the two different two-particle states: the one built on φ_a and φ_b and the one built on φ_c and φ_d. Such a state therefore has the potential for exhibiting intrinsic excess two-particle coherence which does not arises from single particle coherence. As will be clear from the forthcoming discussion of electron dynamics in Section II D, generating such states is not so easy: single particle scattering processes turn Slater determinants such as the Fermi sea into other Slater determinants and never

---

[2] The Slater determinant is usually defined with a $1/\sqrt{N!}$ normalization prefactor which is not present here. This prefactor is needed when one works on the full symmetrized configuration space for the N particle wavefunctions. Whenever one works on the quotient space by the action of the permutation group $\mathfrak{S}_N$, it is not needed.

[3] There are $N(N-1)/2$ possibilities.

[4] Exactly as before the four single electron wave packets φ_i for $i \in \{a,b,c,d\}$ are assumed to be mutually orthogonal.

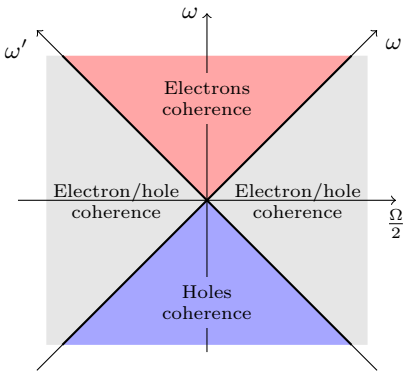

FIG. 4. Frequency domain quadrants for single-electron coherence: depending on the signs of (ω, ω'), we are considering the physical interpretation of $\widetilde{\mathcal{G}}^{(e)}(\omega|\omega')$. The electronic quadrant (in red) defined by both $\omega = \omega + \Omega/2$ and $\omega' = \omega - \Omega/2$ positive gives information about electronic excitations. The hole quadrant (in blue) defined by both ω and ω' being negative gives information about hole excitations. The two off-diagonal quadrants ($\omega\omega' < 0$, light grey) contain information about electron-hole coherences.

into the sum of two such many-body states that differ exactly by two single particle states. In particular, as will be discussed later, applying a classical drive to a electronic reservoir generates a complicated Slater determinant which, therefore, does not lead to deeply off-diagonal two electron coherences.

Whereas single electron coherence was related to averages of single particle quantities such as the time dependent average current or the electron distribution function, two electron coherence is related to two particles quantities such as electronic or charge density fluctuations or current fluctuations. This fact has indeed been known since a long time: computing the particle number fluctuations in an ideal Bose gas, Einstein noticed that besides the classically expected Poissonian contribution, these fluctuations were enhanced by a term related to the single particle coherence [54]. On the other hand, the fermionic statistics is expected to decrease fluctuations as is well known in dc transport by the suppression of the current shot noise [55, 56]. In electron quantum optics, the general relation between current fluctuations and single and two-particle excess coherences has been derived in Ref. [28].

C. Representations of single electron coherence

Because it contains information on all the single electron excitations, the (excess) single electron coherence is much richer than a single particle wavefunction. It is therefore important to have a way to visualize its physical content beyond its mere definition.

In the time domain, its diagonal gives a direct access to the average time dependent current,

$$\langle i(x,t)\rangle_\rho = -ev_F\,\Delta\mathcal{G}^{(e)}_{\rho,x}(t,t)\,, \tag{31}$$

but the off-diagonal values $\mathcal{G}^{(e)}(t,t')$ for $t \neq t'$ are complex and not easily interpreted beyond the fact that its spreading as a function of $t - t'$ informs us on the electronic coherence time. In the frequency domain, its double-Fourrier transform

$$\widetilde{\mathcal{G}}^{(e)}(\omega,\omega') = \int_{\mathbb{R}^2} \mathcal{G}^{(e)}(t,t')\,e^{i(\omega t - \omega' t')}\mathrm{d}t\mathrm{d}t' \tag{32}$$

gives access to the nature of excitations depending on the signs of ω and ω' according to the partition of the (ω, ω') plane into four quadrants depicted on Fig. 4. A non-zero contribution to $\Delta_0\mathcal{G}^{(e)}$ in the electron (resp. hole) quadrant denotes the presence of electron (resp. hole) excitations, whereas a non-vanishing contribution in the off-diagonal quadrants denotes the presence of non-vanishing electron/hole coherences. Beyond these obvious considerations, $\widetilde{\mathcal{G}}^{(e)}(\omega,\omega')$ for $\omega \neq \omega'$ is generically complex valued and does not have an obvious physically transparent interpretation.

These considerations emphasize the need for physically more transparent representations of single electron coherence. As of now, two of them have been unravelled: the first one, discussed in the next paragraph, is the electronic Wigner distribution function [57], a time/frequency version of the Wigner function introduced by Wigner [58] in the early days of quantum theory or, equivalently, a quantum version of the Ville transform introduced in signal processing [59] which captures both the real time and energetic aspects of $\mathcal{G}^{(e)}$. The second one is a discrete one that gives access to the individual single particle wavefunction present within the electron fluid.

1. Time-frequency representation: the Wigner function

The electronic Wigner distribution function[5]

$$W^{(e)}_{\rho,x}(t,\omega) = \int_{\mathbb{R}} v_F \mathcal{G}^{(e)}_{\rho,x}\left(t+\frac{\tau}{2}, t-\frac{\tau}{2}\right) e^{i\omega\tau} \mathrm{d}\tau \tag{33}$$

introduced in Ref. [57] is real and gives access to both time-dependence and energy content at the single particle level. In particular, the average time dependent electric current, the electronic occupation numbers and even the average instantaneous excess energy current $\langle j_E(x,t)\rangle_\rho$ can be related to the excess Wigner distribution function which is defined in the same way from the excess single electron coherence $\Delta\mathcal{G}^{(e)}_{\rho,x}$:

$$\langle i(x,t)\rangle_\rho = -e\int_{\mathbb{R}} \Delta W^{(e)}_{\rho,x}(t,\omega)\mathrm{d}\omega \tag{34a}$$

$$\langle j_E(x,t)\rangle_\rho = \hbar\int_{\mathbb{R}} \omega\, \Delta W^{(e)}_{\rho,x}(t,\omega)\mathrm{d}\omega \tag{34b}$$

$$f_e(\omega) = \lim_{T\to+\infty}\left[\frac{1}{T}\int_{-T/2}^{T/2} W^{(e)}_{\rho,x}(t,\omega)\,\mathrm{d}t\right]. \tag{34c}$$

The Wigner distribution $W^{(e)}_{\rho,x}(t,\omega)$ represents the local first-order correlation function that encodes coherence in time. Similarly, we can characterize coherence in space by introducing the electronic Wigner distribution function at a fixed time,

$$W^{(e)}_{\rho,t}(x,k) = \int_{\mathbb{R}} \mathcal{G}^{(e)}_{\rho}\left(x+\frac{y}{2}, t\middle| x-\frac{y}{2}, t\right) e^{-iky}\mathrm{d}y \tag{35}$$

Here k is introduced as the Fourier conjugate of x. As discussed at the introduction of Eq. (20), single-mode chiral propagation establishes one-to-one correspondence between time (frequency) and coordinate (momentum). Hence in 1D, $p = \hbar k$ is the momentum canonically conjugate to x, and $W^{(e)}_{\rho,t}(x, p/\hbar)$ becomes the Wigner representation of the reduced single-particle density operator $\hat{\rho}$, as defined by the $N = 1$ trace (see Eq. (14)) of the full many-body density operator ρ evolved to time $t_1 = t$. Furthermore, for negligible dispersion Eq. (20) connects the two pictures (time-trace at a fixed site versus snapshot of space at at fixed time), and one has

$$W^{(e)}_{\rho,x}(t,\omega) = W^{(e)}_{\rho,t}(x,k)\,, \tag{36}$$

if one aligns the reference points in space and time, $x = -v_F\, t$, and uses the linear dispersion relation $\omega = v_F\, k$.

For a single point particle in 1D, the full and reduced density operators are equivalent for an isolated electron, as are the full and the excess coherences. Consequently, the Wigner distribution function $W^{(e)}_{\rho,t}(x, p/\hbar)$ gives a complete kinematic description of the state as a Wigner–Weyl transform of the density operator $\hat{\rho}$. This observation connects to the well-known phase-space formulation of quantum mechanics due to Groenewold and Moyal, extending the pioneering ideas of Wigner and Weyl [60]. A pedagogical introduction to the Wigner function and the Weyl transform has been given by Case [61]. In this picture $\rho(x,p) = (2\pi\hbar)^{-1}W^{(e)}_{\rho,t}(x,p/\hbar)$ can be interpreted as a quasi-probability density in two-dimensional phase space, such that a marginal density of $\rho(x,p)$ gives the probability density for the corresponding observable. This property of the phase-space Wigner distribution is the basis for a quantum interpretation [62] of the tomography protocol demonstrated in [32] and described in Section III A 4.

It is important to distinguish the electronic Wigner function from the Wigner function used in quantum optics for description of coherences of a single electromagnetic mode at different orders. In photon quantum optics, Wigner representation is usually used for conjugate continuous variables (so called optical quadratures) governing a single harmonic oscillator corresponding to the relevant spatio-temporal mode of the quantum electromagnetic field. The quantum optical Wigner function of optical quadratures characterizes arbitrarily high order Glauber coherences of this electromagnetic mode and thus is fundamentally different from the Wigner representation of the conjugate variables x and p describing 1D spatial propagation.

In systems with electron-hole symmetry, such as the dispersionless chiral fermion description of Quantum Hall edge channels, the electronic Wigner distribution can be related to the hole Wigner distribution function $W^{(h)}$ which is defined from the hole coherence by Eq. (33): $W^{(e)}_{\rho,x}(t,\omega) = 1 - W^{(h)}_{\rho,x}(t,-\omega)$.

---

[5] The v_F prefactor ensures that $W^{(e)}(t,\omega)$ is dimensionless.

Before discussing the notion of electronic atoms of signal, it is useful to discuss a few examples of the various representations of the single electron coherence associated with simple single electron excitations. Let us consider for example the case of the single electron excitation emitted by the emptying of a single resonant level with energy $\hbar\omega_e$ above the Fermi energy into a chiral edge channel. This leads to an electronic wavefunction with truncated Wigner-Weisskopf spectral shape, that is a truncated Lorentzian wave-function in the frequency domain,

$$\widetilde{\varphi_e}(\omega) = \sqrt{\frac{v_F\gamma_e}{\mathcal{N}}}\,\frac{\mathrm{H}(\omega)}{\omega-\omega_e+i\gamma_e/2}\,, \tag{37}$$

in which γ_e denotes the excitations' natural width, $H(\omega)$ the Heaviside function and $\mathcal{N}$ is a normalization factor. The resulting frequency and time domain representations as well as the electronic Wigner distribution function are depicted in Fig. 5.

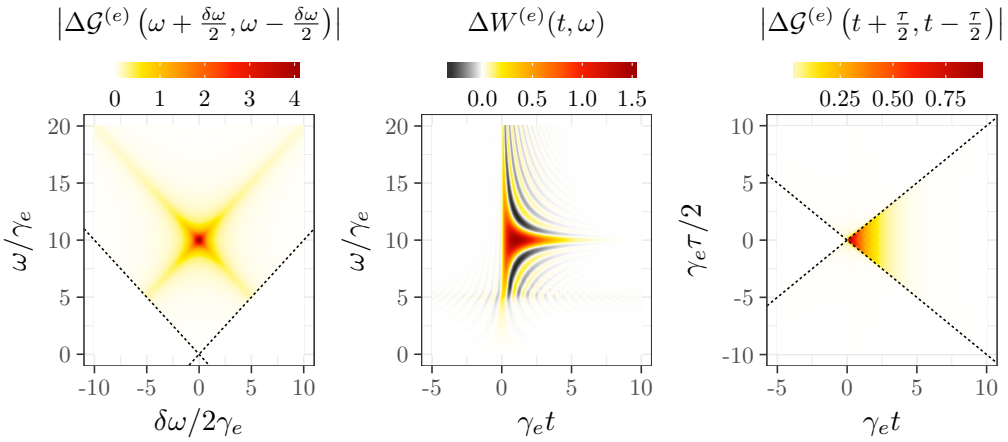

FIG. 5. Representations of the coherence (figure extracted from [20]). Here are depicted three representations of the single electron coherence of a typical wave packet emitted by the mesoscopic capacitor in the single-electron source regime. On the left, we have the modulus of the energy representation of the single-electron coherence $\varphi_e(t)\,\varphi_e(t')^*$ which is only non-vanishing in the electron quadrant as expected. On the right, we have the modulus of the time representation. We can see that the average current is an exponential decay. On the middle, we have plotted the electronic Wigner distribution function which is real and contains both positive and negative values. We can see both the energy dependence of the excitation (which populates only positive energies) and its time dependence (which is an exponential decay).

Let us now turn to lorentzian current pulses carrying a charge $-ne$. The $n=1$ case corresponds to the Leviton source [23] which at zero temperature involves a single electron excitation on top of the Fermi sea. The $n>1$ lorentzian pulse is a Slater determinants obtained from n mutually orthogonal excitations on top of the Fermi sea [23]. Fig. 6 depicts the excess electronic Wigner distribution function of the single particle wavefunctions present within Lorentzian pulses carrying an integer charge $-ne$ for $n=1$ to $n=4$: the $q=-e$ pulse involves the first one, the $q=-2e$ pulse involves the two first single electron states, the $q=-3e$ the $n=1$ to $n=3$ and so forth. Note that these single particle wavefunctions have the same average current but have different energy distributions. Note that for $n\geq 2$, their Wigner functions exhibit negativities close to $t\simeq 0$.

From the single particle point of view, a Slater determinant built from n-electron excitations appears as an incoherent mixture of the single particle states building it (see Eq. (16)). This leads to the excess Wigner functions depicted on Fig. 7 which describe the full single particle content of Lorentzian pulses carrying an integer multiple of the elementary charge $-e$.

By contrast, introducing a coherent superposition of various single particle state leads to interference terms in the Wigner function. Let $|\psi\rangle = \frac{1}{\sqrt{2}}\left(|\varphi_1\rangle + e^{i\vartheta}|\varphi_2\rangle\right)$ be such a coherent superposition built from two mutually single particle states $|\varphi_{1,2}\rangle$, then we have:

$$W^{(e)}_{|\psi\rangle}(t,\omega) = \frac{1}{2}\left(W^{(e)}_{|\varphi_1\rangle}(t,\omega) + W^{(e)}_{|\varphi_2\rangle}(t,\omega)\right) \tag{38a}$$

$$+\,\Re\left[e^{i\vartheta}v_F\int_{\mathbb{R}}\varphi_1\left(t-\frac{\tau}{2}\right)^*\varphi_2\left(t+\frac{\tau}{2}\right)e^{i\omega\tau}\mathrm{d}\tau\right] \tag{38b}$$

The second line is the term associated with quantum interferences between the two single particle states $|\varphi_1\rangle$ and $|\varphi_2\rangle$. It also appears in classical signal processing when considering a classical signal $X(t)$ which is the sum of two classical

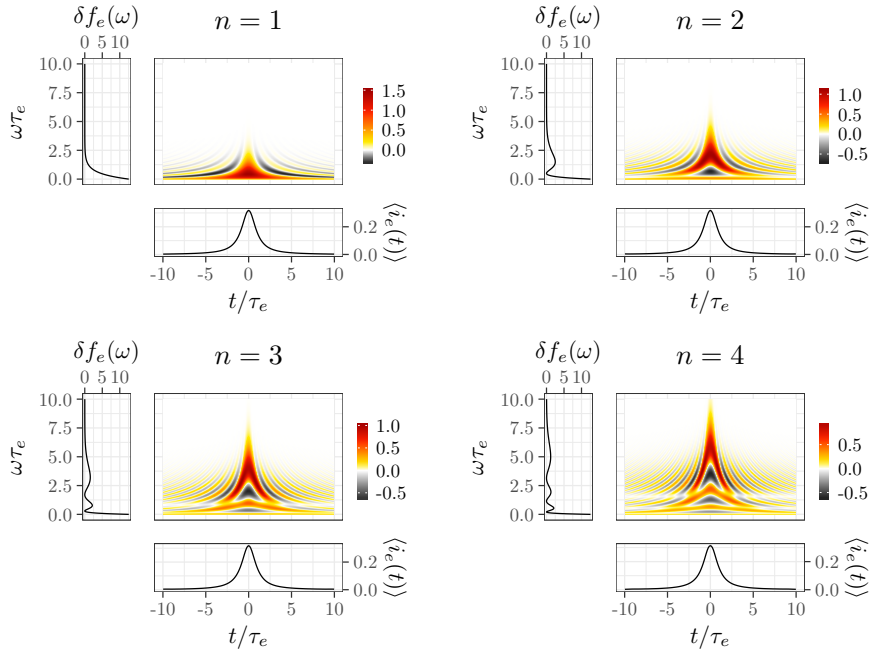

FIG. 6. (Figure reproduced from [20]) Wigner representation of the single-electron wavefunctions building the n-Leviton excitations up to $n = 4$.

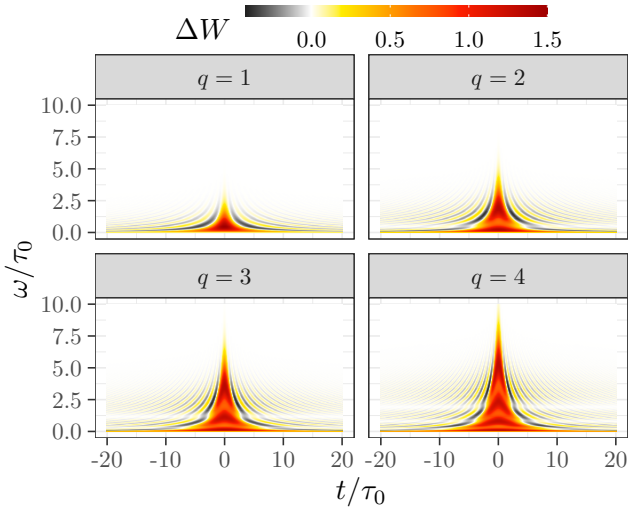

FIG. 7. Excess Wigner function for the n-Leviton excitations up to $n = 4$. Note that $\Delta W^{(e)}(t = 0, \omega)$ exhibits n maximas which arise from the addition of the contributions of the n individual single particle states depitected on 6: each of them adds one more spot with negativities close to $t \simeq 0$ at higher values of ω.

signals $X_{1,2}(t)$. If we consider two single particle states that are related by a time translation, or by a frequency translation, the two contributions $W^{(e)}_{|\varphi_{1,2}\rangle}(t, \omega)$ appear as two distinct "blobs" in the (t, ω) planes. The interference contribution appears as a ghost image involving fringes – and therefore negativities – located at the barycenter of the two previously mentioned blob. The interferences fringes oscillate over a scale that is inversely proportional to the separation between $|\varphi_1\rangle$ and $|\varphi_2\rangle$ and they occur in the direction perpendicular to the direction of separation of the two contributions. More specifically: when φ_1 and φ_2 are separated by a time translation, the oscillations occur as a function of energy, thereby leading to fringes in the electronic distribution functions that are the analogous of the channeled spectrum observed in optical interferometers illuminated by white light [57]. On the other hand, when the two states are translated in energy, then the oscillations occur as a function of time and are visible on the time

Band theory [63, 64]	Floquet-Bloch analysis [29]
Spatial period	Time period
Single particle Hamiltonian	Single electron coherence
Band energy $\varepsilon_a(k)$	Floquet-Bloch probabilty spectrum $g_a(\nu)$
Quasi-momentum k	Quasi-energy ν
Wannier function $w_{a,l}(x)$	Atom of signal $\varphi_{k,l}(t)$

TABLE I. Analogy between solid state band theory and signal processing of the excess single-electron coherence described in [29]: the spatial period of the crystal is replaced by the time period $T = f^{-1}$ of the electron source. Instead of diagonalizing a single particle Hamiltonian and spatial translations, one diagonalizes the projections of the single particle excess coherence operator in the electron and hole subspaces and time translation, thereby obtaining Floquet-Bloch bands. Eigenvalues are probabilities instead of energies and depend on a quasi-energy $0 \leq \nu \leq 2\pi f$ instead of a quasi-momentum. The electronic atoms of signal play the same role as the Wannier functions in band theory and are therefore subject to the same ambiguities [65].

dependent average current.

2. A discrete representation: electronic atoms of signal

As discussed in Section II B 2, the single-electron excess coherence carries the information about all single particle excitations present above the reference Fermi sea. As such, it may be a bit complicated to interpret it as soon as there are more than one electronic or one hole excitation present. In particular, electron/hole coherences lead to complex interference patterns on the excess electronic distribution function which are not very suitable for quantifying the amount of electron-hole coherence.

However, for T-periodic sources, a general decomposition can be found which appears as a natural generalization of the expressions [29] discussed in Section II B 2. This expression consists of a representation of single-electron coherence in terms of what are called electronic and hole atoms of signals [28]. These atoms of signal are electronic and hole single particle states that form orthonormal bases of the space of electronic and hole single particle excitations which are covariant with respect to translation by the period T. More specifically, these states fall into families indexed by a, $|\varphi_{a,l}\rangle$, with $l \in \mathbb{Z}$, where the l index corresponds to a period of duration T so that translating $|\varphi_{a,l}\rangle$ by T in the time domain leads to $|\varphi_{a,l+1}\rangle$. Then, as proved in [29], the most general form of the excess single electron coherence is given by

$$\Delta\mathcal{G}^{(e)}(t,t') = \sum_{l,l'}\sum_{a} g_a^{(e)}(l-l')\,\varphi_{a,l}^{(e)}(t)\,\varphi_{a,l'}^{(e)}(t')^* - \sum_{l,l'}\sum_{b} g_b^{(h)}(l-l')\,\varphi_{b,l}^{(h)}(t)\,\varphi_{b,l'}^{(h)}(t')^* \tag{39a}$$

$$+ \sum_{l,l'}\sum_{a,b}\left(g_{a,b}^{(eh)}(l,l')\,\varphi_{a,l}^{(e)}(t)\,\varphi_{b,l'}^{(h)}(t')^* + g_{b,a}^{(he)}(l,l')\,\varphi_{b,l}^{(h)}(t)\,\varphi_{a,l'}^{(e)}(t')^*\right), \tag{39b}$$

in which we have both electronic atoms of signals (the $\varphi_{a,l}^{(e)}$) and hole atoms of signal (the $\varphi_{b,l}^{(h)}$). In these expressions, the real number $g_a^{(e)}(0)$ and $g_b^{(h)}(0)$ respectively represent the emission probabilities per period for the electronic atom of signal $\varphi_{a,l}^{(e)}$ and hole atom of signal $\varphi_{b,l}^{(h)}$. Note the $-$ sign in front of the hole contribution which expresses the fact that a hole is always the absence of an electron.

There are no coherences between the different families ($a \neq a'$) of electronic atoms of signal as well as between the different families ($b \neq b'$) of hole atoms of signal but there may be electron-hole coherences: $g_{ab}^{(eh)}(l,l')$ may be non-zero. In the same way, electronic atoms of signals may be correlated from one period to the other: $g_{aa}^{(ee)}(l,l')$ maybe non-vanishing even for $l \neq l'$, thereby reflecting the possibility of an electronic coherence time larger than the time-period T. Therefore, the use of electronic atoms of signal provides a discrete representation of single electron coherence which makes it easier to distinguish what are the single electron excitations emitted by an electron source from how they are emitted. This is the exact analogous, in the quantum domain, of describing music in terms of musical notes and of the music score (see Fig. 8).

One should nevertheless keep in mind that the electronic atoms of signals are not unique, as expected by the analogy with the Wannier functions [66] in band theory (Table I summarizes the analogy between the two approaches). In band theory, Wannier functions are not unique because Bloch-functions, which are common eigenvectors of the electrons and of translation operators associated with the crystal's spatial periodicity, may be redefined at least generically by a phase. Consequently, Wannier functions have an intrinsic ambiguity, that is usually lifted by imposing an extra

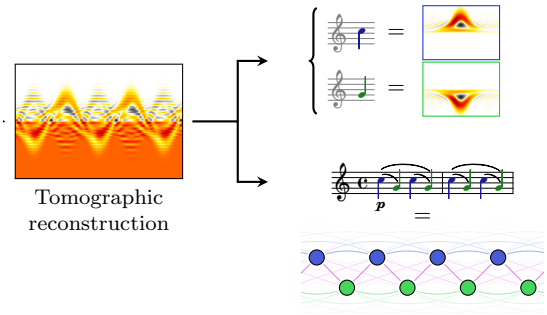

FIG. 8. Schematic representation of the decomposition of the excess electronic coherence $\Delta W^{(e)}(t,\omega)$ in electron and hole atoms of signals (case of a low amplitude sinusoidal drive). The atoms of signal play the role of musical notes and the coherences appearing in Eq. (39) provide the analogous of the music score.

condition such as minimal spreading in space. In the present situation, the situation is the same: the atoms of signals may be chosen as having a minimal spreading in time. The reader is referred to Ref. [29] for the corresponding details.

Such a decomposition has also been derived within the framework of time dependent single particle scattering theory in Ref. [67] but the result is indeed much more general since it only relies on time periodicity and the general properties of single electron coherence. Although we have discussed it in the presence of a Fermi sea, the same ideas have been used in the solitary electron approximation [32], in which case only electronic atoms of signals are present.

D. Dynamics of coherent electrons

Let us now turn to the dynamics of coherent electrons within quantum conductors envisioned for electron quantum optics experiments. To understand the difference between photon and electron quantum optics, one has to realize that with photons non-linearities are notoriously hard to achieve whereas for electrons Coulomb interactions brings them to the center of the stage. As we shall see, this can be viewed as a weakness or a strength of electron quantum optics, depending on the point of view.

The role of Coulomb interactions in time-dependent electrical quantum transport has been emphasized by Büttiker[6]. He noticed that single electron scattering, which proved to be so fruitful when discussing dc transport properties [18, 19, 71], had to be amended in order to deal with time-dependent situation [72]. In particular, he pioneered a mean-field approach to the problem [73], arguing that in the presence of a time dependent current the electrons would perceive a modified time dependent electric potential arising from the corresponding modification of charge density. This approach has been extremely fruitful [74, 75] leading to many experimental confirmations, some of them directly relevant for electronic sources used in electron quantum optics [76–79].

However, we should not expect such an approach to work in all situations: in electron quantum optics, the electrical current associated with one to few electron (and possibly hole) excitations may lead to a quantum fluctuating potential which cannot be described as a classical time dependent potential. Büttiker's self consistent mean field approach is thus expected to fail and a full fledge quantum treatment of single electron decoherence [80] is needed. This is also the case when considering dynamical Coulomb blockade [81–83] in which the electrons passing through a conductor see a quantum environment whose properties depend on the full circuit in which the conductor is embedded. Here again, a careful treatment is needed in order to ensure that the proper fluctuations of the potential within the conductor are accounted for, as for example, in Ref. [84].

In this review, we will thus present the most commonly used approaches to the dynamics of electrons used to describe electron quantum optics experiments, starting from the simplest ones and elaborating forward towards more sophisticated ones. For this reason, we will start by considering that non-linearities could be neglected, which turns out to be not such a bad approximation in a number of experimentally relevant situations. This will enable us to understand electronic interferometry as transformation performed in the electronic quantum coherences which are the quantum signal of interest in the field. Then, discussing the effect of a simple electron-electron Coulomb interaction will show us how relevant electron quantum optics is for fast and sensitive detection of local electromagnetic fields.

[6] The role of strong electronic correlations was recognized much before even in d.c. transport, for example, in the Kondo problem or in Luttinger liquids. Büttiker's contribution was to recognize it even in ordinary quantum conductors in which the Fermi liquid paradigm is not invalidated by the appearance of strong electronic correlations. Attempts at connecting the scattering formalism for quantum transport to the more standard methods of many-body physics even in the presence of interactions are contemporary from Büttiker *et al* works: see Ref. [68–70] for example.

1. Free electronic propagation

The case of free chiral dispersionless fermions[7] has already been discussed: propagation is described by Eq. (20). In terms of the electronic Wigner distribution function, this translates into a rigid time translation by the time of flight of the free electrons:

$$W^{(e)}_{\rho,x+\Delta x}(t,\omega) = W^{(e)}_{\rho,x}(t-\Delta x/v_F,\omega)\,, \tag{40}$$

as discussed in the context of phase-space interpretation (see Eq. (36)). The electronic Wigner distribution therefore propagates unaltered at velocity v_F. Consequently, the electronic distribution function is unaltered after propagation and the average charge density keeps its shape after propagation over a distance Δx.

The case of free fermions with dispersion, such as non-relativistic free fermions, is more interesting and has been considered in Ref. [85] with a slight variation: instead of comparing the Wigner functions in the (t,ω) plane at two different positions, they consider the usual Wigner distribution function in the (x,k) plane defined by Eq. (35) and study how it changes with time. First of all, this Wigner function can be rewritten as

$$W_{\rho,t}(x,k) = \int_{\mathbb{R}} \left\langle c^\dagger\left(k-\frac{q}{2}\right)\, c\left(k+\frac{q}{2}\right)\right\rangle_\rho e^{iqx}\, e^{i(\omega(k-q/2)-\omega(k+q/2))t}\frac{\mathrm{d}q}{2\pi} \tag{41}$$

in which we have used the Heisenberg evolution for the electronic mode operators,

$$c(k,t) = e^{-i\omega(k)t}c(k)\,. \tag{42}$$

The time evolution of the (x,k) electronic Wigner distribution function is therefore expressed in terms of a partial convolution with a kernel that encodes the dynamics

$$W_{\rho,t}(x,k) = \int_{\mathbb{R}} W_{\rho,0}(x',k)\, K_t(x-x';k)\,\mathrm{d}x' \tag{43}$$

$$K_t(x-x';k) = \int_{\mathbb{R}} e^{i(\omega(k-q/2)-\omega(k+q/2))t} e^{iq(x-x')}\,\frac{\mathrm{d}q}{2\pi} \tag{44}$$

which reduces to the spatial version of Eq. (40) for chiral relativistic fermions moving at the constant Fermi velocity v_F:

$$W_{\rho,t}(x,k) = W_{\rho,0}(x-v_Ft,k) \tag{45}$$

When the electronic dispersion relation $\omega(k)$ is non-linear, approximating $\omega(k\pm q/2)$ by $\omega(k)\pm\omega'(k)q/2$ leads to Eq. (45) but with a k-dependent velocity: $v_F(k)=\omega'(k)$. For free fermions with quadratic dispersion relation $\omega(k)=\hbar k^2/2m$, this approximation is indeed exact and Eq. (45) is valid provided one substitutes the constant v_F by the k-dependent velocity $v_F(k)=\hbar k/m$. Therefore, we shall limit ourselves to this case for simplicity.

It is now important to consider the effect of such a dispersion relation on a Fermi sea of electrons and to a local disturbance of the electronic density. For a Fermi sea with all states of given 1D momentum filled up to $|k|=k_F$ the (x,k) Wigner distribution function does not depend on x and is thus left invariant in time translation by t as can be seen from (45) when $W_{\rho,0}(x,k)$ does not depend on x.

This is not the case for an initial state that contains a local density inhomogeneity ($\partial_x W_{\rho,0}(x,k)\neq 0$). In a semi-classical view of such a disturbed Fermi sea, described by an x-dependent k_F, we could consider that for $k\simeq k_F(x)$ $W_{\rho,0}(x,k)=\Theta(k_F(x)-k)$. Then, as explained in Ref. [85], Eq. (45) with $v_F=\hbar k/m$ implies that the average spatial density $\langle n(x,t)\rangle$, which is obtained from $W_{\rho,t}(x,k)$ by integrating over k, would then develop a schock wave along x as explained on Fig. 9-a.

The underlying physics is quite simple: the initial density bum gets distorted by the dispersive propagation, its top (higher k) part running faster than its bottom (lower k) part. In the classical approximation, its sharp boundary is not anymore described by a single value function of x and integrating over k then leads to square-root singularities in the average density $\langle n(x,t)\rangle$.

However, this is an artefact of the description of the initial (x,k) Wigner distribution function as a sharp deformation of the Fermi sea $\Theta(k_F(x)-k)$. In reality, the initial state is nothing but a coherent-state of 1D edge magnetoplasmons

---

[7] Sometimes also called "relativistic" because of their linear dispersion relation $\omega(k)=v_Fk$.

on top of the Fermi sea and its spatial coherence in which all the single electron wave functions have been modulated by the same position dependent phase $\theta(x)$. This state is of the form

$$\mathcal{G}^{(e)}_{t=0}(x,x') = \frac{e^{i(\theta(x)-\theta(x'))}}{2\pi(x'-x+i0^+)} \tag{46}$$

which is the generalization of Eq. (17). Expanding

$$\theta\left(x+\frac{y}{2}\right) - \theta\left(x-\frac{y}{2}\right) \simeq y\,(\partial_x\theta)(x) + \frac{(\partial_x^3\theta)}{24}\,y^3 + \dots \tag{47}$$

and introducing the notation $k_F(x) = (\partial_x\theta)(x)$ then leads to the initial (x,k) electronic Wigner distribution [85]

$$W_{t=0}(x,k) \simeq \mathrm{Ai}_1\left(2^{2/3}\left|(\partial_x^2 k_F)(x)\right|^{-1/3}(k-k_F(x))\right) \tag{48}$$

in which $\mathrm{Ai}_1(x)$ is the following integral of the Airy function:

$$\mathrm{Ai}_1(x) = \int_x^{+\infty} \mathrm{Ai}(z)\mathrm{d}z \tag{49}$$

This integrated Airy function varies from 1 in the limit $x \to -\infty$ to 0 in the limit $x \to \infty$ with an exponential decay for x positive and oscillations within the $x < 0$ plateau. This explains the ripples present in the initial Wigner distribution $W_{t=0}(x,k)$ which are truly a quantum effect arising from the phase coherence of all the electrons within the quantum many body state under consideration. Although Eq. (48) shows these quantum features in the k direction, we can indeed rewrite this result a bit differently. Denoting by $x_F(k)$ the inversion of $k = k_F(x)$ for (x,k) located close to the curve $k = k_F(x)$, we have $x'_F(k) \simeq (x - x_F(k))/(k_F(x) - k)$ and $(\partial_x^2 k_F)(x_F(k)) = -x''_F(k)/x'_F(k)^3$ and therefore

$$W^{(e)}_{t=0}(x,k) \simeq \mathrm{Ai}_1\left(2^{2/3}\left|(\partial_k^2 x_F)(k)\right|^{-1/3}(x-x_F(k))\right). \tag{50}$$

Time evolution using Eq. (45) then consists of replacing $x_F(k)$ by $x_F(k,t) = x_F(k) - v_F(k)t$ which does not change $(\partial_k^2 x_F)(k)$ since $v_F(k) = \hbar k/m$. It shows the presence of oscillations in the plateau region $x < x_F(k,t)$ as well as the exponential decay for $x > x_F(k,t)$ for $t > 0$. As shown in Ref. [85], this smoothed behavior of the Wigner function in the (x,k) plane is responsible for the smearing out of the shock singularities discussed previously. Fig. 9 depicts the time evolution of the excess (x,k)-Wigner distribution function and density charge for an initial Lorentzian bump that carries a charge $-4e$. This examples illustrates the quantum-smoothing discussed here.

To get an insight of the parameter domain where these effects are important, let us discuss the scaling of these quantum ripples in terms of the average number of electrons ΔN involved in it. Assuming that the fluctuation spreads over a distance L, $k_F \simeq \Delta N/L$, and therefore, the scale of the quantum ripples is $\delta k \simeq (\Delta N)^{1/3}/L$ whereas the typical scale of the k is $\Delta N/L$. Consequently, the relative scale of the quantum ripples compared to the spreading in k of the density bump is

$$\frac{\delta k}{k} \simeq (\Delta N)^{-2/3}. \tag{51}$$

This scaling shows that, as expected, the quantum ripple are prominent when considering pulses involving single and sub-single electron charge but are a widely subdominant feature in the case of pulses involving a large number of electrons ($\Delta N \gg 1$). The scaling of Δk with ΔN also enables us to discuss the temperature scale at which the quantum ripples are smeared out. Assuming that the ground state is a Fermi sea, with Fermi velocity v_F, this temperature scale is defined by $k_B T_* = \hbar v_F\,\delta k$ which leads to

$$k_B T_* \simeq \frac{\hbar v_F}{L}\,(\Delta N)^{1/3}. \tag{52}$$

Whenever $T_{\mathrm{el}} \gtrsim T_*$, the quantum ripples are smeared out by thermal fluctuations and the semi-classical approximation is valid.

A similar discussion can be carried out when considering the propagation of the electronic Wigner distribution function $W^{(e)}(t,\omega)$ across a region of length l in which the electrons are scattered elastically with an ω-dependent phase $e^{i\theta(\omega)}$. The case of a linear phase $\theta(\omega) = \omega l/v_F$ where v_F is a given velocity corresponds to a global time translation of $W^{(e)}(t,\omega)$ by the time of flight l/v_F. In full generality, the outgoing Wigner function can be expressed in term of the incoming one by temporal convolution using a kernel that depends on ω. When the non-linearity of the scattering phase $\theta(\omega)$ is only taken into account at first order, the outgoing Wigner distribution function is related to the incoming one by $W^{(e)}_{\mathrm{out}}(t,\omega) = W^{(e)}_{\mathrm{in}}(t-\tau(\omega),\omega)$ in which $\tau(\omega) = (\partial_\omega\theta)(\omega)$ denotes the Wigner-Smith time delay for the electronic scattering across the region of length l. The discussion of the physics of quantum ripples over a semi classical shock can then be carried along the same lines as Ref. [85].

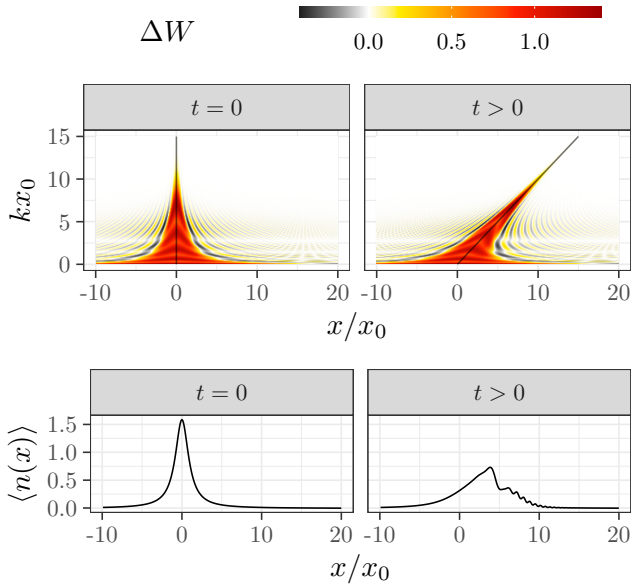

FIG. 9. Top part: Propagation of the Wigner electronic function of a $q = -4e$ Lorentzian density bump of width x_0 in a 1D free electron gas with a quadratic dispersion relation: (left panel) Initial $(x;k)$-distribution function. (right panel) Evolution of the exact (x,k) Wigner distribution function $\Delta W_t^{(e)}(x,k)$ at $t>0$. For simplicity, the excitation has been translated back to $x=0$. Bottom part: corresponding average density in space obtained by integrating $\Delta W^{(e)}(x,k)$ over k. Note that at $t>0$, the classical shocks are smoothed.

2. *Time dependent single particle scattering*

More generally, neglecting the effect of interactions amount to describe a quantum conductor by linear scattering theory for fermionic fields. This is the basic idea behind Büttiker's scattering theory approach. In its most general form, the scattering matrix is non stationary. The scattering amplitude $S_{\alpha,\beta}(t,t')$ for an electron to enter via channel β at time t' and exit into channel α at time t depends on both times and not only of $t-t'$. The incoming and outgoing fermionic fields are then related linearly

$$\psi_{\alpha,\mathrm{out}}(t) = \sum_\beta \int_{\mathbb{R}} S_{\alpha,\beta}(t,t')\,\psi_{\beta,\mathrm{in}}(t')\,\mathrm{d}t'\,. \tag{53}$$

This relation immediately connects the outgoing electronic coherences to the incoming ones. For example, considering a very simple conductor with only one incoming channel and one outgoing channel so that we could get rid of the α and β indices, the outgoing excess single electron coherence is related to the incoming one by

$$\Delta\mathcal{G}^{(e)}_{\mathrm{out}}(t,t') = \int_{\mathbb{R}^2} S(t,t_+)\,S(t',t_-)^*\,\Delta\mathcal{G}^{(e)}_{\mathrm{in}}(t_+,t_-)\,\mathrm{d}t_+\mathrm{d}t_-\,. \tag{54}$$

Such an equation is nothing but a linear filtering of the incoming quantum signal $\Delta\mathcal{G}^{(e)}_{\mathrm{in}}$. It will be discussed more explicitly in the next section. This simple observation is at the heart of the interpretation of electronic ideal interferometry experiments in terms of quantum signal processing. But before digging into specific examples, let us comment on a physically transparent interpretation of time dependent scattering amplitude. As we have just said, such an amplitude is a two-time quantity $S(t,t')$. Exactly as for the single particle amplitude, several equivalent representations can be given. The first one is the afore used time-domain representation. Considering chiral fermions on a line propagating at velocity v_F, the mode operators at fixed energy $c(\omega)$ are scattered according to

$$c_{\mathrm{out}}(\omega) = \int_{\mathbb{R}} S(\omega,\omega')\,c_{\mathrm{in}}(\omega')\,\mathrm{d}\omega' \tag{55}$$

in which

$$S(\omega,\omega') = \frac{1}{2\pi}\int_{\mathbb{R}^2} S(t,t')\,e^{i(\omega t-\omega' t')}\mathrm{d}t\mathrm{d}t' \tag{56}$$

represents the amplitude for an incoming electron at energy $\hbar\omega$ to be scattered to energy $\hbar\omega'$ (see Appendix A for a reminder). It is interesting to connect it to the time-frequency representation of $S(t,t')$ defined by

$$S(\Omega,\tau)=\int_{\mathbb{R}} S\left(t+\frac{\tau}{2},t-\frac{\tau}{2}\right)\,e^{i\Omega t}\mathrm{d}t\,. \tag{57}$$

We have then

$$S(\omega,\omega')=\frac{1}{2\pi}\int_{\mathbb{R}} S(\omega-\omega',\tau)\,e^{i(\omega+\omega')\tau/2}\mathrm{d}\tau \tag{58}$$

The physical interpretation of this equation is quite natural. Let us start with an incoming electron at energy $\hbar\omega'$ and propagate it over a distance $l/2$, its state transforms according to $|\omega'\rangle \mapsto e^{i\omega' l/2v_F}\,|\omega'\rangle$. Let us now assume that there is a dimensionless amplitude $\mathcal{A}(\omega-\omega',l)$ for its energy to shift from $\hbar\omega'$ to $\hbar\omega$. Let us then propagate it along distance $l/2v_F$ again, accumulating a phase $e^{i\omega l/2v_F}$. If we sum over all possible propagation distances l and energy changes $\Omega=\omega-\omega'$, we obtain the scattered state as[8]

$$S\,|\omega'\rangle=\int_{\mathbb{R}^2}\mathcal{A}(\omega-\omega',l)\,e^{i(\omega+\omega')l/2v_F}\,|\omega\rangle\,\frac{\mathrm{d}l\mathrm{d}\omega}{2\pi v_F} \tag{59}$$

Identifying $S(\omega,\omega')$ with $\langle\omega|S|\omega'\rangle$ – see Appendix A – directly shows that $S(\Omega,\tau)$ can be identified with $\mathcal{A}(\Omega,\tau)$ since

$$\langle\omega|S|\omega'\rangle=\frac{1}{2\pi}\int_{\mathbb{R}}\mathcal{A}(\omega-\omega',v_F\tau)\,e^{i(\omega+\omega')\tau/2}\,\mathrm{d}\tau\,. \tag{60}$$

The time-frequency representation $S(\Omega,\tau)$ of the time dependent scattering amplitude thus has a natural interpretation: it corresponds to the amplitude for shifting the energy by $\hbar\Omega$ after free propagation over a time of flight $\tau/2$ at the initial energy and before free propagation over the same time of flight at the final energy. In this interpretation, the time dependant scatterer is replaced by a quantum scatterer with paths of time of flight τ which are summed over and the inelastic ($\omega\neq\omega'$) contribution to the scattering is concentrated mid-flight.

For a time independent scattering matrix, $S(t,t')$ only depends on $t-t'$ and therefore $S(\Omega,\tau)$ reduces to $2\pi\delta(\Omega)S(\tau)$ where $S(\tau)$ is $S(t+\tau,t)$ for any value of t, therefore connecting τ to the possible times of flight within the time independent scatterer.

When the single particle scattering is T-periodic, *id est* $S(t+T,t'+T)=S(t,t')$ for all (t,t'), the Fourier transform with respect to $(t+t')/2$ leads to a series of peaks at $\Omega=2\pi nf$ where $f=1/T$ thereby showing that the energy is transfered by multiples of hf. Time periodic single particle scattering theory is commonly called Floquet scattering theory and has been pioneered by Moskalets and Büttiker for discussing electron pumps [86, 87] and, later for discussing properties of the mesoscopic capacitor [88–90] and also to introduce two electron coherences [91].

3. Photo-assisted propagation

A very important example consists of a region of finite length l in which electrons experience a classical time and space dependent electrical potential $U(x,t)$. We consider here the case of chiral electrons with k-independent velocity. During their propagation, these charged particules accumulate an electric phase. For a point particle of charge q propagating along $t\mapsto\mathbf{r}_t$, the electromagnetic phase is

$$e^{\phi[\mathbf{r}(t)]}=e^{\frac{iq}{\hbar}\int_{t_i}^{t_f}(\mathbf{v}_t\cdot\mathbf{A}(\mathbf{r}_t,t)-V(\mathbf{r}_t,t))\mathrm{d}t} \tag{61}$$

in which $(\mathbf{A},V)$ denote the electromagnetic potentials and $\mathbf{v}_t=\mathrm{d}\mathbf{r}/\mathrm{d}t$ the particle's velocity. In the present case of particles of charge $q=-e$ propagating in 1D a constant velocity v_F where $\mathbf{A}=0$, the phase accumulated during the traversal of the region $-l/2\le x\le l/2$ in which the electrons see the potential $U(x,t)$ is

$$e^{\frac{ie}{\hbar v_F}\int U(x,t_0-x/v_F)\,\mathrm{d}t}\,. \tag{62}$$

---

[8] Using $\omega=v_Fk$, $\mathrm{d}l\,\mathrm{d}\omega/2\pi v_F$ corresponds to the usual measure on the (x,k) space.

in which t_0 denotes the time at which the electron trajectory passes at $x = 0$. This expression directly leads to the time dependent scattering matrix across the $x = -l/2$, $x = l/2$:

$$S_U(t,t') = e^{\frac{ie}{\hbar}\int_{t'}^{t} U(l/2-v_F(\tau-t),\tau)\,\mathrm{d}\tau}\delta\left(t-t'-\frac{l}{v_F}\right) \tag{63}$$

The presence of the $S_0(t,t') = \delta(t-t'-l/v_F)$ comes from chiral propagation at fixed velocity v_F whereas the effect of the time dependent electrical potential arises from the phase.

Let us compute the time-frequency representation $S(\Omega,\tau)$ defined by Eq. (57) which provides us with an interpretation in terms of time of flights and energy transferts for the electrons:

$$S_0(\Omega,\tau) = 2\pi\delta(\Omega)\delta(\tau-l/v_F) \tag{64a}$$

$$S_U(\Omega,\tau) = \delta(\tau-l/v_F)\int_{\mathbb{R}} e^{i\Omega t}e^{\frac{ie}{\hbar}\int_{-l/2v_F}^{l/2v_F} U(v_Ft',t+t')\,\mathrm{d}t'}\,\mathrm{d}t \tag{64b}$$

Eq (64a) just expresses that, when the potential is zero, the electron propagates elastically with a time of flight l/v_F across the $|x| \leq l/2$ region. Eq. (64b) shows that, in the presence of a non zero potential, although the time of flight is still l/v_F, the electron may gain or loose energy with a photo-assisted amplitude given by the Fourier transform of the accumulated phase

$$\mathcal{A}_U(\Omega) = \int_{\mathbb{R}} e^{i\Omega t}e^{i\phi(t)}\,\mathrm{d}t \tag{65a}$$

$$\phi(t) = \frac{e}{\hbar}\int_{-l/2v_F}^{l/2v_F} U(v_Ft',t+t')\,\mathrm{d}t' \tag{65b}$$

This expression explicitly shows that it is the time-dependence of the potential that leads to inelastic scattering of the electron ($\mathcal{A}_U(\Omega) \neq 0$ for $\Omega \neq 0$). In the case of a T-periodic drive ($U(x,t+T) = U(x,t)$ for all (x,t)), the phase is T-periodic in t and therefore $\mathcal{A}_U(\omega)$ is a succession of δ peaks at $\Omega = 2\pi mf$ for $m \in \mathbb{Z}$ which are interpreted for the amplitudes for absorbing ($m > 0$) of emitting ($m < 0$) $|m|$ photons of energy hf.

Before discussing two important example, let us consider the case where the potential seen by the electrons in the $|x| \leq l/2$ region is of the form $U(x,t) = f(x)\,U(t)$ where $U(t)$ is a time dependent voltage and $f(x)$ a dimensionless function vanishing for $|x| > l/2$ which plays the role of a window function. Such a form is expected in the case of a classical drive applied by a top gate in the limit where the potential drop between the top gate and the electron gas can be neglected. A simple model consists of $f(x) = 1$ for $|x| \leq l/2$and zero otherwise. Then, introducing the Fourier transform $\tilde{U}(\omega)$ of $U(t)$, we find that

$$\phi(t) = \frac{e}{\hbar}\int_{\mathbb{R}} \sin(\omega l/2v_F)\frac{\tilde{U}(\omega)}{\omega}\,e^{-i\omega t}\frac{\mathrm{d}\omega}{2\pi} \tag{66}$$

therefore showing that the finite length region acts as an antenna, filtering the various Fourier components of the voltage drive.

In the case of an applied sinusoidal drive at frequency ω_0, $\tilde{U}(\omega) = \pi\left[U_0\delta(\omega-\omega_0) + U_0^*\delta(\omega+\omega_0)\right]$ where $\omega_0 = 2\pi f$ and U_0 denotes the complex amplitude of the drive. This leads to the accumulated phase

$$\phi(t) = \frac{e|U_0|}{2\hbar}\frac{\sin(\omega_0 l/2v_F)}{\omega_0}\left(e^{i\varphi_0}e^{-i\omega_0 t} + \text{h.c.}\right) \tag{67}$$

in which φ_0 is the phase of the sinusoidal drive which can be absorbed in a time shift. Therefore, up to a linear phase in Ω, we find that

$$\mathcal{A}_U(\Omega) = \int_{\mathbb{R}} e^{i\Omega t}e^{i\frac{e|U_0|}{hf}\sin(\pi fl/v_F)\,\sin(\omega_0 t)} \tag{68}$$

Denoting by $U_R = |U_0|\sin(\pi fl/v_F)$ the filtered voltage amplitude, we obtain $\mathcal{A}_U(\Omega)$ as a sum of δ peaks:

$$\mathcal{A}_U(\Omega) = 2\pi\sum_{n=-\infty}^{\infty} e^{2\pi inft_0}J_{-n}\left(\frac{e|U_R|}{hf}\right)\delta(\Omega-2\pi nf) \tag{69}$$

in which we have restored the dependence on the phase of the sinusoidal drive via a time t_0.

4. The driven Fermi sea

The discussion of the previous paragraph combines the effect of a chiral propagation at constant velocity with the effect of a classical voltage drive, thereby introducing an effective filtering of the time dependent voltage. Such a filtering is, in first approximation, not present when considering a driven Ohmic contact. A large Ohmic contact is expected to act as a reservoir for electrons submitted to the time dependent ac voltage $V_{\rm ac}(t)$ applied to the contact. Consequently, all the single electron states get the time dependent phase

$$\phi(t) = \frac{e}{\hbar}\int_{-\infty}^{t} V_{\rm ac}(t')\,{\rm d}t' \tag{70}$$

The dc component of the voltage $V_{\rm dc}$ applied to the Ohmic contact determines the chemical potential of the electrons emitted $\mu = -eV_{\rm dc}$. Consequently, a large Ohmic contact driven by the potential $V(t) = V_{\rm dc} + V_{\rm ac}(t)$ emits a stream of electrons whose single electron coherence is

$$\mathcal{G}^{(e)}(t,t') = \frac{e^{-\omega_{\rm dc}(t-t')}}{t-t'+i0^+}\, e^{\frac{ie}{\hbar}\int_{t'}^{t} V_{\rm ac}(\tau)\,{\rm d}\tau} \tag{71}$$

in which $\omega_{\rm dc} = -eV_{\rm dc}/\hbar$. Note that because all electrons get the same scattering phase, the corresponding many-body state is still an infinite-dimensional Slater determinant built from the single-particle states $|\psi_\omega[V]\rangle$ such that

$$\psi_\omega[V_{\rm ac}](t) = e^{\frac{ie}{\hbar}\int_{-\infty}^{t} V_{\rm ac}(\tau){\rm d}\tau}\,\frac{e^{-i\omega\tau}}{\sqrt{2\pi v_F}} \tag{72}$$

for $\omega \leq \omega_{\rm dc}$. These single particle states can be conveniently expressed in the basis of fixed energy single particle states $|\omega\rangle$ defined in Appendix A:

$$|\psi_\omega[V_{\rm ac}]\rangle = \int_{\mathbb{R}} F(\omega')\;|\omega+\omega'\rangle\;\frac{{\rm d}\omega'}{2\pi} \tag{73a}$$

$$F_{V_{\rm ac}}(\omega) = \int_{\mathbb{R}} e^{i\omega t}\, e^{i\phi(t)}\,{\rm d}t \tag{73b}$$

Assuming that the $V_{\rm ac}(t)$ it T-periodic, the exponential $\exp(i\phi(t))$ is also T-periodic and can therefore be decomposed in a Fourier series:

$$e^{i\phi(t)} = \sum_{n=-\infty}^{n=+\infty} p_n[V_{\rm ac}]\, e^{-2\pi i n f t} \tag{74}$$

where the complex amplitudes $p_n[V_{\rm ac}]$ are called the photo-assisted amplitudes. They represent the amplitude for $|n|$ photon of energy hf to be absorbed ($n>0$) or emitted ($n<0$) to the electrons. The coefficient $p_0[V_{\rm ac}]$ is the amplitude for the electron to absorb or emit no photon. Note that, although the single electron coherence of the Fermi sea is diagonal in frequency space, the single electron coherence given by Eq. (71) is non zero off the frequency space's diagonal. This arises from the transfer of coherences between states of different photon numbers[9]. It can therefore be seen as the transfer of electromagnetic coherences to the electron fluid. As pointed out in Ref. [57], this transfer of coherence from the electromagnetic field to the electron fluid ensures that the quantum noise of the corresponding electrical current is the same than for an equilibrium state.

At zero temperature, the resulting single electron Wigner distribution function is of the form [57]:

$$W^{(e)}(t,\omega) = \sum_{(n_+,n_-)\in\mathbb{Z}^2} p_{n_+}[V_{\rm ac}]\, p_{n_-}[V_{\rm ac}]^*\, e^{2\pi i(n_- - n_+)ft}\Theta(\omega_{\rm dc} + \pi(n_+ + n_-)f - \omega) \tag{75}$$

and therefore exhibit discontinuities for $\omega - \omega_{\rm dc}$ being a multiple of πf which reflect the discreteness of photons of energy hf. Averaging over time leads to the electronic distribution function which is then equal to

$$f_e(\omega) = \sum_{n\in\mathbb{Z}} |p_n[V_{\rm ac}]|^2\;\Theta(\omega_{\rm dc} + 2\pi n f - \omega) \tag{76}$$

---

[9] Remember that a classical drive corresponds to a coherent state of the quantum electromagnetic field.

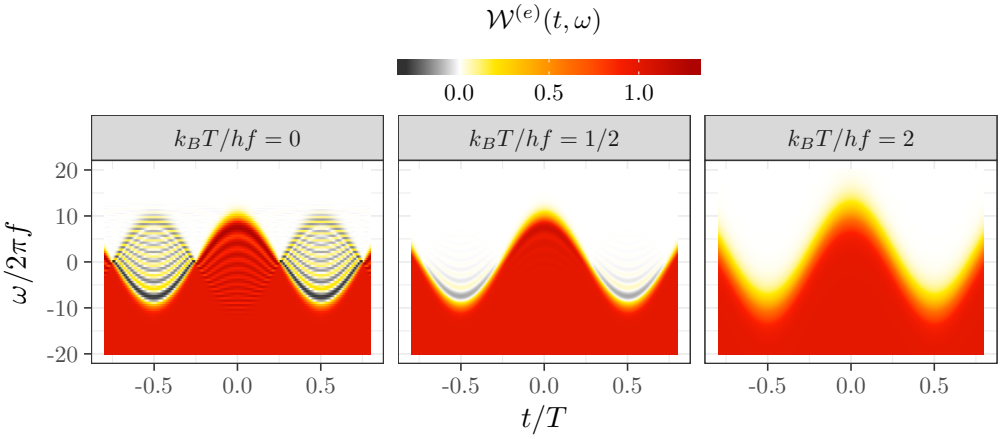

FIG. 10. (Reproduced from [20]) Wigner representation of a sinusoidal voltage drive $V_{\rm ac}(t) = V_0\cos(2\pi ft)$ at large amplitude ($eV_0/hf = 10$) and for increasing temperatures: for $k_BT_{\rm el} = 2hf$, the Wigner distribution corresponds to an agitated Fermi sea at temperature $T_{\rm el}$ and chemical potential $\mu(t) = eV_0\cos(2\pi ft)$. When the temperature is decreased, we see quantum interference effects leading to non-classical values of the Wigner distribution function.

which confirms the interpretation of $p_n[V_{ac}]$ as the amplitude for transferring energy nhf to the electron fluid.

Reference [57] contains a discussion of the sinusoidal drive $V_{\rm ac}(t) = V_0\cos(2\pi ft)$ for which $p_n = J_n(eV_0/hf)$ and $\omega_{\rm dc} = 0$. In the small amplitude limit $eV_0 \ll hf$, the physics is dominated by single electron processes as can be seen on Fig. 11. At first order in eV_0/hf, single electron coherence is non vanishing in a band $|\omega| \leq \pi h$ which gives the average electrical current $(e^2/h) \times V_0\cos(2\pi ft)$ but does not contribute to the electronic distribution function. This contribution really reflects the coherence transferred by the $|0\rangle + (eV_0/hf)\,|1\rangle$ photon state to the electronic fluid. The electronic distribution function is altered at order $(eV_0/hf)^2$ with electrons being transferred from the $-hf \leq \hbar\omega < 0$ energy band to the $0 \leq \hbar\omega < hf$ energy band.

In the large amplitude limit ($eV_0 \gg hf$), at zero temperature, quantum effects manifest themselves as a departure from the resulting electronic Wigner distribution function consists of a classical time dependent electronic distribution

$$W^{(e)}_{\rm cl}(t,\omega) = f_{e,T_{\rm el}=0\,\rm K}(eV(t)+\omega) \tag{77}$$

where $-eV(t)$ plays the role of a time dependent chemical potential. Fig. 10 shows that, this classical image is altered by the presence of quantum ripples which have indeed the same origin as the ones discussed in Section II D 1. They arise from the time variation of the time-dependent voltage $V(t')$ on the time-scale τ around t.

To conclude this discussion of the driven Fermi sea, let us review the important case of Leviton pulses. These are Lorentzian voltage pulses

$$V(t) = \frac{V_0}{1+(t/\tau_0)^2} \tag{78}$$

carrying an integer multiple of the $-e$ single electron charge. This is achieved when the amplitude of the pulse satisfies

$$Q = \int_{-\infty}^{+\infty} \frac{e^2}{h} V(t)\,{\rm d}t = \frac{\pi e^2 V_0\tau_0}{h} = -ne \tag{79}$$

as in Eq. (12) discussed in Section I. Hence for an n-Leviton pulse one has to chose the amplitude $V_0 = nh/(e\pi\tau_0)$. The corresponding time-dependent phase is then:

$$e^{i\phi(t)} = e^{\frac{e}{\hbar}\int_{-\infty}^{t} V(t')\,{\rm d}t'} = (-1)^n \left(\frac{\tau_0 - it}{\tau_0 + it}\right)^n . \tag{80}$$

For $n = 1$, this shows that each single particle state $|\omega\rangle$ is scattered into

$$\mathbb{S}_1\,|\omega\rangle = |\omega\rangle + 2\tau_0 \int_0^{+\infty} e^{-\omega'\tau_0}\,|\omega+\omega'\rangle\,{\rm d}\omega' \tag{81}$$

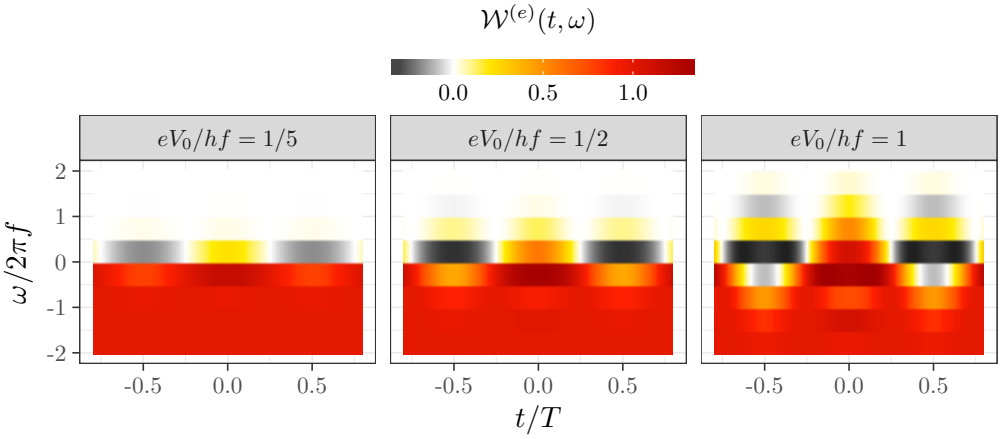

FIG. 11. (Reproduced from [20]) Wigner representation of a sinusoidal voltage drive at low amplitude ($|eV_0| \lesssim hf$) and zero temperature. At low voltage (right panel), the coherence is dominated by the linear term in V_0 which contributes to the average electrical current but not to the excess occcupation number. At increasing voltages (middle panel), the quadratic contribution in eV_0/hf appears which corresponds to real single-photon transitions. Then at higher voltages, the contribution of two-photon transitions becomes visible, progressively leading to the appearance of a sine-shaped Wigner function. Note that, in this regime, negative and greater than one values are visible on all the panels.

This rewriting enables us to describe in a simple way what happens to the Fermi sea with reference chemical potential $\mu = 0$: all the negative energy eigenstates are reshuffled therefore leading to another infinite dimensional Slater determinant but, because each $|\omega\rangle$ is scattered into a linear combination of $|\omega\rangle$ and higher energy states $|\omega + \omega'\rangle$ for $\omega' \geq 0$, all the negative energy single particle states remain present in the final infinite dimensional Slater determinant. Consequently, we come to the conclusion that, remarkably, the Fermi sea is preserved. However, we still have to determine the excitations present on top of it in the final many-body state. Fortunately, a miracle occurs due to the multiplicative properties of the exponential: for $\omega < 0$, $\mathbb{S}_1 |\omega\rangle$ contains a contribution in the state $\mathcal{H}_+$ of positive energy states which is

$$2\tau_0 \int_{-\omega}^{+\infty} e^{-\omega'\tau_0} |\omega + \omega'\rangle \, \mathrm{d}\omega' = 2\tau_0 e^{\omega\tau_0} \int_0^{+\infty} e^{-\omega''\tau_0} |\omega''\rangle \, \mathrm{d}\omega'' \tag{82}$$

Consequently, all negative energy states contribute to the same single particle state in the infinite dimensional Slater determinant as noticed in Ref. [26]. The final infinite dimensional Slater determinant therefore involves only one single electron excitation on top of the reference Fermi sea $|F_{\mu=0}\rangle$ which is

$$|\mathrm{Lev}_{\tau_0}\rangle = \sqrt{2\tau_0} \int_0^{+\infty} e^{-\omega\tau_0} |\omega\rangle \, \mathrm{d}\omega \, . \tag{83}$$

For $n > 1$, the single particle scattering matrix $\mathbb{S}_n = (\mathbb{S}_1)^n$ is more complicated: it does not generate only one single excitation on top of the Fermi sea but $n > 1$. More precisely, the charge $-ne$ Lorentzian pulse is a Slater determinant built from the single particle states $|\varphi_{k,\tau_0}\rangle$ from $k = 1$ to $k = n$ whose wavefunctions in the energy domain has been derived in Ref. [92]:

$$\langle\omega|\varphi_{k,\tau_0}\rangle = \sqrt{2\tau_0}\, \Theta(\omega)\, e^{-\omega\tau_0} L_{k-1}(2\omega\tau_0) \tag{84}$$

where $L_k(X)$ denotes the k-th Laguerre polynomial. Their Wigner function are depicted on Fig. 6 for $k = 1$ to $k = 4$.

E. Ideal electronic interferometers as on-chip quantum signal processors / Interferometric sensing

We will now discuss how ideal electronic interferometers can be viewed as "on-chip" quantum signal processors that encode the result of transformations performed on electronic quantum coherences into measurable quantities such as average electrical currents or low frequency current noise [28]. This general idea is crucial in the perspective of quantum sensing with single electron wave packets since it enables is to collect the information stored within electronic

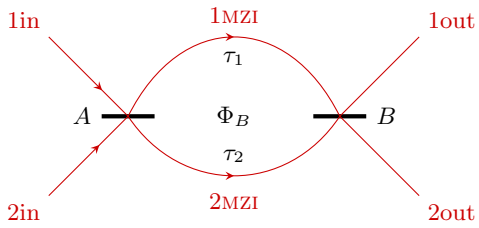

FIG. 12. Schematic view of the Mach-Zehnder interferometer: the incoming channels are partitionned at the electronic beam splitter A and then recombined by the beam splitter B. Here τ_1 and τ_2 denote the times of flight across the two branches of the MZI and Φ_B the magnetic flux enclosed by the interferometer.

quantum coherences using a measurement apparatus thereby opening the way to retrieving quantities that have been imprinted in them via the quantum sensors under study.

In this section, quantum sensing will not be discussed but we will focus on the way ideal electronic interferometers transform incoming electronic coherences into observable quantities by discussing two important examples of ideal single particle interferometers (the Mach-Zehnder interferometer and a time dependent filter), and the Hong-Ou-Mandel interferometer which involves two electron interferences. The generalized Franson interferometer, which is a two-electron interferometers have been theoretically discussed in Ref. [53] for accessing two-electron excess coherence introduced in Eq. (26c) can also be discussed along the same lines but has not been experimentally demonstrated yet.

1. *The Mach-Zehnder interferometer*

Let us start with an ideal Mach-Zehnder interferometer (MZI) depicted on Fig. 12 with an electron source S connected to the incoming channel 1. The average time dependent electrical current $\langle i_{1\mathrm{out}}(t)\rangle$ is related to the incoming excess single electron coherence by[28, 57, 93]:

$$\langle i_{1\mathrm{out}}(t)\rangle = \sum_{j=1,2} \mathcal{M}_{j,j}\langle i_S(t-\tau_j)\rangle - 2e|\mathcal{M}_{1,2}|\int_{\mathbb{R}} \cos\left(\omega\tau_{12}+\phi\right)\Delta W_S^{(e)}(t-\bar{\tau},\omega)\,\frac{\mathrm{d}\omega}{2\pi} \tag{85}$$

in which the $\mathcal{M}_{i,j}$ coefficients can be computed from the scattering matrices of the beam splitters A and B, $\phi = e\Phi_B/h$ denotes the normalized magnetic flux enclosed by the interferometer and $\tau_{12} = \tau_1 - \tau_2$ and $\bar{\tau} = (\tau_1+\tau_2)/2$ respectively denote the difference and average of the time of flights across the two branches of the interferometer. Its magnetic flux dependent part is directly related to the excess Wigner function of S, enabling a direct read out of its time dependence as well as its ω dependence by varying the difference of times of flights across the two branches of the MZI.

2. *Time dependent filtering at a QPC*

Another example of the same type is the time dependent filter discussed by Locane *et al* [62] which consists of a driven quantum point contact with a frequency dependent transmission $T(\omega)$ as depicted in Fig. 13. A classical time dependent voltage $V_d(t)$ is applied to a top gate, thereby leading to the transmission of specific scattering states. This device can be viewed as a generalization of the stationary quantum dot used to probe the electron distribution function within quantum Hall edge channels [94]. The signal of interest is the average electric charge $\langle Q\rangle$ transmitted across the filter which is, once again, the result of a linear filtering on the incoming excess single electron coherence $\Delta\mathcal{G}_S^{(e)}$:

$$\langle Q\rangle = -e\int_{\mathbb{R}^2} v_F\Delta\mathcal{G}_S^{(e)}\left(t+\frac{\tau}{2},t-\frac{\tau}{2}\right)\mathcal{F}_d(t,\tau)^*\,\mathrm{d}t\,\mathrm{d}\tau \tag{86}$$

where the filter's kernel is given by

$$\mathcal{F}_d(t,\tau) = \int_{\mathbb{R}} T(\omega)\,\mathrm{e}^{\mathrm{i}\omega\tau+\frac{\mathrm{i}e}{\hbar}\int_{t-\tau/2}^{t+\tau/2}\mathcal{V}_d(t')\mathrm{d}t'}\frac{\mathrm{d}\omega}{2\pi} \tag{87}$$

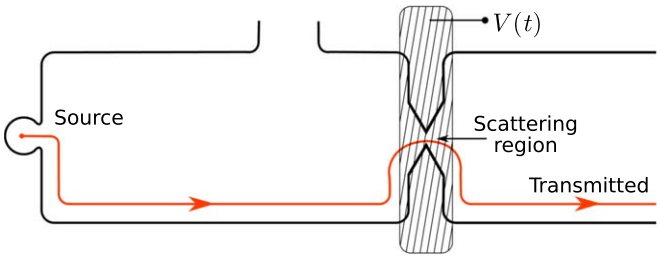

FIG. 13. (Fig. reproduced from [62]) A quantum point contact with energy dependent transmission is driven by a top gate to which a time dependent voltage $V_d(t)$ is applied. It is assumed that along all their propagation below the top gate the electrons feel the spatially uniform voltage $V_d(t)$. The source S is located on one of the incoming edge channels arriving at the QPC whereas the other incoming channel is connected to the ground.

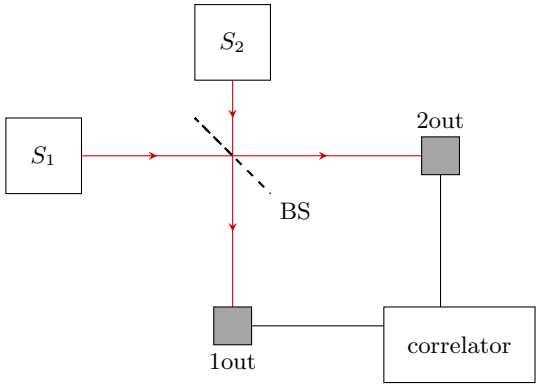

FIG. 14. (Reproduced from [28]) Principle of the HOM experiment: excitations emitted by two independent sources S_1 and S_2 are sent onto a beam splitter BS. In optics, one performs a time-resolved detection of photons. In the electronic case, the beamsplitter is a QPC and one measures current correlations between 1out and 2out or current noise in the 1out channel. In the case of the HBT experiment, vacuum is replaced by the reference Fermi sea.

in which

$$\mathcal{V}_d(t) = \int_{-\infty}^{x} (\partial_x U)\,(x, t - x/v_F)\mathrm{d}x \tag{88}$$

in which $U(x,t) = \mathcal{V}_d(t)u(x)$ denotes the voltage seen by the electrons as they fly across the QPC[10]. As explained in [62], this time dependent filter can be used to perform quantum tomography of the single electron coherence $\Delta\mathcal{G}_S^{(e)}$ by utilizing linear-in-time modulation and a sufficiently energy-selective $T(\omega)$. Experimental realization of such a protocol and its classical interpretation are discussed in [32] and summarized in Section III A 4 below.

3. The Hong-Ou-Mandel interferometer

The setup depicted on Fig. 13 is indeed very close to a Hong-Ou-Mandel (HOM) interferometer. The crucial difference is that the HOM interferometer probes two particle interferences whereas the time dependent filter is based on single particle interferences. However, an ideal HOM interferometer can also be used to perform single electron tomography and can indeed be described as a kind of filtering on the unknown single electron coherence one wishes to reconstruct. In a HOM interferometer, two particle interferences between two independent sources S_1 and S_2 are probed by looking at correlations after a beam-splitter as depicted on Fig. 14. This experiment has been first demonstrated in optics, using photons emitted by two independent sources [95], and since then has been reproduced in many different contexts in optics and beyond (see [96] for an extensive recent review), in particular with fermionic and

[10] $u(x)$ is non zero close to the constriction of the QPC and rapidly vanishes away from it.

bosonic cold Helium atoms [97] and with single electron excitations propagating within quantum Hall edge channels [98].

The signal of interest is the excess low-frequency current noise just after the QPC when both sources S_1 and S_2 are switched on. It is the sum of three contributions [57]:

$$\Delta S_{11}^{(S_1\&S_2)} = \Delta S_{11}^{(S_1)} + \Delta S_{11}^{(S_2)} + \Delta S_{11}^{(\mathrm{HOM})}, \tag{89}$$

where $\Delta S_{11}^{(S_1)}$ and $\Delta S_{11}^{(S_2)}$ are the excess current noises when only the source S_j ($j = 1,\ 2$) is switched on. These terms are given by:

$$\Delta S_{11}^{(S_1)} = e^2T^2 \int_{\mathbb{R}} \overline{\Delta W_{S_1}^{(e)}(t,\omega)}^{t}\ (1-2f_{\mathrm{eq}})\,(\omega)\frac{\mathrm{d}\omega}{2\pi}. \tag{90a}$$

$$\Delta S_{11}^{(S_2)} = e^2R^2 \int_{\mathbb{R}} \overline{\Delta W_{S_2}^{(e)}(t,\omega)}^{t}\ (1-2f_{\mathrm{eq}})\,(\omega)\frac{\mathrm{d}\omega}{2\pi}. \tag{90b}$$

where R and T denote the reflection and transmission probabilities of the QPC and f_{eq} the equilibrium Fermi distribution of the incoming channels. These terms correspond to the excess noise in Handburry Brown and Twiss (HBT) experiments performed on each of the sources. Since $1-2f_{\mathrm{eq}}(\omega) = \tanh\left(\hbar\omega/2k_BT_{\mathrm{el}}\right)$ this expression counts the total number of excitations (electrons and hole) whose energy are above k_BT_{el} injected by the source S_j. When the other channel (called the probe) is at zero temperature, it is exactly the total number of excitations injected by S_j. This quantity has been measured for a single-electron source in quantum Hall edge channel in Ref. [99].

The last term, called the HOM contribution since it requires both sources to be switched on, is given by

$$\Delta S_{11}^{(\mathrm{HOM})} = -2e^2RT \int_{\mathbb{R}^2} \overline{\Delta W_{1\mathrm{in}}^{(e)}(t,\omega)\Delta W_{2\mathrm{in}}^{(e)}(t,\omega)}^{t}\ \frac{\mathrm{d}\omega}{2\pi}, \tag{91}$$

where $\overline{\cdots}^{t}$ denotes the average over time t. The HOM signal thus directly represents the overlap of the excess single-electron coherences arriving at the QPC [57]. Equation (91) encodes the effect of two-particle interferences between the excitations emitted by these sources. Note that the time delay of the two sources can be controlled and, therefore, a single experimental run gives access to the time-shifted overlaps of the excess electronic Wigner functions of the two sources. Finally, the minus sign comes from the fermionic statistics of electrons. Viewing $\Delta W_{1\mathrm{in}}^{(e)}$ as the unknown quantum signal $\Delta W_{S}^{(e)}$ and $\Delta W_{2\mathrm{in}}^{(e)}$ as a well controlled probe signal, Eq. (91) thus appears once again as a linear filtering equation connecting the signal to be reconstructed to the measured quantity $\Delta S_{11}^{(\mathrm{HOM})}$. This time, the filter is nothing but the probe signal $\Delta W_{2\mathrm{in}}^{(e)}$. Hence Eq. (91) expresses the fundamental principle behind the HOM-based general tomography protocol for low energy electrons described in Section III A 2.

One thus immediately sees the formal analogy between the tomography protocols based on time-dependent single particle scattering [32] and on two-particle interferences [52], respectively. Both of them lead to a linear filtering of the unknown incoming single electron coherence, connecting the unknown quantum signal to the experimentally measured quantity. Experimental demonstrations of these two different tomography techniques are reviewed in Section III A.

F. Interaction effects

Let us now consider the effects of interactions on single electron excitation. In this section, we will first show that Coulomb interactions between two single electron excitations propagating in nano-structures do induce a significative change of phase. A detrimental effect is Coulomb interaction induced electronic decoherence which will be briefly reviewed. But this also opens the way to using single electron excitations as a probe of rapidly varying electromagnetic fields as well as of fast and efficient detection of single charges, two examples that are at the core of the SEQUOIA project.

1. Two-electron interaction

Let us estimate the phase variation induced by the interaction of two single electrons propagating at velocity v_F in opposite directions along two parallel 1D edge channels separated by a distance d. For simplicity, we consider the effect of unscreened Coulomb interactions along a distance l and assume that the two particles meet at minimal distance at the center of this interaction region. The Coulomb interaction induced phase shift is associated with the

effect of the Coulomb potential $V_{\rm C}(\mathbf{r}) = e/(4\pi\varepsilon_0\varepsilon_r|\mathbf{r}|)$ induced by one electron on the other within the material of relative permittivity ε_r ($\varepsilon_r \simeq 12.9$ for GaAs):

$$\delta\phi_{\rm coll} = \frac{e}{\hbar}\int V_{\rm C}(\mathbf{r}(t))\,{\rm d}t \tag{92}$$

in which $\mathbf{r}(t)$ denotes the relative coordinate of the two electron system. An explicit computation leads to $\delta\phi_{\rm coll} = \alpha_{\rm eff}F(l/d)$ where

$$\alpha_{\rm eff} = \frac{e^2}{4\pi\varepsilon_0\varepsilon_r\hbar v_F} = \frac{\alpha_{\rm qed}}{\varepsilon_r}\,\frac{c}{v_F} \tag{93}$$

is the effective fine structure constant within the material ($\alpha_{\rm qed} = 1/137.035999084(21)$ being the fine structure constant in vacuum) describing the effective strength of electromagnetic interactions for the electrons in the present case and

$$F\left(\frac{l}{d}\right) = {\rm arcsinh}\left(\frac{l}{d}\right) = \begin{cases} l/d & l \ll d \\ \ln(2\,l/d) & l \gg d \end{cases} \tag{94}$$

encodes the geometry considered here. In the present situation, it increases linearily with l in the limit of a short ($l \ll d$) region and then crosses over to a logarithmic behavior for a long interaction region ($l \gg d$). This shows that in AlGaAs/GaAs systems the effective coupling can indeed be quite large: $\alpha_{\rm eff} \sim 1.7$ for $v_F = 1\times10^5\,{\rm ms}^{-1}$. For $l \sim 1\,\mu{\rm m}$ and $d = 100\,{\rm nm}$, $\delta\phi_{\rm coll} \sim 2\pi\times0.81$ thereby implying the relevance of single excitations for detecting potential fluctuations created by sub-single electron charge within a sub-micrometric device. It is however important to point out that in the situation considered here such a phase kick occurs on a very short time scale: 10 ps for $l = 1\,\mu{\rm m}$ and $v_F = 1\times10^5\,{\rm ms}^{-1}$.

Another model geometry that can capture interaction of two counterpropagating modes is a saddle point potential [100] $V(x,y) = m\,\omega_y^2\,y^2/2 - m\,\omega_x^2\,x^2/2$. This model is also particularly suitable for description of two isolated electrons [101]. A single electron, localized by a strong magnetic field in a well-defined Landau level, undergoes $\mathbf{E}\times\mathbf{B}$ drift [50] along the equipotential lines. For the saddle point potential, the corresponding guiding centre trajectory is a hyperbola with a local velocity $\mathbf{v} = -\omega_c^{-1}\{\omega_y^2 y, \omega_x^2 x\}$, where $\omega_c = eB/m \gg \omega_x, \omega_y$ is the cyclotron frequency.

Neglecting the classical backaction (change of trajectory due to interaction), the relative coordinate follows the same set of hyperbolic trajectories with $\mathbf{r}(t) = \sqrt{d^2\cosh^2(\omega_0 t) + l^2\,\sinh^2(\omega_0 t)}$ where $\omega_0 = \omega_x\,\omega_y/\omega_c$, d is the minimal distance, $v_{\rm min}$ is the minimal relative velocity (both reached at $t = 0$), and $l = v_{\rm min}/\omega_0$ is the characteristic size in the longitudinal direction. $l/d = \omega_y/\omega_x$ for electrons passing each other along x (in the opposite case of passing along y, $l/d = \omega_x/\omega_y$)).

The corresponding phase shift accumulated by one electron due to the presence of the other can be estimated perturbatively from Eq. (92) as

$$\delta\phi = \alpha_{\rm eff}\times\frac{2\,l}{d}K(-l^2/d^2) \tag{95}$$

where K is the complete elliptic integral of the first kind and v_F in Eq. (93) for $\alpha_{\rm eff}$ has to be replaced by $v_{\rm min}$. We get essentially the same result as the estimate for the straight channels as the asymptotics of Eq. (95) is similar to that of $F(l/d)$, cf. (94) above,

$$\frac{2\,l}{d}K\left(-\frac{l^2}{d^2}\right) = \begin{cases} \pi l/d & l \ll d \\ 2\ln(4\,l/d) & l \gg d \end{cases} \tag{96}$$

In the strong electron-electron coupling regime, $\delta\phi \gg 1$, presence of the other electron may significantly alter the classical trajectories, and a non-perturbative treatment of interactions becomes necessary. For the two collision problem, fully self-consistent classical treatment of Coulomb interactions at the saddle point [101] reveals significant renormalization of the transmission threshold and thus potential for singe-shot sensing of coincident arrival.

2. Electronic decoherence

Considerations of the previous paragraph show that electron/electron interactions within a quantum conductor can lead to significant phase shifts for electrons. As we shall now discuss this is at the root of a key phenomenon in

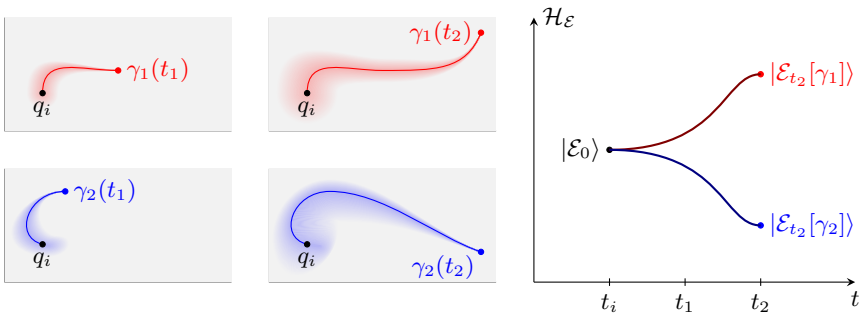

FIG. 15. (Figure reproduced from [105]) Schematic view of the evolution of the state of environmental degrees of freedom in $|\mathcal{E}_0[\gamma]\rangle$ as the particle (or system) follows a trajectory γ_1 or γ_2 (see left panel). At the initial time, the environment is in its initial state $|\mathcal{E}_0\rangle$ (pure for simplicity) and as time increases the two imprints $|\mathcal{E}_t[\gamma_a]\rangle$ for $a = 1$ and $a = 2$ become more and more distinguishable therefore killing interferences between the different trajectories and leading to decoherence.

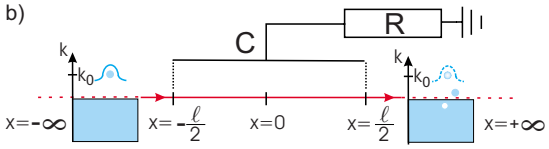

FIG. 16. (Figure reproduced from [106]) Electrons propagating along a chiral edge channel at constant and uniform velocity v_F in the presence of a top gate of length l connecting to a resistance R which provides the environmental degrees of freedom. An electron injected in the incoming channel will then experience electronic decoherence due to the coupling to external degrees of freedom and also, when a Fermi sea is present, due to electron/electron interactions.

mesoscopic physics: electronic decoherence. Within a path integral point of view, a single electron propagating within a quantum conductor from an initial state $I = (r_i, t_i)$ to a final state $F = (r_f, t_f)$ explores all the possible trajectories connecting these two points. As illustrated on Fig. 15, two different trajectories γ_+ and γ_- leave different "quantum imprints" in its environment which involves all the quantum degrees of freedom it is interacting with. In particular, among them could be the charge degrees of freedom of the other electrons: each of this electron will feel the Coulomb interaction induced phase shift associated with the motion of the electron along its trajectory which obviously is not the same for γ_+ or for γ_-. Therefore, these different imprints carry some which-path information on the trajectories and, as is well known from Feynman & Vernon work [102], it leads to a contrast reduction for the interference between γ_+ and γ_-. This is the general idea behind decoherence theory (see Ref. [103, 104] for extensive reviews) rephrased in the context of coherent electronic transport.

It is particularly well suited to the description of electronic decoherence for "high energy electrons" which propagated into depleted channels because, due to their confinement, they can be viewed as "distinct" from all the other electrons present in the sample, such as the one present in side gates or within distinct but undepleted channels.

A discussion of electronic decoherence for solitary ballistic electrons propagating at speed v_F beneath a metallic top gate of finite length l (see Fig. 16) can be found in Ref. [106]. The top gate is connected to a finite resistance R which is equivalent to a transmission line [107]. The resulting RC-circuit thus provides the environmental degrees of freedom leading to electronic decoherence. Neglecting the back-action from this environment onto the electron, one can compute how spatial coherence of the solitary electron in single particle state $|\varphi_e\rangle$ is altered after its passing beneath the gate. We denote by $\mathcal{G}^{(e)}_{\rm in}(x_i, x'_i) = \varphi_e(x_i)\,\varphi_e(x'_i)^*$ the incoming spatial single electron coherence with $x_i < -l/2$ and $x'_i < -l/2$ being located before the gate. After a sufficient time t, the final positions $x_f = x_i + v_F t$ and $x'_f = x_i + v_F$ are located after the gate, in the $x > l/2$ region. The outgoing spatial electronic coherence and $\mathcal{G}^{(e)}_{\rm out}(x_f, x'_f)$ is then related to the incoming one by [106]

$$\mathcal{G}^{(e)}_{\rm out}(x_f, x'_f) = \mathcal{G}^{(e)}_{\rm in}(x_i, x'_i)\mathcal{D}_t(x_f, x'_f) \tag{97}$$

in which $\phi_\pm$ represent the forward scattering phase induced by the presence of the gate and the decoherence coefficient $\mathcal{D}_t(x_f, x'_f)$ is associated with the overlaps left by the two different classical trajectories, respectively connecting $(x_i, 0)$ to $(x_i + v_F t, t)$ and $(x'_i, 0)$ to $(x'_i + v_F t, t)$.

In the "scattering limit" where $t \to +\infty$, (x_i, x'_i) being far on the $x \to -\infty$ and (x_f, x'_f) far on the $x \gg l/2$ parts of the x axis, $D_f(x_f, x'_f)$ is expected to only depend on $d = x_f - x'_f = x_i - x'_i$. In this limit the difference of the two

scattering phases $\phi_\pm = \frac{e^2}{2\hbar C}\int_0^t f(x_f^\pm - v_F\tau)^2 \mathrm{d}\tau$ is also expected to vanish. Consequently, we are left with

$$\mathcal{G}^{(e)}_{\rm out}(x_f, x'_f) = \mathcal{D}_\infty(x_f - x'_f)\,\mathcal{G}^{(e)}_{\rm in}(x_i, x'_i) \tag{98}$$

where $\mathcal{D}_\infty(x_f - x'_f)$ is the asymptotic decoherence coefficient describing decoherence induced by the interaction with the RC-circuit. This transformation of the single electron coherence replaces the chiral dispersionless propagation equation (Eq. (45)) and even more generally the transformation under coherent single particle scattering (Eq. (54)) which does not involve any decoherence coefficient. In terms of Wigner functions in the (x, k) space, this leads to

$$W^{(e)}_{\rm out}(x_{\rm out}, k) = \int_{\mathbb{R}} \widetilde{\mathcal{D}}_\infty(q)\, W^{(e)}_{\rm in}(x_{\rm in}, k-q)\,\mathrm{d}q \tag{99}$$

where $x_{\rm out} = x_{\rm in} + v_F t$ under the hypothesis that $x_{\rm out} \gg l/2$, $-x_{\rm in} \gg l/2$ and t being sufficiently large, and $\widetilde{\mathcal{D}}_\infty(q)$ is the Fourier transform of the decoherence coefficient $\mathcal{D}_\infty(x)$. Note that the effect of the interaction region is to spread the Wigner function in k independently of x, a way that reflects spatial translation invariance in the scattering limit, a consequence of time translation invariance of the dynamics itself. Such an equation is very reminiscent of $P(E)$ theory in the context of the dynamical Coulomb blockade [82] except that here it is expressed in momentum space. Since, in the asymptotic regions $x \to \pm\infty$, we are dealing with chiral dispersionless fermions with linear dispersion relation $\omega(k) = v_F k$, Eq. (99) is indeed an equation describing the energy change of the single electron due to its interaction with the RC circuit in the $|x| \leq l/2$ region. At zero temperature, $\widetilde{\mathcal{D}}_\infty(q) \neq 0$ only for $q \leq 0$ and therefore, only energy emission is possible. The energy lost by the electron is dissipated in the resistance R or, in the transmission line language, corresponds to the energy of the outgoing photons emitted into the transmission line.

Although this simplified model explains electronic decoherence and relaxation for solitary electrons, it is not sufficient to describe electronic decoherence associated with electron/electron interactions in the presence of the Fermi sea. In principle, if one injects a single electron excitation well above the Fermi sea, and if electronic decoherence does not smash it back onto the Fermi sea, one could view the electrons within the Fermi sea as distinct environmental degrees of freedom. Instead of imprinting information on spatially separated degrees of freedom as in the example discussed above, one would also imprint information in the charge density modes of the edge channel with energies much smaller than the initial and final energies of the electron we are considering. Instead of generating photons in an external circuit, the incoming electron would emit low energy charge density wave in the channel where it is propagating.

However, the full single electron coherence does not reduce to the contribution of the injected solitary electron. As explained in Section II B, the excess single electron coherence will get a contribution $\Delta\mathcal{G}^{(e)}_{\rm e/h\ pairs}$ from the coherent electron/hole pairs generated by Coulomb interactions. What is expected is an excess contribution of the form:

$$\Delta\mathcal{G}^{(e)}_{\rm out}(x_f, x'_f) = \mathcal{D}_\infty(x_f, x'_f)\,\varphi_{e,\rm out}(x_f)\,\varphi_{e,\rm out}(x'_f)^* + \Delta\mathcal{G}^{(e)}_{\rm e/h\ pairs}(x_f, x'_f) \tag{100}$$

in which $\varphi_{e,\rm out}$ denotes the outgoing wave packet computed using free propagation. The electron/hole pair contribution may be evaluated by computing the effective many-body state of the EMP modes generated by the passing of the quantum solitary-electron.

It should be noted that the toy model of Ref. [106] uses an RC-circuit for the environment but in real systems one should analyze all the possible environmental degrees of freedom. In high energy electron quantum optics experiments the dispersion relation for electrons is no longer linear and electron/electron interactions are no longer the dominant mechanism for relaxation. In this regime, phonon emission becomes the dominant mechanism and this perfectly fits the framework of decoherence by an external bath. Detailed computations of the relaxation rate equations have been performed in Refs. [108, 109] based on the Fermi Golden rule and used in a master equations's approach to estimate electronic decoherence in MZI [109].

However, for low energy electron quantum optics experiments, these approaches are not the most suitable one for computing electronic decoherence in the presence of electron/electron interactions in the edge channel. Measurements of the relaxation of a non equilibrium stationary electronic distribution in a system of two copropagating quantum Hall edge channels [94] have shown that the electron quasi-particle does not survive in such a system after a distance inversely proportional to the typical injection energy scale ε [110], contrary to what would happen in a Fermi liquid where the typical relaxation length would scale as ε^{-2} [111]. This suggest that an energy resolved single electron excitation injected on top of the Fermi sea is smashed back onto the Fermi level. In this situation, this electron can no longer be considered as distinguishable by its energy from the ones in the Fermi sea and the above simple approach based on the effective separation between the quantum particle and its environment is not expected to work.

Fortunately, the problem of electronic decoherence in a chiral edge channel has been solved in full generality for single electron excitations traveling across an interaction region under the hypothesis that its environment responds linearly to charge density disturbances [80, 112, 113]. This approach, based on bosonization, is non-perturbative in

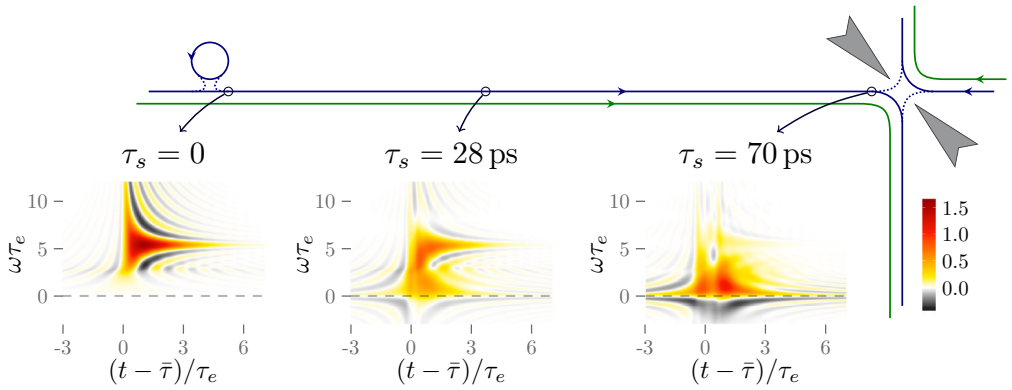

FIG. 17. (Figure reproduced from [114]) Destruction of a Landau quasi-particle in a system of two co-propagating quantum Hall edge channels: Wigner representation of the excess single electron coherence at $T_{\mathrm{el}} = 0\,\mathrm{K}$ for different propagation distances after it has been injected in the outer (blue) edge channel by a mesoscopic capacitor due to strong screened Coulomb interactions between the inner (green) and outer (blue) channel. The landau excitation has temporal width $\tau_e = 60\,\mathrm{ps}$ and is emitted at energy $\varepsilon/k_B = 0.7\,\mathrm{K}$ above the Fermi sea. The time axis are time translated to account for propagation. The time τ_s corresponds to the time of flight for the slowest collective EMP mode [115] and is typical of propagation along a few micrometers.

the interactions and automatically accounts for back-action of the external environmental degrees of freedom on the electron fluid in which the excitation under study has been injected. When the coupling to environmental degrees of freedom and electron/electron interactions are not too strong, it leads to a result of the form given by Eq. (100) [112, 113].

In the case of two-copropagating edge channels [80, 116], it explains why the electron does not survive as a quasi-particle (see Fig. 17). These predictions have been tested experimentally in an HOM experiment involving two mesoscopic capacitors used in the single electron source regime [114]. This enables testing one of its striking prediction which is the forgetting of the initial emission energy of the electrons during the 3 µm of propagation between the single electron-source and the HOM electronic beam splitter: the HOM curves only depends on the temporal width of each of the wave packets and not on their initial energies.

In the perspective of the SEQUOIA project, this approach provides a better understanding of electronic decoherence effects and opens a way to control electronic decoherence, and maybe to use it for further purposes:

- The robustness of Leviton excitations to electronic decoherence compared to Landau quasi-particles emitted by the mesoscopic capacitor arises from the fact that these are coherent states of edge-magnetoplasmons and therefore, these are pointer states with respect to the electromagnetic environment of the quantum edge channel [80].

- It explains the weakness of electronic decoherence in graphene, first observed in a Mach-Zehnder interferometry experiment [117] by the combination of two factors: due to the higher value of v_F in graphene, at fixed energy scale, the experimentally demonstrated graphene interferometers are much smaller than their AlGaAs/GaAs counterparts. But more importantly, the effective coupling constant characterizing the intensity of electromagnetic-interactions responsible for electronic decoherence

$$\alpha_{\mathrm{eff}} = \frac{e^2}{4\pi\varepsilon_0\varepsilon_r\hbar v_F} = \frac{\alpha_{\mathrm{qed}}}{\varepsilon_r}\,\frac{c}{v_F} \tag{101}$$

  is smaller in graphene than in AlGaAs/GaAs [113].

- It confirms that a clever design of sample can be used to fight electronic decoherence by cutting-off the emission of edge-magnetoplasmons in nearby quantum edge channels [113], a fact already explored in experiments [118–120]. Interestingly, it also suggests that the emission of a single electron excitation could be heralded by a single photon emission with a suitable sample design [113].

3. Using single electrons for quantum sensing

Section II F 1 strongly suggests that a single electron excitation could be used to detect very small and fast variation of the electrical potential via the associated phase shift. Measuring phase is always done by comparison with a reference and, following the discussion of Section II E 1 this suggests to use an electronic interferometer for that purpose. The principle is very similar to the one of a radar which uses a classical electromagnetic wave to probe, in a Mach-Zehnder like design, how a target scatters these electromagnetic waves. However, in the present case, a single electron wavefunction is used to probe a time-dependent electromagnetic field. Since, as explained in Section II there is nothing like the classical amplitude for a fermionic field, one can speak of quantum sensing of an electromagnetic field by a single electron interferometer.

In Section IV A, a first demonstration of this idea is presented: an electronic interferometer is used to compare propagation of a single electron excitation in the presence and in the absence of the coupling to a driven electrostatic gate (see Fig. 27). This experiment demonstrates the ability of an electronic interferometer used in the single electron regime to probe locally a time-dependent voltage with a temporal resolution of a few tens of ps limited by the duration of the electronic wave packet. Section IV B presents another illustration of this idea with the detection of magnons propagating across the bulk of a quantum Hall ferromagnet in graphene by a valley Mach-Zehnder interferometer.

However, this simple view does not take into account all aspects of the problem. Electronic decoherence discussed in the previous paragraph potentially jeopardizes the perspective of such quantum sensing of time dependent potentials by limiting the visibility of the interferometer. In the experiment presented in Section IV A, the amplitude of the time-dependent voltage drive was quite high and, electronic decoherence did not prevent the detection of the time dependent drive. However, if the prospect is to detect small time dependent signals such as the passing of a single electron in a nearby quantum Hall edge channel, the effect of electronic decoherence cannot be overlooked.

In full generality, the electron interferometer could be used to probe a quantum electromagnetic field, searching for signatures of non-classical fluctuations for example. One could even think of using a single electron interferometer to distinguish among different quantum states within a short time window. In such situations, a compromise has to be found on the coupling between the single electron interferometer and its electromagnetic environment: increasing the coupling seems to be good for sensitivity but may lead to strong decoherence effects and to strong feedback of the electronic interferometer on the field it is coupled to. Unfortunately, these effects tend to deteriorate the interference signal in the interferometer and therefore lower its performances. Characterizing and then optimizing the performances of such an interferometers thus ultimately requires developing a theoretical approach to electronic decoherence in the presence of an external quantum radiation.

III. APPLICATION CONCEPTS AND TECHNOLOGY TOOLBOX

Just as new theoretical techniques are needed for capturing the appropriate description of single electron physics, new experimental techniques are required to bolster the 'toolkit' used to configure and verify the performance of single-electron optics systems and components. In this section we present three new techniques/components advanced within the SEQUOIA project. Section III A introduces the spectrum of single-electron sources and explains the techniques used to probe the emission purity of these sources. Due to characteristic differences in the physical environment in which high energy electron sources operate (emission energy, screening), these had been lacking probes of coherence or emission purity analogous to those developed in low energy sources. This motivated the development of new techniques within the project which will be explained. Section III B introduces a new technique developed for capture and detection of individual single-electron wave packets. This enables an efficient readout of scattering outcomes as an alternative to noise measurements. It allows to access the full probability matrix of multi-electron scattering events, allowing for a single-electron based quantum metrology with enhanced signal quality and integrity, and also adds an exciting extension of the electron optics toolbox towards the use of quantum states with larger electron number. Finally, section III C reports on the evaluation of the dissipation mechanisms in the quantum Hall regime of h-BN encapsulated graphene. Graphene is a promising material for the formation of electron optics devices (see section IV B) and is already a familiar in the electrical metrology community due to its potential to make quantum Hall resistance metrology available to a broader user community. Such applications require a detailed understanding of relaxation effects.

A. Probing wave packets emitted from on-demand single-electron sources

Jonathan D. Fletcher and Masaya Kataoka

The thesis of the single-electron quantum optics approach is that it should be possible to isolate and control electronic excitations at the single particle level. Practical implementation of this requires single particle sources, device structures (e.g. quantum dots, low dimensional systems) and control regimes (e.g. RF drive techniques) through which excitations can be launched into appropriate edge channels for single electron transport. It also requires the means to verify things like the injection energy of the particles.

Mesoscopic capacitors [78], single electron pumps [121], Leviton sources [23] are examples of single particle sources defined in semiconductor systems. These three device types operate by i) electron/hole emission from a low energy quantum dot [78] ii) electron emission from a high energy quantum dot [30] iii) 'minimal' excitation electron by shaped voltages pulses [23]. Techniques have been developed to characterise the excitations that they inject into the external circuit and the ability of the above devices to inject single-electron/particle excitations on-demand. This process generally starts with basic characterisation of the charge transfer characteristics, source energy and emission time distribution and can eventually extend to a quantum tomographic reconstruction of the electronic excitation in the Wigner representation. While there are common aspects to this process between devices (e.g. use of some additional time-domain probe of the excitations) there are necessary adaptations required to suit the characteristic of each device. Of the three different sources, two of them, the mesoscopic capacitor and the leviton sources, inject excitations at relatively low energy, close to the Fermi sea, in an integer quantum hall edge state. Because of this similarity in energy, the techniques to characterise wave packets in these devices are more closely related than the techniques required for the very high injection energy [30]. Here we briefly review the factors that sets the energy and time scales of low and high energy devices and how this leads to different approaches for tomography of single electron wave packets.

1. Mesoscopic Capacitor and Levitons: Characteristic energy, times scales

The first source to demonstrate on-demand single electronic excitations appropriate for single electron quantum optics was a low energy quantum dot source [78]. These devices consist of a mesoscopic charge island, defined in a two-dimensional electron gas, coupled to quantum hall edge channel. Transport of electrons on and off the charge island is governed by Coulomb blockade (level spacing $\Delta \simeq 1$ meV) and the coupling barrier with transmission D which sets the tunnel rate to the edge channel. Modulation of the dot energy with a 'plunger' gate controlled by an AC voltage waveform toggles the dot between charge levels. At the correct operating point, the dot alternately ejects and admits single electrons into/from the adjacent quantum hall edge channel, which is tuned (by external magnetic field) to the $\nu = 2$ filling factor.

The AC charge current from these devices can be detected using RF techniques and can be quantized in units of $I = 2ef$, demonstrating on-demand alternating single-hole, single-electron injection [122]. Measurement and control of the emission time distribution within each pump cycle time is possible within certain bounds; if the tunnel rate is set too small the emission process is too slow to empty the dot and if it is too large the dot charge quantisation levels are broadened. As the injection takes place by tunneling, the emission distribution is expected to have an exponential decay with the width of this emission time distribution slightly smaller that the pumping period 0.3 – 3 ns. The injection energy is set by the energy scales of the dot energy modulation $\Delta/2$ with the exact distribution depending on the exact ejection dynamics, namely how rapidly the dot level is brought out of equilibrium with respect to the tunnel rate. If the dot level were raised instantaneously, the injection energy distribution would be a lorentzian peak at $E = \Delta/2$ [88, 89, 123]. A slow enough linear drive would also lead to a single electron excitation [124]. A more general analysis of the excitations emitted by the mesoscopic capacitor in terms of electronic atoms of signal (see Section II C 2) is presented in Ref. [29].

Information on the actual energy distribution can be extracted from measurements of the shot noise generated when electrons/holes from the source beam are partitioned randomly into two output channels by a quantum point contact in the beam path [99]. This is a scenario which lends some comparison with the optical configuration of the Hanbury Brown-Twiss (HBT) interferometer. In the elementary case, partitioning of a single-election frequency f at a barrier with transmission probability T produces shot noise $S_I = 2T(1-T)e^2 f$. This partition noise is a baseline against which correlations or interaction effects emerge, or through which effective excitation charge or number can be measured [74, 125]. Partitioning of electrons/holes from the mesoscopic capacitor revealed a current noise smaller than expected from the injection frequency. This was accompanied by a characteristic dependence on the waveform used to control emission conditions [99]. This revealed that the noise measured was not the result of simple partitioning but was influenced by antibunching, i.e. two particle interference with thermal excitations from the other side of the beam splitter which suppresses the noise (discussed below). The emission rate and quantum dot drive waveform

govern the injection energy distribution $\rho(E)$ which partially overlaps the thermal excitation energy scale set by kT. The manifestation of fermionic exchange statistics as two particle 'antibunching' is an effect that recalls the Hong Ou Mandel interference of quantum optics where 'bunching' of bosonic particles is observed [95]. This effect is driven by exchange statistics and constitutes a probe of particle indistinguishability. As a time/phase sensitive probe it also lies at the centre of technique to provide a full tomography of the electronic state described below that provides more information than the time and energy distributions alone [123].

A leviton source is also defined in a two dimensional electron gas, but does not use any confinement to isolate electrons. Instead it uses a pulsed injection technique that excites a discrete number of quasi-particles without an uncontrolled background of electron-hole pairs. creating 'minimal' electronic excitations [23] (see Section II D 4). The successful creation of levitons is demonstrated by measuring partition noise, which show a noise minima at the point where the average charge per pulse $Q = -e$ when the appropriate pulse shape and amplitude is used, see Eqs. (78) and (79). In contrast to the mesoscopic capacitor, the energy scale for the emission of Levitons is not set by the energy of a confined state (e.g. set by a gate pulse voltage [99]), but the temporal pulse width of the lorentzian pulse. In the ideal case of a single-leviton emission, a lorentzian input pulse $V(t) = \frac{h}{e\pi}\frac{\tau_0}{t^2+\tau_0^2}$ with $2\,\tau_0 \simeq 75$ ps, the energy dependence of the wavefunction of the resulting single-electron excitation has an exponential form $\psi(E) \propto \exp(-\tau_0\,E/\hbar)$, as measured from the Fermi edge [23], see Eq. (84) with $k = 1$ and $E = \hbar\omega$.

2. *Tomography of low energy electrons: the HOM protocol*

Techniques to probe the quantum state of the injected electrons can be performed for low energy sources by harnessing two-particle interference effects. One example is where the excitations from two independently operated single-particle sources are collided at a beam splitter and the output read out by detection of shot noise. Figure 18 shows the principle and execution of two-particle interference study of single electron wave packets. Two sources, with adjustable phase, and a beam-splitter are required, along with a system to detect shot noise. The suppression of the partitioning noise for synchronised arrival is a probe of the indistinguishability of the incoming wave packets [98].

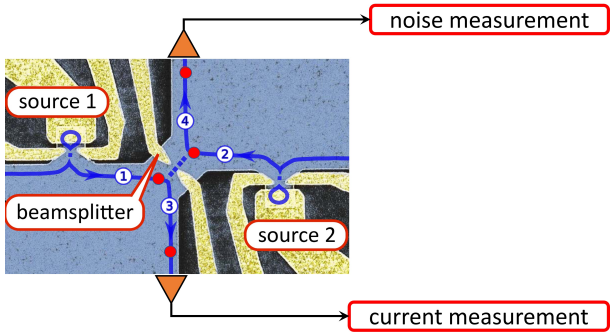

FIG. 18. SEM image of experimental device with two sources (on left and right arms) generating single-electron excitations in path 1 and 2 incident on the interaction region (beamsplitter). The outcome of the partitioning into outgoing paths 3 and 4 can be determined by measuring the electron correlation, realized in Ref. [98] by measuring the low frequency partitioning noise of the single-electron current in one output (4) and the (ac) charge current at the repetition frequency in the other output (3). The triangles symbolize the amplification chain for the electric charge currents.

This effect is a potent probe of the quantum state of the excitations, and how they are modified by interactions. For example, inter-channel coulomb interaction modify the Wigner distribution of excitations as they travel in coupled edge state, something that can be observed experimentally via the two particle interferometer [114, 126].

The above techniques have been further developed to provide a method of tomography of electronic excitations injected into one arm of the interferometer. Figure 19 shows a schematic representation of a two particle interference effect created at a beam splitter between the 'unknown' electrical excitation under test (left input arm) and a modulated Fermi sea (right input arm) whose frequency, amplitude and phase define the probe signal. As explained in Section II E 3, multiple measurements of the partition noise ΔS_n at different excitation frequency/phase can provide enough information for a quantum tomography of low energy electronic excitations [57, 123] as experimentally demonstrated in [51, 52].

The above schemes essentially hinge on creating a controlled interference experiment between excitations incident on opposite sides of partition barrier. Unfortunately, the techniques that work so effectively for low energy sources

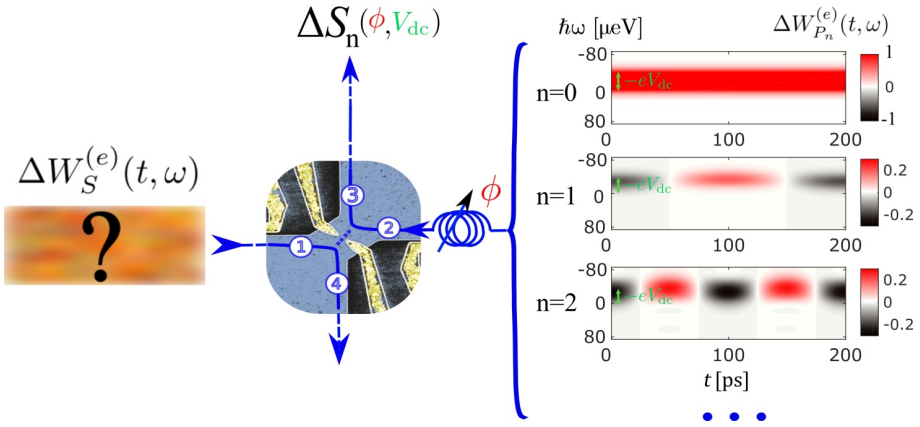

FIG. 19. Quantum current analyser for low energy excitations. Interference between the unknown periodic electronic Wigner distribution $W_S^{(e)}$ in the incoming channel (1) and a modulated reference Fermi sea signal, called the probe signal, $W_{P_n}^{(e)}$ incoming in channel (2), generated by a voltage $V_{P_n}(t)$ applied to a contact, occurs at a central barrier. The current shot noise signal is measured in output (3) as function of relative phase and reference probe amplitude. The measurement is repeated with a set of known reference probes at harmonics of the base frequency of the unknown signal. For each harmonic, one then varies the d.c. bias of the probe to sweep the position in ω thereby leading to a reconstruction of the ω-dependence of the n-th harmonic of the unknown excess Wigner distribution $\Delta W_S^{(e)}(t,\omega)$ [52]. Wigner distributions of the probe signal correspond to weak harmonic modulation discussed in Section II D 4 and Fig. 11.

are not universally applicable. In the next section we review the picture for high energy sources where a different technique is required.

3. *High energy quantum dot sources: Energy and time distributions*

High energy quantum dot sources load and eject electrons from a dynamically formed quantum dot controlled by an RF drive waveform with *eject* (rapidly increasing dot energy to eject electron), *reset* (rapidly lowering entrance barrier) and *load* (slowly raising entrance barrier to set charge capture) phases [127, 128]. Electrons within the 2DEG from the trap region underneath the metal surface gates are released into high energy edge states, confined to the edge of the mesa by perpendicular magnetic confinement. Basic operation of these devices can be validated using DC detection of the injected charge current which can be set to some integer $n = 1 \ldots N$ electrons per cycle [121, 128–130]. Measurement of a parameter-invariant quantised pump current indicates that a single electron is being transported in each cycle with high fidelity. The pumped DC current $I_p = \langle n \rangle ef$ at operation frequencies f =0.2-2 GHz and $\langle n \rangle$ can be 1 ± 10^{-7} in the most accurate devices [131, 132]. The current noise generated by partitioning a beam into with a probability T is given by $S = 2T(1-T)e^2 f$ and detection of this noise signal also demonstrates the ability of these devices to pump one electron per cycle [49, 133]. These tests alone do not probe the exact structure of the electronics excitations in the time/energy domain or provide information on the quantum state of the beam. Knowledge of the relevant time scales of the pump segments [127, 128] gives indirect information about the electron emission timing. For example, if the ejection pulse successfully ejects electrons with a probability of 1 when the ejection segment only occupies 10% of the $1/f \sim 1$ ns pumping period, then the characteristic tunnelling rate, Γ must be very fast on this time scale ($1/\Gamma \ll 100$ ps).

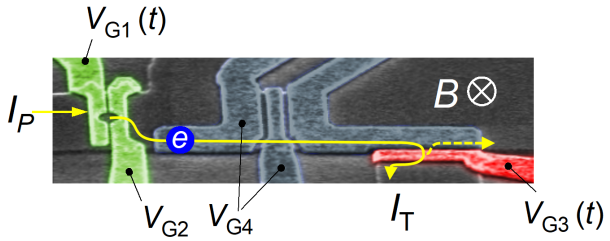

FIG. 20. SEM micrograph of a tunable barrier pump and detector barrier

To probe the characteristic emission time more directly it is necessary to introduce an additional time-dependent probe. For this purpose it is possible to use a time-dependent barrier in the beam path [30, 31] as shown in Figure 20. The energy selective barrier in the electron path (shaded red) is controlled by a periodic time dependent voltage V_{G3} synchronised to the same signal V_{G1} that drives electron emission from the pump (shaded green). This 'detector' barrier can be modulated rapidly, sweeping between voltages that open and close the channel to electrons at the threshold defined by the electron injection energy E. This injection energy is readily measured in a separate experiment with a time-independent barrier height set by the DC barrier voltage V_{G3}^{DC} and is typically $E \simeq 100 - 150$ meV with a broadening of $\simeq$ 1meV [30]. For a time dependent barrier height, injected electrons are either permitted through the barrier or deflected into a side channel depending on the relative arrival time of the electron and the point at which the barrier crosses the injection energy E. The ratio of transmitted to pumped current I_T/I_p as a function of the relative time delay t_d between pump and detector signals probes the arrival time distribution of electrons with picosecond resolution [31, 134] just as the detection of the transmitted current $I(V_{G3}^{DC})$ probes the energy distribution in the static barrier case. Through this technique it was possible to establish directly that the arrival time distribution of single electrons can be extremely small ($<$ 10 ps) and that the emission process only occupies a tiny fraction of the pump cycle. It also demonstrates that transport of electrons over the distances of order 2-10 microns between the pump and detector does not introduce a gross broadening of either the energy or arrival time distributions. In fact, the sharpness of these distributions is of immediate utility in characterising the modulated waveform which opens and closes the detector barrier [135]. This constitutes a novel use for single electron technology, for example the characterisation of RF components at cryogenic temperatures.

4. Towards quantum tomography of single hot electrons

Simple experiments using modulated barriers to sense the arrival time distribution [134] form a somewhat incomplete picture of the electronic Wigner distribution. As shown in Section II C 1), the Wigner distribution contains key information about the energy and time distributions and quantum coherence and thus captures much of the character of the source. For example, in a tuneable barrier electron pump there is a significant modulation of the source dot energy during emission [136]. This can lead to a strong emission energy, emission time correlation which is significant in both classical and quantum limits of electron emission [137]. To reveal this structure a full mapping of the emission distribution is desirable. Going further, information on the coherence or indistinguishability of the single electron excitations via tomographic reconstruction as applied to the low energy particle sources [51, 52] would help establish high energy sources as quantum building blocks in electron quantum optics circuits. There is, however, a serious problem with applying the same techniques to the higher energy injection; the lack of a Fermi sea at the high injection energies of these sources. This means that some other time-dependent probe of the injected excitations has to be used.

One approach is to use the temporal control of the detector barrier as a probe of the electronic Wigner distribution [32, 62]. This time dependent filtering method (see Section II E 2) provides information about the energy time correlations by probing 'intermediate' projections of the distribution between the purely energy projection of a 'static barrier' measurement $I_T(V_{G3})$ and the (ideally) time-only projection of the rapidly opening/closing barrier $I_T(t_{pd})$. This scenario as sketched schematically in Fig. 21(a). A linear ramp of the barrier voltage creates a time dependent mask of the arrival time distribution, with only those parts in the 'open' ($T = 1$) side of the line of this filter contributing to the transmitted current. When the linear ramp rate of the detector is kept constant, but the voltage and/or time delay of the signal generator is swept the current is cut off in a way that captures a particular projection of the distribution. Recording a large number of these distributions and performing a numerical back projection (for instance using the inverse radon transform) enables computation of the time, energy probability distribution, as shown in Fig. 21. The shape and size of this distribution contain key information about the emission process in these devices. For example, the numerical back projections capture a pronounced correlation between emission energy and time, with later arrival times corresponding to higher energy. This energy 'chirp', which is a characteristic feature of electronic emission in these devices, can be shaped by changing the sweep rate of the pump drive waveform very close to the moment of electron emission. This experimental signature helps to establish that it is indeed the emission processes that imprints the correlation and not some other process relating to the propagation path or the detector. It also enables a shaping of the distribution between maximal energy broadening (for fast emission) and maximal time broadening emission (for the slowest emission) which assists in the separation of contributions to the emission broadening. Ultimately, the size and shape of this emission distribution determines the resolution of the single electron sampling-oscilloscope technique demonstrated in Ref. [135], which is a prototypical demonstration of single electron sensing.

The area occupied by the measured distribution in energy-time place is a relevant measure of the quantum mechanical purity of the injected wave packets when compared to the quantum limit of one Planck constant. The quantum

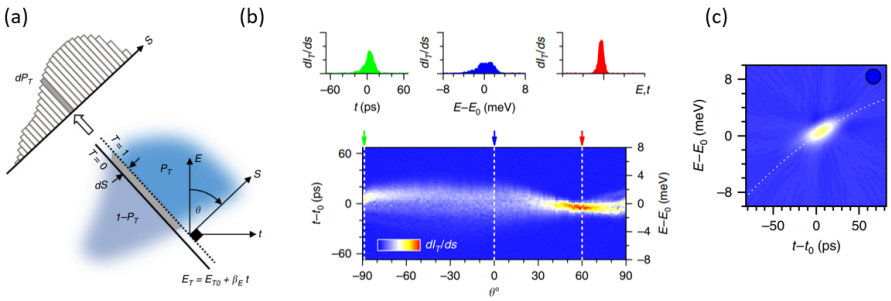

FIG. 21. (a) Schematic of a partially transmitted emission distribution in the presence of a linear ramp of an energy filtering barrier (b) Example of data collected at a continuously varying range of cut angles in the energy time plane (c) Example of the numerical back-projection of data to form a map of the emission distribution.

mechanical purity of the effective density matrix, $\gamma = h \int \int \rho^2(t, E)\, dt\, dE$, can be computed from the reconstructed distributions $\rho(t, E)$. Typical values of $\gamma \simeq 0.04$ indicate a distribution significantly broadened from that expected of quantum fluctuations alone. This suggests that some combination of experimental effects are broadening the detected emission distribution. One possible source is the effective energy resolution of the detector barrier, i.e. the energy range over which transmission changes from $T = 1$ to $T = 0$ [100]. The ability to change the shape of the emission distribution via changes of emission sweep rates allows some exploration of this factor. The smallest detected energy spread $\sigma_{E,\min} \simeq 0.8$ meV in the case of ejection from an almost stationary quantum dot energy. The detected emission energy range is clearly larger in the case of fast emission, as the source broadening dominates. This implies that $\sigma_{E,\min}$ is an upper limit of the barrier resolution. The finite sweep rate of the experimental probe barrier is also a possible limiting factor, setting an experimental time broadening which can be estimated from the maximal sweep rate and other relevant parameters as $\sigma_t' \simeq 0.3$ ps. Estimates of the combined resolution give $\sigma_{E,\min}\sigma_t' \simeq 0.36\hbar$, smaller than the resolution required to resolve electronic emission broadened only by quantum uncertainty.

Other possible sources of the low experimentally detected purity are classical fluctuations of the quantum dot source, both in energy and in time - the tomography above requires control of the nominal emission time of two sources set by phase delays between signal generators. As tomographic measurements are an average over multiple cycles, any instability in the relative emission time will reduce the detected purity. In addition, effects relating to exact trajectories or loss in the beam path can also contribute. Such additional effects will manifest differently in different forms of interferometry. The interference of single-particle amplitudes [27] are expected to be less affected by emission time jitter, whereas two particle interferometry (e.g. in the HOM geometry) requires precise control of the arrival time of individual electrons in the same cycle [98].

The use of current measurements and dynamic barrier to perform tomography is an intriguing alternative path to access coherence information [62]. This approach has many contrasts with other forms of tomography inspired by quantum optics (see Section II), for instance it relies upon an energy-filtering barrier which would be antagonistic to two-particle interference. The complete absence of the Fermi sea in the conducting waveguide and scattering region mean that the 'solitary' electrons are in a different regime of environmental interactions.

B. A counting scheme for single-electron wave packets

Lars Freise and Niels Ubbelohde

Coincidence counting and single photon detection are crucial tools for assessing first and second order coherences in correlation measurements (Fig. 22). The development of these techniques has been continuously advanced by applications in optical quantum information [138, 139]. By implementing networks of multiple detectors, multiplexing techniques or detectors with photon-number resolution, higher-order correlations have also become accessible [140]. In an electronic analogue to optical interferometry experiments, the characterization of single-electron and two-electron states as for example generated by tunable barrier electron pumps follows the same concepts for signal-acquisition. While an electron source typically emits a highly regular stream and therefore does not induce a chaotic limit to correlation due to accidental coincidence, higher-order moments may still provide valuable information in case of two-electron states and interactions. Similar to the performance-criteria in the single-photon case, a detection and counting scheme for electron quantum optics should achieve high detection-efficiency, large bandwidth and the ability to resolve particle numbers with high fidelity.

In an electron quantum optics circuit as shown in Figure 23, hot electrons injected in high magnetic field at non-

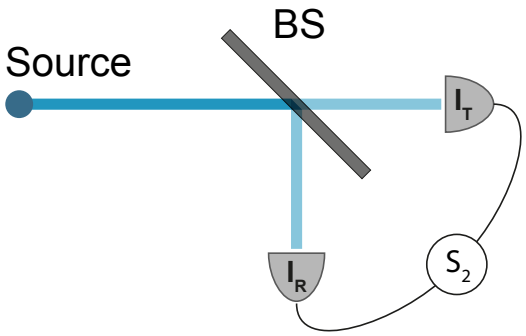

FIG. 22. Schematic of a classic Hanbury Brown and Twiss experiment, where a time-correlated signal of the partitioning can be acquired utilizing single-particle detection

equilibrium energies (several 10 meV above the Fermi level) propagate with minimal energy loss along the edge of the conductor (white lines exemplifying the path through the circuit). The detection of such quasi-ballistic electrons at the output of the circuit requires either storage [141] or on-the-fly[106, 142, 143] readout techniques. Trapping electrons prior to read-out allows to significantly enhance signal-to-noise at the expense of reduced bandwidth. Hot electrons can be trapped by controlled energy relaxation into a large charging node isolated from the remainder of the circuit. A minimal example of all essential circuit components is shown in Fig. 23. In the micrograph of a GaAs/AlGaAs heterostructure, the etched mesa (dark blue) forms the conductive region, separated by Au top-gates into three sections forming the pump(red), a short wave guide with an edge-depletion gate (orange) to modify transverse confinement potential for minimal losses [50, 135], and a trapping node (green). Shape and size of this node are designed to maximize the path length for the traversing electron while still allowing the charge to be read out with single electron resolution.

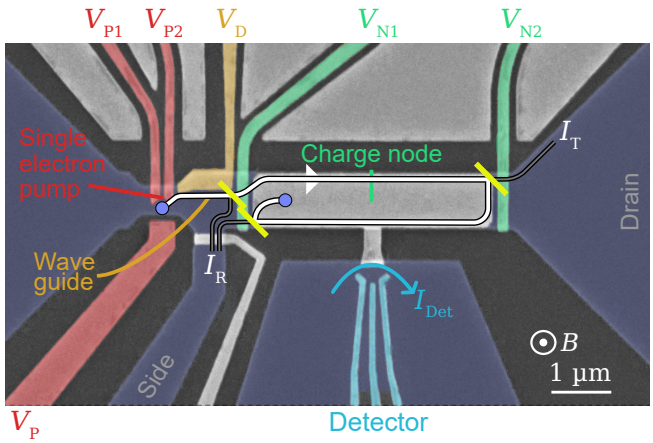

FIG. 23. False color SEM image of a sample implementing all components necessary to demonstrate the ballistic transport and trapping of high-energy electrons. Etched mesa conductive region (dark blue), gates forming the single-electron pump (red), edge depletion gate (orange), node confining gates (green) and detector dot gates (cyan) are colored. White lines indicate the path of an electron being trapped inside the node, gray lines sketch multiple paths of electrons ending up in one of the leads.

A measurement of the probability of an electron to traverse the node $\alpha = I_T/I_0$ as a function of the entrance (G_{N1}) and exit (G_{N2}) barrier height can be used to illustrate relaxation effects contributing to the effective detection fidelity (see Fig. 24). As the barrier heights are raised, the maximum energy to which the node can be filled is increased, effectively decreasing the excess energy of the injection electron relative to the node. This allows to probe the energy dependence of relaxation effects with a fixed injection energy $E_0 \gg E_F$ in a continuous-current measurement ($I_0 \approx 48\,\mathrm{pA}$).

The dashed line marks symmetric barrier height ($G_{N1} = G_{N2}$). Below this line, scattered electrons will flow off over the lower entrance barrier and do not contribute towards the displayed exit-barrier transmission (see Fig. 24b). Whereas the high injection energy isolates electron from e-e interaction within the wave-guide section of the circuit and transport along the gated edge suppresses relaxation via phonon emission (survival rate for this section of the path ≈ 0.998), these effects become visible within the trapping node. At large excess energies (labeled (D) in

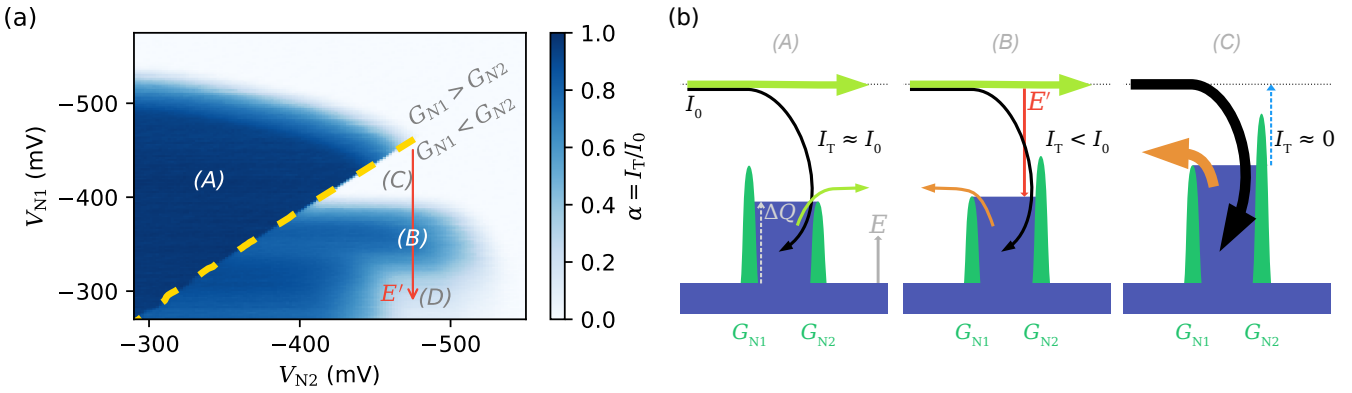

FIG. 24. (a) Continuous-current measurement of the transfer coefficient $\alpha = I_T/I_0$ as a function of the node entrance and exit barrier-height for constant injection energy. Barrier heights increase to the top/right of the diagram. (b) Energy diagrams showing the path of scattered and transmitted electrons for various points labeled in (a): Electron relaxation can only be probed if not both scattered and transmitted electrons are collected in I_T (A); for an excess energy smaller than 36 meV LO phonon emission (D) is suppressed (B); below a threshold energy all incoming electrons are being scattered and not transmitted (C).

Fig. 24a) LO phonon emission is easily recognizable as a step requiring the exit barrier to be at least 36 meV (the characteristic energy of LO-phonon emission in GaAs) below the injection energy for scattered electrons to still be transmitted. With decreasing excess energy (below the 36 meV threshold) LO-phonon emission becomes suppressed and over a large extent $\alpha \approx 0.6$ is observed, consistent to the fraction of electrons crossing G_{N2} without detectable energy loss when only G_{N2} is formed. For small excess energies e-e scattering dominates, displaying a power-law energy dependence [144] down to a threshold energy, below which all electrons scatter before reaching the exit barrier (C). In addition to these two effects commonly observed in such circuits, back action from the charge read-out will further increase the scattering rate within the node. To trap an electron injected on-demand, excess electrons on the node are flushed by temporally lowering the entrance barrier, and the exit barrier is set to reflect all incoming electrons, forcing unscattered electrons on a roundtrip with a length of 10 μm. A trapping fidelity near unity (0.999) under various experimental conditions can be achieved making the trapping node a very robust and versatile building block for electron quantum optics.

For charge readout, the trapping node is capacitively coupled to a separate quantum dot, which is tuned to a steep Coulomb blockade peak resonance, similar to conventional electron counting experiments and recently also used in a series circuit of single-electron sources [145] to demonstrate a benchmark for single-electron circuits [146]. As the on-demand source provides control over the injection time, a differential readout of the charge detector signal with high signal-to-noise ratio becomes possible, as the integration time of the detector signal before and after electron injection can be freely chosen. At a read-out bandwidth of 230 Hz, number of trapped electrons can still be estimated with a fidelity better than 5 sigma.

For applications in tomography and interferometry, the required energy and time selectivity can be achieved by applying a sharp transient signal to the entrance barrier [141]. Figure 25 shows an example measurement of coincidence correlations $P_{m,n}$ in a configuration very similar to Fig. 22, where the partitioning of a multi-electron state is acquired by placing two detection nodes (A and B) at the outputs of the beam splitter. Here, a total of 16 different non-zero elements of the coincidence correlations are resolved. This allows to simultaneously characterize the source, which potentially injects unwanted extra electrons, record losses and excitations and probe interactions, which is particularly important in a system, where strong Coulomb interactions are likely to influence partitioning at the beam splitter in addition to particle statistics. This distinctly exceeds the capabilities of current and noise measurements, highlighting the advantages of counting in complex circuits utilizing multi-electron states.

C. Dissipation in the quantum Hall effect regime in h-BN encapsulated graphene

François Couedo, Alexsander Kadykov and Wilfrid Poirier

The development of a single-electron interferometry platform based on graphene relies on high-quality devices operating in the QHE regime [147]. It is particularly interesting to determine not only the transport properties such as carrier mobility and contact resistance but also the dissipation mechanisms responsible for electron backscattering

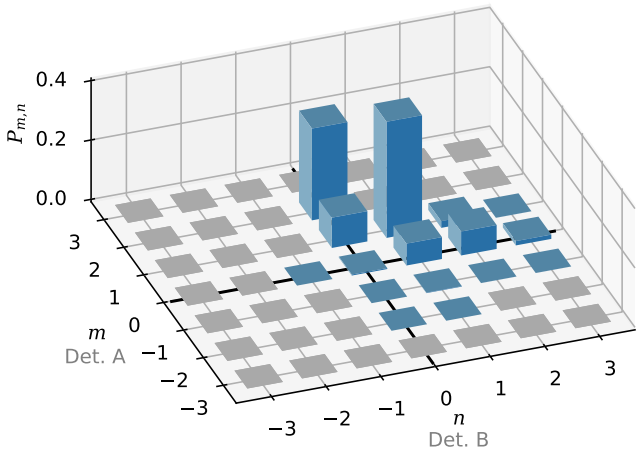

FIG. 25. Exemplary bar graph depicting the coincidence correlations of two detector circuits (A and B), shown for a series of single-shot counting measurements. A total of 49 probabilities $P_{m,n}$ can be resolved by the electron counter.

in the edge states, which is characterized by a finite longitudinal resistance value at finite temperature and current. These investigations are also essential to test the Hall quantization accuracy of graphene-based quantum resistance standards which relies on a low rate of charge carrier backscattering [148]. In this perspective, one question of interest is: can a higher carrier mobility, than that achieved in graphene grown on SiC (typically $10\,000\,\mathrm{cm^2V^{-1}s^{-1}}$), lead to a resistance standard operating in more relaxed experimental conditions [149], i.e. at lower magnetic field ($B < 3.5$ T), higher temperature ($T > 10$ K) or higher measurement current ($I > 500\,\mu$A)? Another goal of these characterizations was to know whether the sharp increase of the longitudinal voltage, which manifests the breakdown of the QHE beyond a threshold current value [150], could be used as a very sensitive current detector, possibly able to detect the injection of a single-electron like a Leviton quasi-particle [23].

1. Basic transport characterizations

To characterize the electronic transport properties, two devices with a Hall bar geometry (width of $4\,\mu$m) were fabricated at CEA[151] from heterostructures made of a graphene monolayer encapsulated between hexagonal-boron nitride (h-BN) flakes of a few tens of nanometers thickness (see Fig.26a)). A graphite back-gate is added to tune the carrier density and to screen charged impurities located in the SiO_2/Si substrate on which the stack is deposited. The stack is made using polypropylene carbonate (PPC) transfer of mechanically-exfoliated layers obtained from high-purity crystals. The device mesa is defined by CHF_3/O_2 reactive ion etching and Cr/Au contacts are realized at the stack edges.

The resistance of contacts is measured in the QHE regime ($\nu = 2$ plateau) using a three-terminal connection scheme to exploit the edge equipotentiality [152]. In the first Hall bar (S1), contact resistances of about 100 Ω are typically measured, which corresponds to a contact resistivity of about $350\,\Omega\,\mu$m. To further improve the quality of these contacts, which is known to be critical not only for achieving an accurate quantized Hall resistance but also for observing the fractional quantum Hall effect, a more complex design was tested for the second Hall bar (S2). The graphite gate surface was reduced so that the carrier density of an area close to the contacts could be independently tuned and increased by the Si back-gate. This allowed achieving lower contact resistivity around $250\,\Omega\,\mu$m. From magnetoresistance measurements performed at low magnetic fields, an unexpectedly low carrier mobility around $2000\,\mathrm{cm^2V^{-1}s^{-1}}$ was determined for carrier densities of a few $10^{11}\mathrm{cm^{-2}}$ in S1 device. This was explained by a pollution or water that got in between the layers during the stack manufacturing. On the other hand, carrier mobilities close to $100\,000\,\mathrm{cm^2V^{-1}s^{-1}}$ and $70\,000\,\mathrm{cm^2V^{-1}s^{-1}}$ at 4 K for holes and electrons respectively were measured in S2 device. These higher carrier mobilities allowed observation of the QHE below 1 T and lift of both spin and valley degeneracies of Landau levels at 18 T (see 26b)). Besides, typical features of the fractional $\pm 4/3$ state can be observed at $B = 19\,\mathrm{T}$ and $T = 0.3\,\mathrm{K}$.

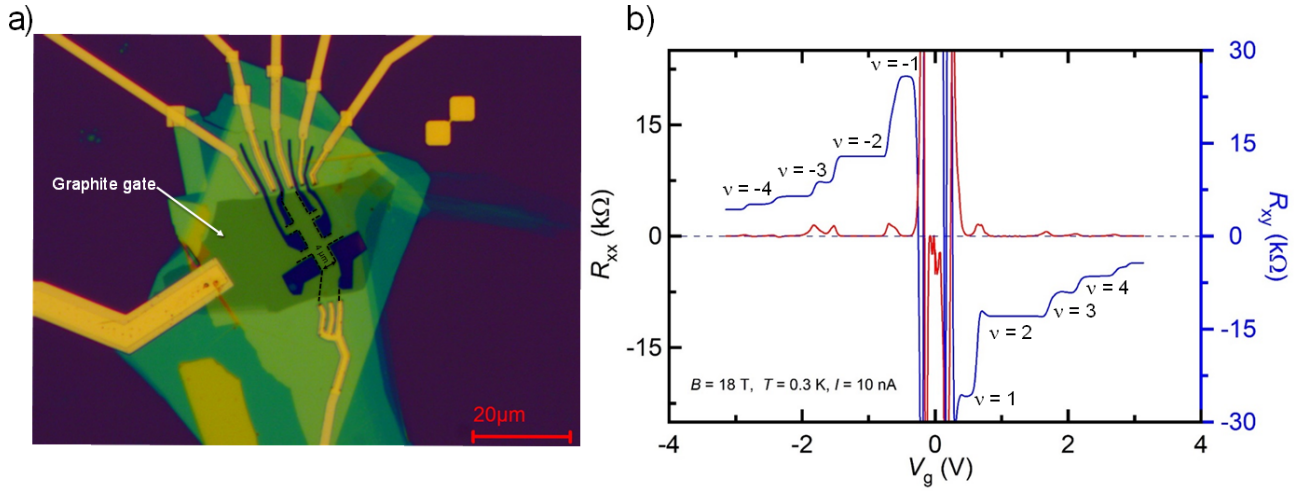

FIG. 26. a) Optical image of a h-BN encapsulated graphene Hall bar. b) Magnetoresistance curves measured at B=18 T.

2. *Dissipation mechanisms in the QHE regime*

The quantization of the Hall resistance in the QHE regime relies on the absence of backscattering: the two-dimensional gas must be in a dissipation-less state[153]. At finite temperature and measurement current, a residual level of dissipation exists and can be quantified by the measurement of the longitudinal resistance. The analysis of the current and temperature dependencies of the longitudinal conductivity allows the determination of the mechanisms of dissipation, i.e. of backscattering.

a. Temperature dependence It turns out that the temperature dependence of the conductivity can be explained by the backscattering mechanism based on the variable range hopping (VRH), both in the low carrier mobility S1 and the high carrier mobility device S2. The temperature data can be fitted by the law of the VRH based on a soft Coulomb gap, $\propto (\frac{1}{T})\exp[-(T_0/T)^{-1/2}]$, where $T_0 = C\frac{e^2}{4\pi\epsilon_0\epsilon_r\xi}$, ϵ_r is the relative dielectric constant, ξ is the localization length of bulk states and $C = 6.2$[154] is a numerical parameter related to percolation theory [155]. In device S1 the maximal value of T_0 amounts to about 1850 K at B=16 T. A similar value was found in a device [156] of the same carrier mobility but made of graphene grown by chemical vapor deposition of propane/hydrogen on SiC. Considering the different dielectric constants in both graphene materials, one finds a localization length about three times lower in the SiC-based device than in the h-BN encapsulated graphene device. This can be explained by the specific short range disorder caused by the buffer layer existing at the interface between graphene and SiC substrate[156, 157]. On the other hand, the adjustment of data in the high carrier mobility device leads to a larger T_0 value of about 40 000 K at B=10 T. This reflects a stronger temperature robustness of the dissipation-less state. For comparison, let us remember that the highest T_0 values were found around 10 000 K in devices made of graphene grown on SiC [149, 158]. As for these devices, the localization length deduced from such large T_0 value is found lower than the magnetic length $l_B = \sqrt{\hbar/eB}$, which is not expected from the VRH theory. This disagreement seems to occur in highly-robust dissipation-less state against temperature independently of the nature of the graphene material. Besides, considering T_0 values of both devices and those from previously characterized devices based on graphene grown on SiC, we experimentally observe an increase of T_0 as a function of the carrier mobility: the highest the mobility in the range investigated, the highest the temperature robustness of the dissipation-less state.

b. Current dependence In the VRH theory based on a soft Coulomb gap, the longitudinal conductivity follows a law $\propto \exp[-(I_0/I)^{-1/2}]$, where I_0 is a current parameter linked to T_0 according to the relationship $T_0 = I_0\frac{eR_H}{k_B}(\xi/W_{\rm eff})$, where k_B is the Boltzmann constant and $W_{\rm eff}$ is the effective width over which the Hall voltage drops (in an homogeneous device, $W_{\rm eff}$ is the sample width). The current effect can also be reduced to an effective temperature $T_{\rm eff} = I\frac{eR_H}{k_B}(\xi/W_{\rm eff})$ [159]. This implies that curves of conductivity obtained as a function of either temperature or current can be superposed by converting current in an effective temperature using the former linear relationship. This was already verified in graphene grown on SiC by chemical vapor deposition of propane/hydrogen [156].

In the h-BN encapsulated graphene devices, current curves cannot be superposed to temperature curves using an effective temperature proportional to the current. On the other hand, superposition can be achieved using a modified relationship by introducing an effective width decreasing linearly with an increasing current, $W_{\rm eff} = W_{I=0}(1-\alpha\times|I|)$, where $W_{I=0}$ is the effective width at zero current. $W_{I=0}$ is found close to the sample width in S1 device at B= 16

T (about 5 µm) and at a lower value (less than 1 µm) in S2 at B= 10 T. This tends to indicate that the Hall electric field is more homogeneous in S1 than in S2. The current effect was also investigated by measuring the longitudinal resistance as a function of I for both current directions and for various graphite gate voltages. A breakdown current I_c (values up to 15 μA are found for B=10 T and T=10 K in S2) is defined by a given longitudinal resistance threshold ($R_{xx} > 0.1$ Ω). Similar breakdown current densities around 4 A/m are found in S1 and S2 devices. The advantage of a larger T_0 temperature in S2 seems to be compensated by a lower $W_{I=0}$ width. Surprisingly, for both devices an inverse evolution of I_c is observed as a function of the gate voltage depending on the breakdown current polarity. All these features can be explained by the relative effect of the Hall voltage to the graphite gate voltage. Given the small distance (around 30 nm) of the graphite gate from the graphene layer, the applied gate voltages are indeed small and comparable to the Hall voltages that develop for the significant currents of a few μA used for metrology measurements. This implies that the current circulation induces a differential gate effect on each edge of the Hall bar: V_g on one edge and $V_g \pm R_H \times I$ on the other edge. This leads to a transverse carrier density gradient which turns into a transverse Landau level filling factor gradient in the QHE regime. Experimentally, this manifests not only by a linear reduction of the effective width, W_{eff}, of the integer (ν=2) quantized current strip as a function of the current value but also by an effective gate shift proportional to the current which can explain the observed I_c evolutions as a function of the gate voltage. It turns out that the usual triangular shape[160] of the breakdown current evolution as function of the LL filling factor (or gate voltage) in a quantized plateau can be recovered by rescaling the gate voltage according to the relationship $V_{g,eff} = V_g \pm \mathrm{sign}(I_c)\beta R_H \times I_c$, where β is a proportionality factor lower than unity. To conclude, the electronic transport properties can be strongly impacted in devices equipped with a close gate by the current-induced gate shift effect.

3. Hall quantization accuracy

Precision measurements of the longitudinal resistance per square R_{xx} were performed on the $\nu = 2$ plateau using a low-noise direct-current amplifier or a cryogenic current comparator (CCC)[161]. Values lower than 100 $\mu\Omega$ were measured at B=16 T, T=0.3 K and $I = 5$ μA in S1 and at B=10 T, T=10 K and $I = 5$ μA in S2. This threshold value corresponds to the value below which the Hall resistance is expected to be accurately quantized within a few 10^{-9} uncertainty in usual QHR devices, according to the metrological guidelines[162]. Let us remark that these resistance values are obtained by subtracting longitudinal voltages measured for positive and negative currents. This procedure allows cancelling parasitic voltage signals that we usually observe in graphene devices. Accurate measurements of the Hall resistance performed using a CCC-based resistance bridge however show significant relative discrepancies to the quantized value $R_K/2$ amounting to a few 10^{-7} for both Hall bars. They are randomly distributed as a function of gate voltage, temperature or current. A first explanation relies on the finite value of the resistance of edge contacts, which amount to around percent of R_H. In the Landauer-Büttiker theory, quantization errors are indeed predicted if there is selective detection of non-equilibrium populations of edge states, which happens for imperfect adjacent current and voltage contacts[163]. In metrology works, the discrepancies reported were found qualitatively increasing with the contact resistance[160] However, their magnitude could not be predicted by the theory because they depend on the experimental equilibrium rate of edge states[164]. Here, the impact of the resistance of contact could be reinforced by the mesoscopic size of the devices. The current-induced gate shift could also be responsible for part of the Hall resistance discrepancies. Independent accurate measurements of the Hall resistance as a function of the gate voltage, performed either with a positive and a negative current in the high carrier mobility device, lead to two shifted resistance plateaus. For a current of 5 μA, it does not exist any gate voltage ensuring quantization of the Hall resistance both for positive and negative currents. The close gate has therefore a clear detrimental effect on the measurement of the Hall resistance at large currents that can explain the discrepancies observed.

4. Current sensitivity in the QHE breakdown regime

The principle of the current detection consists in using the strong non-linear increase of the longitudinal resistance at the QHE breakdown to detect a small current variation. In practice, the Hall bar is fed with a dc current used to set the dissipation state and a small ac current at a frequency of a few hundred Hz is injected through another terminal. The resulting increase of the ac longitudinal voltage is then detected. The ratio of the ac voltage to the ac current gives a dynamic resistance. In the devices investigated, it is observed that the dynamic resistance increases with the dc current but remains limited to a few thousands of ohms. This small dynamic resistance is explained by the dissipation mechanism which is dominated by the VRH: no enough sharp increase of resistance, i.e. of dissipation, is observed at the QHE breakdown. In future works, one could study the QHE breakdown in devices designed with a width constriction to amplify the transverse Hall electric field so that the inter Landau level scattering mechanism

could drive a sharper QHE breakdown[165–167]. Besides, it is observed an increase of the $1/f$ voltage noise power with an increasing dc current. This noise increase can spoil the sensitivity gain of the ac current brought by the dynamic resistance increase. Thus, small current detection requires measurement at frequencies large enough so that $1/f$ noise level is lower than the one of the voltage detector.

IV. IMPLEMENTATION OF INTERFEROMETRIC SENSING

The following section discusses two specific implementations of interferometric sensing developed in the spirit of harnessing electron quantum optics for novel sensing applications. First, in section IV A there is an explanation of how a form of interferometer well known in classical optics, the Fabry-Perot cavity, can be realised in an electronic system. This can be used to measure time dependent potentials when driven with on-demand single electron sources. Secondly, section IV B showcases an experiment which uses a Mach-Zehnder interferometer to sense the emission of magnons, charge neutral spin waves, in a quantum hall ferromagnet. These examples nicely illustrate the power of single electron interferometry, both for high bandwidth sensing of electromagnetic fields, but also an emerging capability as a sensor in spintronic systems.

A. Single-electron interferences in Fabry-Perot cavities

Gwendal Fève and Hugo Bartolomei

We describe in this section how the electronic coherence of short single electron pulses generated at the input of an interferometer can be exploited to probe time-dependent electric fields.

1. Principle of the experiment

The principle of electric field sensing by single electron interferometry is sketched in Figure 27.a). A first beam-splitter splits electronic trajectories in two different paths that are recombined by a second beam-splitter. Inserting a time-dependent electric field on one arm of the interferometer leads to a temporal modulation of the phase difference between the two arms. Depending on this phase difference, electrons will exit the interferometer in output 3 or 4, which can be detected by either measuring the average electrical current or by detecting individual electrons using a single electron detector [1]. The time sampling of the electric field inside the interferometer can be performed by generating single electron pulses of short temporal width at the input of the interferometer and recording the output interference pattern as a function of the time delay between single electron emission and the time-dependent electric field.

Electronic interferometers such as Mach-Zenhder interferometers [27, 168] can be defined using electrostatic gates that are used as tunable electronic beam-splitters. In the presence of a strong magnetic field perpendicular to the sample (integer quantum Hall regime), the electronic propagation can also be guided along the edges of the sample, defining two distinct paths inside the interferometer with well-defined lengths. Figure 27.b presents the design of an electronic Fabry-Perot interferometer in the integer quantum Hall regime. Two split gates called quantum point contacts (QPCA and QPCB) act as tuneable beam-splitters scattering electronic waves with transmission amplitude $t_{A/B}$ and reflection amplitude $ir_{A/B}$, where $t_{A/B}$ and $r_{A/B}$ are real coefficients. For $r_A, r_B \neq 0$, electrons can perform several round-trips within the cavity of the Fabry-Perot interferometer, accumulating some phase φ related to the Aharonov-Bohm phase inside the cavity. This phase can be modulated by the voltage applied on the gate of the bottom part of the cavity (see Fig. 27.b). The time dependent electric field leads to a dynamical change of the area of the interferometer leading to a dynamical change of the Aharonov-Bohm phase. The goal of the SEQUOIA project is to demonstrate sensing of electric and magnetic fields using single electron wave packets with a time resolution below 1 ns and a space resolution of the order of 1 micron. The time resolution is limited by the width of electronic wave packet whereas the spatial resolution is set by the size of the gate that is used generate the electric field.

2. Simple model of time-dependent electronic scattering

We describe here how a simple model of single electron scattering by a time-dependent scatterer can describe single electron interference when the phase difference between two arms depends in time. The current $I_{\rm out}$ measured at output 4 of the interferometer can be expressed as a function of electronic coherence (see Eq. (54)):

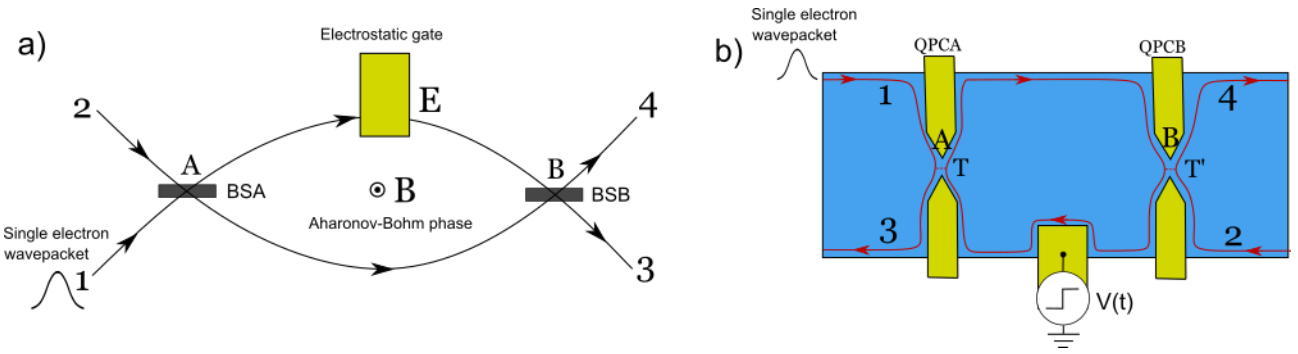

FIG. 27. a) Principle of the experiment. Two beam-splitter define two paths for electron propagation. The electrical current at a given output of the interferometer probes the phase difference between the two paths which can be dynamically varied when a time-dependent electric field is generated at one arm of the splitter. using a single electron source of short temporal width, the time dependent electric field can be sampled by measuring the output electrical current for different times of emission of electrons inside the cavity. b) Implementation of the previously discussed sketch in a Fabry-Perot cavity defined in a two-dimensional electron gas in the integer quantum Hall regime. Electronic propagation occurs along the ballistic chiral edge channels (represented in red). Metallic split gates can be used as quantum point contacts used as electronic beam-splitters of tunable transmission amplitude t_A and t_B. Applying the time dependent voltage $V(t)$ on a plunger gate can generate a time-dependent phase difference between the two interfering paths.

$$I_{\rm out}(t) = -ev_F \Delta\mathcal{G}^{(e)}_{\rm out}(t,t) = -ev_F \int_{\mathbb{R}^2} S^*(t,t_1) S(t,t_2) \Delta\mathcal{G}^{(e)}_{\rm in}(t_1,t_2)\, {\rm d}t_1 {\rm d}t_2 \tag{102}$$

in which $S(t,t')$ describes the propagation of an electronic excitation from the input of the interferometer at time t' to its output at time t. For the Fabry-Perot interferometer, it can be decomposed as a sum of paths involving an increasing number of round-trips inside the cavity:

$$S(t,t_2) \approx -t_A t_B \delta(t-t_2-\tau_1) - t_A t_B r_A r_B\, e^{i\frac{e}{\hbar}\int_{t-\tau_0}^{t-\tau_0+\tau_g} V(\tau)d\tau} \delta(t-t_2-\tau_1-\tau_0) + \cdots, \tag{103}$$

where τ_1 is the time to go from point A to point B inside the cavity, τ_0 is the time to make one round-trip inside the cavity (from B back to B), and τ_g is the travel time below the gate. We assume in Eq. 103 that the expansion of $S(t,t')$ as a function of the number of loops inside the cavity can be stopped at first order (one loop). This is a reasonable hypothesis when one beam splitter is set to a small value of the reflection probability (r_A, $r_B \ll 1$) or whenever electronic phase coherence is lost after one round trip inside the cavity. The time-dependent modulation of the phase is related to the integration of the local electrical potential $V(t)$ below the gate.

Finally, the computation of the output average current requires to know the value of the input coherence of the Fermion field, $\Delta\mathcal{G}^{(e)}_{\rm in}(t,t')$. Expressing the input coherence in terms of electron and hole excitations is a complex task in general [29, 169]. However, in the specific situation where a single electronic excitation is generated at the input of the interferometer, $\Delta\mathcal{G}^{(e)}_{\rm in}(t,t')$ can be simply related to the emitted electronic wavefunction: $\Delta\mathcal{G}^{(e)}_{\rm in}(t,t') = \varphi^*(t)\varphi(t')$. Plugging these expressions of $S(t,t')$ and $\Delta\mathcal{G}^{(e)}_{\rm in}$ in the expression of $I_{\rm out}(t)$, and introducing the transmission and reflexion probabilities $T_{A/B} = |t_{A/B}|^2$ and $R_{A/B} = |r_{A/B}|^2$ of the two beam splitters, we obtain:

$$\frac{I_{\rm out}(t)}{-ev_F T_A T_B} = |\varphi(t-\tau_1)|^2 + R_A R_B |\varphi(t-\tau_1-\tau_0)|^2 + 2\sqrt{R_A R_B}\Re\left[e^{i\frac{e}{\hbar}\int_{t-\tau_0}^{t-\tau_0+\tau_g} V(\tau){\rm d}\tau} \varphi^*(t-\tau_1)\varphi(t-\tau_1-\tau_0)\right]. \tag{104}$$

The quantity of interest is the dc current at the output of the cavity, which is obtained after time average of $I_{\rm out}(t)$:

$$I_{\rm out,\,dc} = -ef\, T_A T_B \left[1 + R_A R_B + 2\sqrt{R_A R_B}\,\Re\left(\int_{\rm R} e^{i\phi(t)}\varphi^*(t-\tau_1)\varphi(t-\tau_1-\tau_0)\,{\rm d}t\right)\right], . \tag{105}$$

where f is the frequency at which single electron wave packets are generated inside the Fabry-Perot cavity. The first two terms in Eq. (105) are the classical transmission probability for the direct path from A to B and after one round trip inside the cavity. The third term in Eq. (105) is the interference term that is sensitive to the time dependent phase $\phi(t)$:

$$\phi(t) = \frac{e}{\hbar}\int_{t-\tau_0}^{t-\tau_0+\tau_g} V(\tau){\rm d}\tau \tag{106}$$

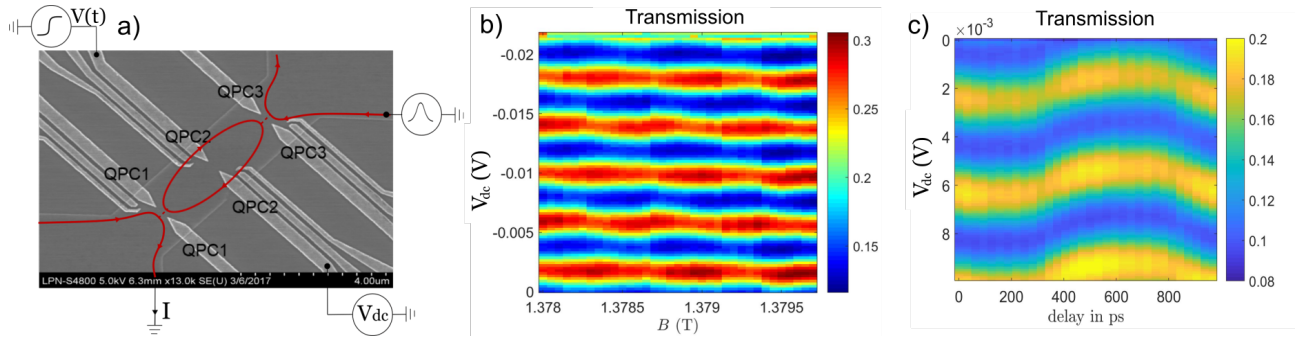

FIG. 28. a) Scanning electron microscope picture of the sample. Two quantum point contacts, QPC1 and QPC3 are used as tunable beam-splitters. QPC2 at the center of the sample is used as a plunger gate voltage for changing the phase in a static way (using $V_{\rm dc}$) and in a dynamical way (using $V(t)$). b) Two-dimensional color plot of the transmission through the cavity as a function of $V_{\rm dc}$ and magnetic field B. c) Two-dimensional color plot of the transmission through the cavity as a function of $V_{\rm dc}$ and time delay between single electron emission and the periodic square voltage $V(t)$.

A classical limit of Eq. (105) can be obtained in the limit of slow voltage variation, much slower than both τ_g, τ_0. In this limit, the phase $\phi(t)$ can be approximated by $e\tau_g V(t)/\hbar$. Considering narrow wave packets with a much shorter duration than the temporal scale for the variations of $\phi(t)$ enables it to feel only the phase $\phi(t)$ for $t = t_e$, where t_e denotes to the entering time into the Fabry-Perot cavity. In this regime of very short wave packets and slow variation of the plunger gate voltage, Eq. (105) simplifies into:

$$I_{\rm out,\ dc} = -ef\,T_A T_B\left[1 + R_A R_B + 2\sqrt{R_A R_B}\cos\left[\phi(t_e)\right]\right]. \tag{107}$$

Eq. (107) shows a direct relation between the output current and the time-dependent phase, allowing to sample the time-dependent phase by modifying the electron emission time t_e. Although the phase is directly proportional to the time dependent voltage, the relation between $I_{\rm out,\ dc}$ and the local voltage potential $V(t)$ is non-linear due to the cosine dependence on $\phi(t_e)$. A linear relation can be obtained by tuning the operation of the interferometer at the value of the phase $\phi = \pi/2$, which turns the cosine into a sine, and taking the small voltage limit:

$$I_{\rm out,\ dc} \approx -ef\,T_A T_B\left[1 + R_A R_B + 2\sqrt{R_A R_B}\,\frac{e\tau_g}{\hbar}V(t_e)\right] \tag{108}$$

At this operating point and within this regime, the interferometer can then be used as a voltage sampler whose time resolution is limited by the width of the single electron wave packets.

3. Description of the results

The sample is represented on Figure 28.a. It consists in a Fabry-Perot cavity, as sketched on Fig. 27.b, implemented in a two-dimensional electron gas of density $n_s = 1.1 \times 10^{15}\,\mathrm{m}^{-2}$ and mobility $\mu = 1.4 \times 10^6\,\mathrm{cm}^2\mathrm{V}^{-1}\mathrm{s}^{-1}$. A magnetic field $B = 1.37\,\mathrm{T}$ is applied perpendicular to the sample in order to reach the integer quantum Hall effect at filling factor $\nu = 3$ where the current is carried by three edge channels. Two quantum point contact labeled QPC1 and QPC3 are tuned to partially transmit the outer edge channel with transmissions T_A and T_B and fully reflect the two inner channels. QPC2 at the center of the sample is used as a plunger, both for tuning the static value of the phase using a dc gate voltage $V_{\rm dc}$ connected to the split gate at the bottom, and for applying the time dependent potential $V(t)$ at the top split gate.

Single electron emission is triggered by applying a periodic train of Lorentzian voltage pulses with a period of 1 ns and a width of 35 ps. The amplitude of the pulses is calibrated such that each pulse contains one electron. It has been demonstrated that in this regime and at very low temperature, a single electronic excitation is generated with a wavefunction $\varphi(t)$ of Lorentzian shape [23]. The periodic train of Lorentzian pulses is periodically modulated at the low frequency of 1 MHz in order to detect the output dc current transmitted through the cavity using lock-in detection.

Figure 28.b) presents the measurement of the transmission through the cavity as a function of the dc gate voltage $V_{\rm dc}$ applied to the plunger and magnetic field B. As can be seen on the Figure, single electron interferences can be seen as oscillations of the transmission as a function of $V_{\rm dc}$. The amplitude of the oscillations is 0.18 and the contrast of interference is approximately 0.4. The interference pattern seems almost not modified when the magnetic field is

varied, as expected when charging effects of the bulk of the interferometer cannot be neglected and lead to a shrinking of the interferometer area when the magnetic field is increased [170]. However, oscillations of the transmission as a function of magnetic field can be observed with an amplitude reduced by a factor 7 and a period of 0.6 mT which is perfectly consistent with a variation of the magnetic flux through the cavity of one flux quantum.

Having characterized single electron interferences through the Fabry-Perot cavity, we can move to the dynamical variation of the phase by applying a periodic square voltage $V(t)$ at a frequency of 1 GHz on the top split gate of QPC2. Figure 28.c) presents the measurement of the transmission through the cavity as a function of the dc voltage $V(\mathrm{dc})$ (vertical axis) and the time delay (horizontal axis) between single electron emission and the periodic square voltage applied to the top split gate. Taking a vertical cut of the color plot shows the oscillation of the transmission as a function of the static phase difference for a given time delay. Around a time delay of 300 ps, we observe a sudden shift of the interference pattern (with a phase shift which equals $\pi/2$). This reflects the fact that single electrons are now sensing a different value of the electric field (or electrical potential) corresponding to a modified value of the phase difference between the two paths inside the interferometer. The interference pattern then stays roughly constant until, for a time delay of 800 ps, the interference pattern shifts again as the square voltage goes back to its initial value. This plot shows that single electron pulses combined with single electron interferometry can be combined to detect time-dependent electrical potentials with a resolution of tens of picoseconds limited by the width of single electron wave packets.

B. Excitonic nature of magnons in a quantum Hall ferromagnet

Preden Roulleau and François Parmentier

When a perpendicular magnetic field is applied to a two-dimensional electron system like e.g. graphene, electrons become distributed in energy on widely-spaced, highly degenerate Landau levels. The latter are the hallmark of the so-called quantum Hall effect regime. At large enough magnetic field, the various symmetries underlying the Landau levels (spin, valley, etc) can break, giving rise to well-separated sub-Landau levels that can be fully polarized in a given symmetry. By tuning the electron density and the magnetic field such that only one spin-polarized sub-Landau level is filled, one can effectively create a perfect ferromagnet, a system where absolutely all electron spins point in the same direction. In monolayer graphene, such a perfect "quantum Hall ferromagnet" is obtained at filling factor $\nu = 1$, when spin and valley symmetries are broken by electronic interactions and only a single spin- and valley-polarized electron channel can propagate along the edges of the sample (while the bulk remains insulating). Recent experiments have shown that it is possible to excite the elementary bulk excitations of this peculiar ferromagnet, which are charge-neutral spin waves, or magnons, simply by applying to the sample a drain-source potential larger than the Zeeman energy. Many fundamental properties of these magnons remain to be observed and investigated. In particular, even though they are magnetic excitations, magnons of a quantum Hall ferromagnet have an intrinsic excitonic nature, as they carry an intrinsic electric dipole oriented perpendicularly to their propagation direction.

To observe this electric dipole, we have devised an experiment [151], described in Figure 29a, in which a stream of magnons is emitted towards an electronic Mach-Zehnder interferometer realized in a graphene p-n junction, acting as an ultra-sensitive electric dipole detector. The detection mechanism is two-fold: on the one hand, the stream of magnons impinge on the interferometer with a given average angle, which depends on the position of the magnon emission point relative to the interferometer. Depending on the value of this angle, the positive part of the electric dipole might be closer to the interferometer than the negative part, or vice-versa (see insets in Figure 29a). This plays the role of an effective local electrostatic gate, shifting the position of the interferometer's two arms (central blue and yellow arrows in Figure 29a) relative to one another, thus leading to a measurable phase shift of the interferometer. On the other hand, the magnons are emitted randomly in time, and impinge accordingly on the interferometer. This leads to rapid fluctuations in the electric field felt by the interferometer, which cause the amplitude of the interference pattern to diminish.

We have confirmed this dual effect in the experiments (see Figure 29b), demonstrating the first observation of the excitonic nature of magnons in a quantum Hall ferromagnet. Furthermore, the analysis of the results unveils several elusive properties of the magnons; amongst them, the facts that the emission process is Poissonian (that is, magnons are indeed emitted randomly in time), and that increasing the drain-source potential increases the magnons' emission rate rather than their energy.

The ability to couple magnetic excitations to quantum coherent conductors offers many exciting possibilities for experiments probing new phenomena at the intersection of mesoscopic quantum physics and spintronics.

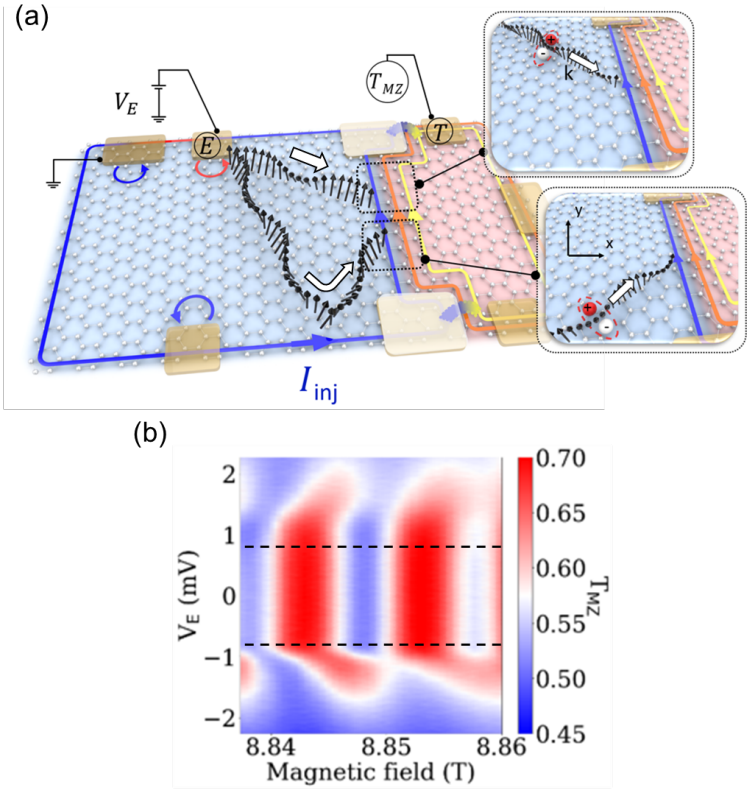

FIG. 29. (a) Artist sketch of the experiment: a flake of graphene is divided into two regions with opposite p- and n- doping (blue and red areas), creating at their interface an electronic Mach-Zehnder between the edge channels of each region with same spin (blue and yellow arrows). An additional channel with opposite spin (red arrow) also propagates in the right region but does not play any role here. Magnons (wavy black arrows) are emitted from a biased contact (E) towards the interferometer. Depending on the propagation direction relative to the interface (symbolized by the large white arrows), the magnons' electric dipoles (red and white balls) can have different orientations when impinging on the interface, as depicted in the insets. (b) Electronic transmission TMZ across the interferometer, measured versus bias voltage V_E and magnetic field. Above the bias voltage threshold (black dashed lines), magnons are emitted and the interference patterns become tilted and significantly blurred, indicating phase shift and decoherence.

ACKNOWLEDGEMENT AND DISCLAIMER

This work was supported by the Joint Research Projects SEQUOIA (17FUN04). This project received funding from the European Metrology Programme for Innovation and Research (EMPIR) cofinanced by the Participating States and from the European Unions Horizon 2020 research and innovation programme. G.F. and H. B. acknowledge the support of A. Cavanna, U. Gennser and Y. Jin for the fabrication of samples. P.R. thanks Patrice Roche.

Disclaimer: The views expressed in this Guide are those of the authors and of the EMPIR 17FUN04 project team.

Appendix A: Definitions and normalizations

Let us introduce the single-particle states $|t\rangle$ and $|\omega\rangle$, normalized as

$$\langle t|t'\rangle = v_F^{-1}\delta(t-t') \tag{A1a}$$
$$\langle \omega|\omega'\rangle = \delta(\omega-\omega') \tag{A1b}$$

which are related by

$$|t\rangle = \frac{1}{\sqrt{2\pi v_F}}\int \mathrm{d}\omega\, \mathrm{e}^{\mathrm{i}\omega t}|\omega\rangle \tag{A2a}$$
$$|\omega\rangle = \sqrt{\frac{v_F}{2\pi}}\int \mathrm{d}t\, \mathrm{e}^{-\mathrm{i}\omega t}|t\rangle \tag{A2b}$$

There relations mirror into the following relations for the fermionic field operator

$$\psi(t) = \int_{\mathbb{R}} c(\omega)\, \mathrm{e}^{-\mathrm{i}\omega t}\frac{\mathrm{d}\omega}{\sqrt{2\pi v_F}} \tag{A3}$$

in which the fermionic annihilation and creation operators $c(\omega)$ and $c^\dagger(\omega)$ obeying the canonical anti-commutation relations $\{c(\omega), c^\dagger(\omega')\} = \delta(\omega-\omega')$.

The single electron electronic Wigner distribution function can then be expressed as:

$$W^{(e)}_{\rho,x}(t,\omega) = \int_{\mathbb{R}} v_F \Big\langle \psi^\dagger\left(t-\frac{\tau}{2}\right)\psi\left(t+\frac{\tau}{2}\right)\Big\rangle_\rho e^{i\omega\tau}\,\mathrm{d}\tau \tag{A4a}$$

$$= \int_{\mathbb{R}} \Big\langle c^\dagger\left(\omega-\frac{\Omega}{2}\right) c\left(\omega+\frac{\Omega}{2}\right)\Big\rangle_\rho e^{-i\Omega t}\,\frac{\mathrm{d}\Omega}{2\pi} \tag{A4b}$$

Let us consider time-dependent single particle scattering and recall the connexion between single particle scattering and the linear relation between incoming and outgoing fermionic fields. We will discuss it in the $|\omega\rangle$ basis but the discussion can be adapted to any single particle state basis. The frequency representation of the single particle scattering matrix is defined by Eq. (55):

$$c_{\mathrm{out}}(\omega) = \int_{\mathbb{R}} S(\omega,\omega')\, c_{\mathrm{in}}(\omega')\,\mathrm{d}\omega' \tag{A5}$$

which translates into

$$c^\dagger_{\mathrm{out}}(\omega) = \int_{\mathbb{R}} S(\omega,\omega')^*\, c^\dagger_{\mathrm{in}}(\omega')\,\mathrm{d}\omega' \tag{A6}$$

Since $|\omega\rangle$ is obtained by the action of $c^\dagger(\omega)$ on the true particle vacuum $|\emptyset\rangle$, we thus obtain that

$${}_{\mathrm{out}}\langle\omega|\omega'\rangle_{\mathrm{in}} = {}_{\mathrm{in}}\langle\omega'|\omega\rangle^*_{\mathrm{out}} = S(\omega,\omega') \tag{A7}$$

Consequently, since relating $|\omega'\rangle_{\mathrm{in}}$ to $|\omega\rangle_{\mathrm{out}}$ precisely involves the single particle scattering matrix $S_{1\mathrm{p}}$, we find

$${}_{\mathrm{out}}\langle\omega|\, S_{1\mathrm{p}}\, |\omega'\rangle_{\mathrm{in}} = S(\omega,\omega') \tag{A8}$$

[1] A. J. Heinrich, W. D. Oliver, L. M. K. Vandersypen, A. Ardavan, R. Sessoli, D. Loss, A. B. Jayich, J. Fernandez-Rossier, A. Laucht, and A. Morello, Quantum-coherent nanoscience, Nature Nanotechnology **16**, 1318 (2021).

[2] A. Laucht, F. Hohls, N. Ubbelohde, M. F. Gonzalez-Zalba, D. J. Reilly, S. Stobbe, T. Schröder, P. Scarlino, J. V. Koski, A. Dzurak, C.-H. Yang, J. Yoneda, F. Kuemmeth, H. Bluhm, J. Pla, C. Hill, J. Salfi, A. Oiwa, J. T. Muhonen, E. Verhagen, M. D. LaHaye, H. H. Kim, A. W. Tsen, D. Culcer, A. Geresdi, J. A. Mol, V. Mohan, P. K. Jain, and J. Baugh, Roadmap on quantum nanotechnologies, Nanotechnology **32**, 162003 (2021), 2101.07882.

[3] S. Hermelin, S. Takada, M. Yamamoto, S. Tarucha, A. Wieck, L. Saminadayar, C. Bäuerle, and T. Meunier, Electrons surfing on a sound wave as a platform for quantum optics with flying electrons, Nature **477**, 435 (2011).

[4] M. R. Delbecq, T. Nakajima, T. Otsuka, S. Amaha, J. D. Watson, M. J. Manfra, and S. Tarucha, Full control of quadruple quantum dot circuit charge states in the single electron regime, Applied Physics Letters **104**, 183111 (2014).

[5] A. R. Mills, D. M. Zajac, M. J. Gullans, F. J. Schupp, T. M. Hazard, and J. R. Petta, Shuttling a single charge across a one-dimensional array of silicon quantum dots, Nature Communications **10**, 10.1038/s41467-019-08970-z (2019).

[6] E. Bocquillon, V. Freulon, F. Parmentier, J. Berroir, B. Plaçais, C. Wahl, J. Rech, T. Jonckheere, T. Martin, C. Grenier, D. Ferraro, P. Degiovanni, and G. Fève, Electron quantum optics in ballistic chiral conductors, Ann. Phys. (Berlin) **526**, 1 (2014).

[7] Proceedings of the 19th meeting of the general conference on weights and measures, `https://www.bipm.org/documents/20126/33145745/CGPM19.pdf/3f65ecf1-f86e-b86c-5c28-709d9f12eec4` (1991).

[8] B. Josephson, Possible new effects in superconductive tunnelling, Physics Letters **1**, 251 (1962).

[9] K. V. Klitzing, G. Dorda, and M. Pepper, New Method for High-Accuracy Determination of the Fine-Structure Constant Based on Quantized Hall Resistance, Phys. Rev. Lett. **45**, 494 (1980).

[10] Proceedings of the 26th meeting of the general conference on weights and measures, `https://www.bipm.org/documents/20126/30876792/CGPM26.pdf/9db96c32-a986-e32a-09f9-3ed7e6c77cf7` (2018).

[11] V. Kashcheyevs, Single-electron turnstile stirring quantized heat flow, Nature Nanotechnology 10.1038/s41565-021-01069-x (2022).

[12] M. Marín-Suárez, J. T. Peltonen, D. S. Golubev, and J. P. Pekola, An electron turnstile for frequency-to-power conversion, Nature Nanotechnology 10.1038/s41565-021-01053-5 (2022).

[13] Truths satellite calibration mission, `https://www.npl.co.uk/earth-observation/truths`.

[14] M. W. Keller, Current status of the quantum metrology triangle, Metrologia **45**, 102 (2008).

[15] R. Landauer, Spatial variation of currents and fields due to localized scatterers in metallic conduction, IBM Journal of Research and Development **1**, 223 (1957).

[16] R. Landauer, Electrical resistance of disordered one-dimensional lattices, The Philosophical Magazine: A Journal of Theoretical Experimental and Applied Physics **21**, 863 (1970), https://doi.org/10.1080/14786437008238472.

[17] M. Y. Azbel, Quantum delta -dimensional landauer formula, Journal of Physics C: Solid State Physics **14**, L225 (1981).
[18] M. Büttiker, Y. Imry, R. Landauer, and S. Pinhas, Generalized many-channel conductance formula with application to small rings, Phys. Rev. B **31**, 6207 (1985).
[19] M. Büttiker, Four terminal phase coherent conductance, Phys. Rev. Lett. **57**, 1761 (1986).
[20] B. Roussel, *Autopsie d'un courant électrique quantique*, Ph.D. thesis, Université de Lyon (2017).
[21] T. Martin and R. Landauer, Wave-packet approach to noise in multichannel mesoscopic systems, Physical Review B **45**, 1742 (1992).
[22] C. Shannon, Communication In The Presence Of Noise, Proceedings of the IEEE **86**, 447 (1998).
[23] J. Dubois, T. Jullien, F. Portier, P. Roche, A. Cavann, Y. Jin, W. Wegscheider, P. Roulleau, and D. C. Glattli, Minimal-excitation states for electron quantum optics using levitons, Nature **502**, 659 (2013).
[24] L. S. Levitov, H. Lee, and G. B. Lesovik, Electron counting statistics and coherent states of electric current, Journal of Mathematical Physics **37**, 4845 (1996), https://doi.org/10.1063/1.531672.
[25] D. A. Ivanov, H. W. Lee, and L. S. Levitov, Coherent states of alternating current, Phys. Rev. B **56**, 6839 (1997).
[26] J. Keeling, I. Klich, and L. Levitov, Minimal excitation states of electrons in one-dimensional wires, Phys. Rev. Lett. **97**, 116403 (2006).
[27] Y. Ji, Y. Chung, D. Sprinzak, M. Heiblum, D. Mahalu, and H. Shtrikman, An electronic mach-zenhder interferometer, Nature **422**, 415 (2003).
[28] B. Roussel, C. Cabart, G. Fève, E. Thibierge, and P. Degiovanni, Electron quantum optics as quantum signal processing, Physica Status Solidi B **254**, 16000621 (2017).
[29] B. Roussel, C. Cabart, G. Fève, and P. Degiovanni, Processing Quantum Signals Carried by Electrical Currents, PRX Quantum **2**, 020314 (2021).
[30] J. Fletcher, P. See, H. Howe, M. Pepper, S. Giblin, J. Griffiths, G. Jones, I. Farrer, D. Ritchie, T. Janssen, *et al.*, Clock-controlled emission of single-electron wave packets in a solid-state circuit, Physical Review Letters **111**, 216807 (2013).
[31] J. Waldie, P. See, V. Kashcheyevs, J. Griffiths, I. Farrer, G. Jones, D. Ritchie, T. Janssen, and M. Kataoka, Measurement and control of electron wave packets from a single-electron source, Physical Review B **92**, 125305 (2015).
[32] J. D. Fletcher, N. Johnson, E. Locane, P. See, J. P. Griffiths, I. Farrer, D. A. Ritchie, P. W. Brouwer, V. Kashcheyevs, and M. Kataoka, Continuous-variable tomography of solitary electrons, Nature Communications **10**, 5298 (2019).
[33] B. Bertrand, S. Hermelin, S. Takada, M. Yamamoto, S. Tarucha, A. Ludwig, A. D. Wieck, C. Bäuerle, and T. Meunier, Fast spin information transfer between distant quantum dots using individual electrons, Nature Nanotechnology **11**, 672 (2016).
[34] H. Flentje, P. A. Mortemousque, R. Thalineau, A. Ludwig, A. D. Wieck, C. Bäuerle, and T. Meunier, Coherent long-distance displacement of individual electron spins, Nature Communications **8**, 501 (2017).
[35] S. Takada, H. Edlbauer, H. V. Lepage, J. Wang, P.-A. Mortemousque, G. Georgiou, C. H. W. Barnes, C. J. B. Ford, M. Yuan, P. V. Santos, X. Waintal, A. Ludwig, A. D. Wieck, M. Urdampilleta, T. Meunier, and C. Bäuerle, Sound-driven single-electron transfer in a circuit of coupled quantum rails, Nature Communications **10**, 4557 (2019).
[36] R. Glauber, Photon correlations, Phys. Rev. Lett. **10**, 84 (1962).
[37] R. Glauber, The quantum theory of optical coherence, Phys. Rev. **130**, 2529 (1963).
[38] R. Glauber, Coherent and incoherent states of the radiation field coherent and incoherent states of the radiation field coherent and incoherent states of the radiation field, Phys. Rev. **131**, 2766 (1963).
[39] G. C. Wick, A. S. Wightman, and E. P. Wigner, The intrinsic parity of elementary particles, Phys. Rev. **88**, 101 (1952).
[40] M. Johansson, Comment on 'Reasonable fermionic quantum information theories require relativity' (2016), arXiv:1610.00539.
[41] A. Abrikosov, L. Gorkov, and I. Dzyaloshinski, *Methods of quantum field theory in statistical physics* (Dover, 1963).
[42] G. Stefanucci and R. van Leeuwem, *Non-equilibrium many-body theory of quantum systems: a modern introduction* (Cambridge University Press, 2013).
[43] J. Rammer, *Quantum transport theory*, Frontiers in Physics (Westview Press, 2004).
[44] M. V. Moskalets, *Scattering Matrix Approach to Non-Stationary Quantum Transport* (Imperial College Press, Singapore, 2011).
[45] K. E. Cahill and R. J. Glauber, Density operators for fermions, Phys. Rev. A **59**, 1538 (1999).
[46] I. Madan, G. M. Vanacore, S. Gargiulo, T. LaGrange, and F. Carbone, The quantum future of microscopy: Wave function engineering of electrons, ions, and nuclei, Applied Physics Letters **116**, 230502 (2020).
[47] S. Asban and F. J. García de Abajo, Generation, characterization, and manipulation of quantum correlations in electron beams, npj Quantum Information **7**, 42 (2021).
[48] A. Marguerite, E. Bocquillon, J.-M. Berroir, B. Plaçais, P. Degiovanni, and G. Fève, Two-particle interferometry in quatum Hall edge channels, Physica Status Solidi B **254**, 1600618 (2017).
[49] N. Ubbelohde, F. Hohls, V. Kashcheyevs, T. Wagner, L. Fricke, B. Kästner, K. Pierz, H. W. Schumacher, and R. J. Haug, Partitioning of on-demand electron pairs, Nature Nanotechnology **10**, 46 (2015).
[50] M. Kataoka, N. Johnson, C. Emary, P. See, J. P. Griffiths, G. A. C. Jones, I. Farrer, D. A. Ritchie, M. Pepper, and T. J. B. M. Janssen, Time-of-flight measurements of single-electron wave packets in quantum hall edge states, Phys. Rev. Lett. **116**, 10.1103/physrevlett.116.126803 (2016).
[51] T. Jullien, P. Roulleau, P. Roche, A. Cavanna, Y. Jin, and D. C. Glattli, Quantum tomography of an electron, Nature **514**, 603 (2014).
[52] R. Bisognin, A. Marguerite, B. Roussel, M. Kumar, C. Cabart, C. Chapdelaine, A. Mohammad-Djafari, J. M. Berroir,

E. Bocquillon, B. Plaçais, A. Cavanna, U. Gennser, Y. Jin, P. Degiovanni, and G. Fève, Quantum tomography of electrical currents, Nature Communications **10**, 3379 (2019).
[53] E. Thibierge, D. Ferraro, B. Roussel, C. Cabart, A. Marguerite, G. Fève, and P. Degiovanni, Two-electron coherence and its measurement in electron quantum optics, Phys. Rev. B **93**, 081302(R) (2016).
[54] A. Einstein, Quantentheorie der einatomigen idealen gases, Sitz. Ber. Preuss. Akad. Wiss. , 18 (1925).
[55] G. Lesovik, Excess quantum noise in 2d ballistic point contacts, JETP Letters **49**, 592 (1989).
[56] A. Kumar, L. Saminadayar, D. Glattli, Y. Jin, and B. Etienne, Experimental test of the quantum shot noise reduction theory, Phys. Rev. Lett. **76**, 2778 (1996).
[57] D. Ferraro, A. Feller, A. Ghibaudo, E. Thibierge, E. Bocquillon, G. Fève, C. Grenier, and P. Degiovanni, Wigner function approach to single electron coherence in quantum Hall edge channels, Phys. Rev. B **88**, 205303 (2013).
[58] E. Wigner, On the quantum correction for thermodynamic equilibrium, Phys. Rev. **40**, 749 (1932).
[59] J. Ville, Théorie et applications de la notion de signal analytique, Câbles et Transmission **2**, 61 (1948).
[60] N. Balazs and B. Jennings, Wigner's function and other distribution functions in mock phase spaces, Physics Reports **104**, 347 (1984).
[61] W. B. Case, Wigner functions and Weyl transforms for pedestrians, American Journal of Physics **76**, 937 (2008).
[62] E. Locane, P. W. Brouwer, and V. Kashcheyevs, Time-energy filtering of single electrons in ballistic waveguides, New Journal of Physics **21**, 093042 (2019), arXiv:arXiv:1901.08940.
[63] J. Ziman, *Principles of the theory of solids* (Cambridge University Press, 1972).
[64] J. Singleton, *Band theory and electronic properties of solids* (Oxford University Press, 2001).
[65] N. Marzari, A. A. Mostofi, J. R. Yates, I. Souza, and D. Vanderbilt, Maximally localized Wannier functions: Theory and applications, Rev. Mod. Phys. **84**, 1419 (2012).
[66] G. Wannier, The structure of electronic excitation levels in insulating crystal, Physical Review **52**, 191 (1937).
[67] Y. Yin, Quasiparticle states of on-demand coherent electron sources, J. Phys.: Condens. Matter **31**, 245301 (2019).
[68] Y. Meir and N. Wingreen, Landauer formula for the current through an interacting electron region, Phys. Rev. Lett. **68**, 2512 (1992).
[69] N. S. Wingreen, A.-P. Jauho, and Y. Meir, Time-dependent transport through a mesoscopic structure, Phys. Rev. B **48**, 8487 (1993).
[70] A. Jauho, N. Wingreen, and Y. Migal, Time-dependent transport in interacting and noninteracting resonant-tunnelling systems, Phys. Rev. B **50**, 5528 (1994).
[71] M. Buttiker, Scattering theory of current and intensity noise correlations in conductors and wave guides, Phys. Rev. B **46**, 12485 (1992).
[72] M. Büttiker, A. Prêtre, and H. Thomas, Dynamic conductance and the scattering matrix of small conductors, Phys. Rev. Lett. **70**, 4114 (1993).
[73] A. Prêtre, H. Thomas, and M. Büttiker, Dynamics admittance of mesoscopic conductors: discrete potential model, Phys. Rev. B **54**, 8130 (1996).
[74] Y. Blanter and M. Buttiker, Shot noise in mesoscopic conductors, Physics Reports **336**, 1 (2000).
[75] C. W. J. Beenakker, P. Jacquod, A. N. Jordan, and P. Samuelsson, eds., *Frontiers in quantum electronic transport - In memory of Markus Büttiker*, Physica E: Low-dimensional Systems and Nanostructures, Vol. 82 (Elsevier, 2016).
[76] J. Gabelli, G. Fève, J. Berroir, B. Plaçais, A. Cavanna, B. Etienne, Y. Jin, and D. Glattli, Violation of kirchhoff's laws for a coherent rc circuit, Science **313**, 499 (2006).
[77] J. Gabelli, G. Fève, T. Kontos, J.-M. Berroir, B. Plaçais, D. C. Glattli, B. Etienne, Y. Jin, and M. Büttiker, Relaxation time of a chiral quantum r-l circuit, Phys. Rev. Lett. **98**, 166806 (2007).
[78] G. Fève, A. Mahé, J. Berroir, T. Kontos, B. Plaçais, D. C. Glattli, A. Cavanna, B. Etienne, and Y. Jin, An on-demand single electron source, Science **316**, 1169 (2007).
[79] F. D. Parmentier, E. Bocquillon, J.-M. Berroir, D. Glattli, B. Plaçais, G. Fève, M. Albert, C. Flindt, and M. Büttiker, Current noise spectrum of a single-particle emitter: Theory and experiment, Phys. Rev. B **85**, 165438 (2012).
[80] D. Ferraro, B. Roussel, C. Cabart, E. Thibierge, G. Fève, C. Grenier, and P. Degiovanni, Real-time decoherence of Landau and Levitov quasiparticles in quantum Hall edge channels, Phys. Rev. Lett. **113**, 166403 (2014).
[81] M. Devoret, D. Esteve, H. Grabert, G.-L. Ingold, H. Pothier, and C. Urbina, Effect of the electromagnetic environment on the coulomb blockade in ultrasmall tunnel junctions, Phys. Rev. Lett. **64**, 1824 (1990).
[82] G.-L. Ingold and Y. Nazarov, Single charge tunneling (Plenum Press, New York, 1992) Chap. Charge tunneling rates in ultrasmall junctions, pp. 21–107.
[83] S. Girvin, L. Glazman, M. Jonson, D. Penn, and M. Stiles, Quantum fluctuations and the single junction coulomb blockade, Phys. Rev. Lett. **64**, 3183 (1990).
[84] C. Altimiras, F. Portier, and P. Joyez, Interacting electrodynamics of short coherent conductors in quantum circuits, Phys. Rev. X **6**, 031002 (2016).
[85] E. Bettelheim and L. Glazman, Quantum ripples over a semiclassical shock, Phys. Rev. Lett. **109**, 260602 (2012).
[86] M. Moskalets and M. Büttiker, Floquet scattering theory of quantum pumps, Phys. Rev. B **66**, 205320 (2002).
[87] M. Moskalets and M. Büttiker, Time-resolved noise of adiabatic quantum pumps, Phys. Rev. B **75**, 035315 (2007).
[88] M. Moskalets, P. Samuelsson, and M. Büttiker, Quantized dynamics of a coherent capacitor, Phys. Rev. Lett. **100**, 086601 (2008).
[89] M. Moskalets, G. Haack, and M. Büttiker, Single-electron source: Adiabatic versus nonadiabatic emission, Phys. Rev. B **87**, 125429 (2013).
[90] M. Moskalets, Noise of a single-electron emitter, Phys. Rev. B **88**, 035433 (2013).

[91] M. Moskalets, Two-electron state from the Floquet scattering matrix perspective, Phys. Rev. B **89**, 045402 (2014).
[92] C. Grenier, J. Dubois, T. Jullien, P. Roulleau, D. C. Glattli, and P. Degiovanni, Fractionalization of minimal excitations in integer quantum hall edge channels, Phys. Rev. B **88**, 085302 (2013).
[93] G. Haack, M. Moskalets, J. Splettstoesser, and M. Büttiker, Coherence of single-electron sources from Mach-Zehnder interferometry, Phys. Rev. B **84**, 081303(R) (2011).
[94] C. Altimiras, H. le Sueur, U. Gennser, A. Cavanna, D. Mailly, and F. Pierre, Non-equilibrium edge channel spectroscopy in the integer quantum Hall regime, Nature Physics **6**, 34 (2010).
[95] C. Hong, Z. Ou, and L. Mandel, Measurement of subpicosecond time intervals between two photons by interference, Phys. Rev. Lett. **59**, 2044 (1987).
[96] F. Bouchard, A. Sit, Y. Zhang, R. Fickler, F. M. Miatto, Y. Yao, F. Sciarrino, and E. Karimi, Two-photon interference: the hong–ou–mandel effect, Reports on Progress in Physics **84**, 012402 (2021).
[97] R. Lopes, A. Imanaliev, A. Aspect, M. Cheneau, D. Boiron, and C. I. Westbrook, Atomic hong-ou-mandel experiment, Nature **520**, 66 (2015).
[98] E. Bocquillon, V. Freulon, J.-M. Berroir, P. Degiovanni, B. Plaçais, A. Cavanna, Y. Jin, and G. Fève, Coherence and indistinguishability of single electrons emitted by independent sources, Science **339**, 1054 (2013).
[99] E. Bocquillon, F. Parmentier, C. Grenier, J.-M. Berroir, P. Degiovanni, D. Glattli, B. Plaçais, A. Cavanna, Y. Jin, and G. Fève, Electron quantum optics: partitioning electrons one by one, Phys. Rev. Lett. **108**, 196803 (2012).
[100] H. A. Fertig and B. I. Halperin, Transmission coefficient of an electron through a saddle-point potential in a magnetic field, Phys. Rev. B **36**, 7969 (1987).
[101] E. Pavlovska, P. G. Silvestrov, P. Recher, G. Barinovs, and V. Kashcheyevs, Collision of two interacting electrons on a mesoscopic beamsplitter: exact solution in the classical limit, arXiv:2201.13439 (2022).
[102] R. Feynman and F. Vernon, The theory of a general quantum system interacting with a linear dissipative system, Annals of Physics **24**, 118 (1963).
[103] M. A. Schlosshauer, *Decoherence and the quantum to classical transition*, The Frontiers Collection (Springer, 2008).
[104] U. Weiss, *Quantum Dissipative Systems* (World Scientific, 1999).
[105] P. Degiovanni, N. Portier, C. Cabart, A. Feller, and B. Roussel, *Physique quantique, information et calcul : des concepts aux applications*, edited by M. Leduc, Savoirs Actuels (EDP Sciences, 2020).
[106] G. Fève, P. Degiovanni, and T. Jolicoeur, Quantum detection of electronic flying qubits in the integer quantum hall regime, Phys. Rev. B **77**, 035308 (2008).
[107] B. Yurke, Quantum network theory, Phys. Rev. A **29**, 1419 (1984).
[108] C. Emary, L. A. Clark, M. Kataoka, and N. Johnson, Energy relaxation in hot electron quantum optics via acoustic and optical phonon emission, Phys. Rev. B **99**, 045306 (2019).
[109] L. A. Clark, M. Kataoka, and C. Emary, Mitigating decoherence in hot electron interferometry, New Journal of Physics **22**, 103031 (2020).
[110] H. Le Sueur, C. Altimiras, U. Gennser, A. Cavanna, D. Mailly, and F. Pierre, Energy relaxation in the integer quantum hall regime, Phys. Rev. Lett. **105**, 056803 (2010).
[111] D. Pines and P. Nozières, *The theory of quantum liquids* (Perseus Book, 1966).
[112] P. Degiovanni, C. Grenier, and G. Fève, Decoherence and relaxation of single electron excitations in quantum Hall edge channels, Phys. Rev. B **80**, 241307(R) (2009).
[113] C. Cabart, B. Roussel, G. Fève, and P. Degiovanni, Taming electronic decoherence in 1d chiral ballistic quantum conductors, Phys. Rev. B **98**, 155302 (2018).
[114] A. Marguerite, C. Cabart, C. Wahl, B. Roussel, V. Freulon, D. Ferraro, C. Grenier, J. M. Berroir, B. Placais, T. Jonckheere, J. Rech, T. Martin, P. Degiovanni, A. Cavanna, Y. Jin, and G. Fève, Decoherence and relaxation of a single electron in a one-dimensional conductor, Phys. Rev. B **94**, 115311 (2016).
[115] I. Levkivskyi and E. Sukhorukov, Dephasing in the electronic mach-zehnder interferometer at filling factor $\nu = 2$, Phys. Rev. B **78**, 045322 (2008).
[116] C. Wahl, J. Rech, T. Jonckheere, and T. Martin, Interactions and charge fractionalization in an electronic Hong-Ou-Mandel interferometer, Phys. Rev. Lett. **112**, 046802 (2014).
[117] D. S. Wei, T. van der Sar, J. D. Sanchez-Yamagishi, K. Watanabe, T. Taniguchi, P. Jarillo-Herrero, B. I. Halperin, and A. Yacoby, Mach-zehnder interferometry using spin- and valley-polarized quantum hall edge states in graphene, Science advances **3**, e1700600 (2017).
[118] C. Altimiras, H. Le Sueur, U. Gennser, A. Cavanna, D. Mailly, and F. Pierre, Tuning energy relaxation along quantum hall edge channels, Phys. Rev. Lett. **105**, 226804 (2010).
[119] P.-A. Huynh, F. Portier, H. le Sueur, G. Faini, U. Gennser, D. Mailly, F. Pierre, W. Wegschider, and P. Roche, Quantum coherence engineering in the integer quantum hall regime, Phys. Rev. Lett. **108**, 256802 (2012).
[120] H. Duprez, E. Sivre, A. Anthore, A. Aassime, A. Cavanna, A. Ouerghi, U. Gennser, and F. Pierre, Macroscopic electron quantum coherence in a solid-state circuit, Phys. Rev. X **9**, 021030 (2019).
[121] M. D. Blumenthal, B. Kaestner, L. Li, S. Giblin, T. Janssen, M. Pepper, D. Anderson, G. Jones, and D. Ritchie, Gigahertz quantized charge pumping, Nature Physics **3**, 343 (2007).
[122] G. Fève, A. Mahé, J.-M. Berroir, T. Kontos, B. Plaçais, D. C. Glattli, A. Cavanna, B. Etienne, and Y. Jin, An on-demand coherent single-electron source, Science **316**, 1169 (2007).
[123] C. Grenier, R. Hervé, E. Bocquillon, F. Parmentier, B. Plaçais, J. Berroir, G. Fève, and P. Degiovanni, Single electron quantum tomography in quantum Hall edge channels, New Journal of Physics **13**, 093007 (2011).
[124] J. Keeling, A. Shytov, and L. Levitov, Coherent particle transfer in an on-demand single-electron source, Phys. Rev. Lett.

101, 196404 (2008).
[125] K. Kobayashi and M. Hashisaka, Shot noise in mesoscopic systems: From single particles to quantum liquids, Journal of the Physical Society of Japan **90**, 102001 (2021).
[126] V. Freulon, A. Marguerite, J. Berroir, B. Plaçais, A. Cavanna, Y. Jin, and G. Fève, Hong-Ou-Mandel experiment for temporal investigation of single-electron fractionalization, Nature Communications **6**, 6854 (2015).
[127] B. Kaestner, V. Kashcheyevs, S. Amakawa, L. Li, M. D. Blumenthal, T. J. B. M. Janssen, G. Hein, K. Pierz, T. Weimann, U. Siegner, and H. W. Schumacher, Single-parameter nonadiabatic quantized charge pumping, Physical Review B **77**, 153301 (2008).
[128] S. Giblin, M. Kataoka, J. Fletcher, P. See, T. Janssen, J. Griffiths, G. Jones, I. Farrer, and D. Ritchie, Towards a quantum representation of the ampere using single electron pumps, Nature communications **3**, 1 (2012).
[129] B. Kaestner, V. Kashcheyevs, G. Hein, K. Pierz, U. Siegner, and H. W. Schumacher, Robust single-parameter quantized charge pumping, Appl. Phys. Lett. **92**, 192106 (2008).
[130] B. Kaestner and V. Kashcheyevs, Non-adiabatic quantized charge pumping with tunable-barrier quantum dots: a review of current progress, Rep. Prog. Phys. **78**, 103901 (2015).
[131] F. Stein, H. Scherer, T. Gerster, R. Behr, M. Götz, E. Pesel, C. Leicht, N. Ubbelohde, T. Weimann, K. Pierz, H. W. Schumacher, and F. Hohls, Robustness of single-electron pumps at sub-ppm current accuracy level, Metrologia **54**, S1 (2016).
[132] S. P. Giblin, E. Mykkänen, A. Kemppinen, P. Immonen, A. Manninen, M. Jenei, M. Möttönen, G. Yamahata, A. Fujiwara, and M. Kataoka, Realisation of a quantum current standard at liquid helium temperature with sub-ppm reproducibility, Metrologia **57**, 025013 (2020).
[133] N. Maire, F. Hohls, B. Kaestner, K. Pierz, H. W. Schumacher, and R. J. Haug, Noise measurement of a quantized charge pump, Applied Physics Letters **92**, 082112 (2008).
[134] M. Kataoka, J. D. Fletcher, and N. Johnson, Time-resolved single-electron wave-packet detection, physica status solidi (b) **254**, 1600547 (2017), https://onlinelibrary.wiley.com/doi/pdf/10.1002/pssb.201600547.
[135] N. Johnson, J. D. Fletcher, D. A. Humphreys, P. See, J. P. Griffiths, G. A. C. Jones, I. Farrer, D. A. Ritchie, M. Pepper, T. J. B. M. Jannsen, and M. Kataoka, Ultrafast voltage sampling using single-electron wavepackets, Appl. Phys. Lett. **110**, 102105 (2017).
[136] C. Leicht, P. Mirovsky, B. Kaestner, F. Hohls, V. Kashcheyevs, E. V. Kurganova, U. Zeitler, T. Weimann, K. Pierz, and H. W. Schumacher, Generation of energy selective excitations in quantum hall edge states, Semiconductor Science and Technology **26**, 055010 (2011).
[137] V. Kashcheyevs and P. Samuelsson, Classical-to-quantum crossover in electron on-demand emission, Physical Review B **95**, 245424 (2017), arXiv:1701.02637.
[138] R. H. Hadfield, Single-photon detectors for optical quantum information applications, Nat. Photonics **3**, 696 (2009).
[139] C. J. Chunnilall, I. P. Degiovanni, S. Kück, I. Müller, and A. G. Sinclair, Metrology of single-photon sources and detectors: a review, Optical Engineering **53**, 081910 (2014).
[140] K. Laiho, T. Dirmeier, M. Schmidt, S. Reitzenstein, and C. Marquardt, Measuring higher-order photon correlations of faint quantum light: a short review, arXiv:2109.01437 [quant-ph] (2021), arXiv: 2109.01437 version: 1.
[141] L. Freise, T. Gerster, D. Reifert, T. Weimann, K. Pierz, F. Hohls, and N. Ubbelohde, Trapping and counting ballistic nonequilibrium electrons, Physical Review Letters **124**, 127701 (2020).
[142] R. Thalineau, A. D. Wieck, C. Bäuerle, and T. Meunier, Using a two-electron spin qubit to detect electrons flying above the Fermi sea, arXiv:1403.7770 (2014).
[143] D. C. Glattli, J. Nath, I. Taktak, P. Roulleau, C. Bauerle, and X. Waintal, Design of a single-shot electron detector with sub-electron sensitivity for electron flying qubit operation, arXiv:2002.03947 (2020).
[144] T. Ota, S. Akiyama, M. Hashisaka, K. Muraki, and T. Fujisawa, Spectroscopic study on hot-electron transport in a quantum hall edge channel, Phys. Rev. B **99**, 085310 (2019).
[145] L. Fricke, M. Wulf, B. Kaestner, V. Kashcheyevs, J. Timoshenko, P. Nazarov, F. Hohls, P. Mirovsky, B. Mackrodt, R. Dolata, T. Weimann, K. Pierz, and H. W. Schumacher, Counting statistics for electron capture in a dynamic quantum dot, Physical Review Letters **110**, 126803 (2013).
[146] D. Reifert, M. Kokainis, A. Ambainis, V. Kashcheyevs, and N. Ubbelohde, A random-walk benchmark for single-electron circuits, Nature Communications **12**, 10.1038/s41467-020-20554-w (2021).
[147] M. Jo, P. Brasseur, A. Assouline, G. Fleury, H.-S. Sim, K. Watanabe, T. Taniguchi, W. Dumnernpanich, P. Roche, D. C. Glattli, N. Kumada, F. D. Parmentier, and P. Roulleau, Quantum hall valley splitters and a tunable mach-zehnder interferometer in graphene, Phys. Rev. Lett. **126**, 146803 (2021).
[148] W. Poirier, S. Djordjevic, F. Schopfer, and O. Thévenot, The ampere and the electrical units in the quantum era, C. R. Physique **20**, 92 (2019).
[149] R. Ribeiro-Palau, F. Lafont, J. Brun-Picard, D. Kazazis, A. Michon, F. Cheynis, O. Couturaud, C. Consejo, B. Jouault, W. Poirier, and F. Schopfer, Quantum hall resistance standard in graphene devices under relaxed experimental conditions, Nature Nano. **10**, 965 (2015).
[150] M. E. Cage, R. F. Dziuba, B. F. Field, E. R. Williams, S. M. Girvin, A. C. Gossard, D. C. Tsui, and R. J. Wagner, Dissipation and dynamic nonlinear behavior in the quantum hall regime, Phys. Rev. Lett. **51**, 1374 (1983).
[151] A. Assouline, M. Jo, P. Brasseur, K. Watanabe, T. Taniguchi, T. Jolicoeur, N. Glattli, D. C.and Kumada, P. Roche, F. D. Parmentier, and P. Roulleau, Excitonic nature of magnons in a quantum hall ferromagnet, Nature Physics **17**, 1374 (2021).
[152] W. Poirier and F. Schopfer, Resistance metrology based on the quantum hall effect, Eur. Phys. J. Spec. Top. **172**, 207

(2009).
[153] M. Buttiker, Absence of backscattering in the quantum hall effect in multiprobe conductors, Phys. Rev. B **38**, 9375 (1988).
[154] N. V. Lien, Sov. Phys. Semicond. **18**, 207 (1984).
[155] B. I. Shklovskii and A. L. Efros, *Electronic properties of Doped semiconductors* (Springer, 1984).
[156] F. Lafont, R. Ribeiro-Palau, D. Kazazis, A. Michon, O. Couturaud, C. Consejo, T. Chassagne, M. Zielinski, M. Portail, B. Jouault, F. Schopfer, and W. Poirier, Quantum hall resistance standards from graphene grown by chemical vapour deposition on silicon carbide, Nature Communications **6**, 6806 (2015).
[157] J. Brun-Picard, *Une nouvelle génération d'étalons quantiques fondés sur l'effet Hall quantique*, Ph.D. thesis, Paris-Sud, Paris-Saclay, Orsay (2018).
[158] T. J. B. M. Janssen, A. Tzalenchuk, R. Yakimova, S. Kubatkin, S. Lara-Avila, S. Kopylov, and V. I. Falko, Anomalously strong pinning of the filling factor $\nu = 2$ in epitaxial graphene, Phys. Rev. B **83**, 233402 (2011).
[159] M. Furlan, Electronic transport and the localization length in the quantum hall effect, Phys. Rev. B **57**, 14818 (1998).
[160] B. Jeckelmann and B. Jeanneret, The quantum hall effect as an electrical resistance standard, Rep. Prog. Phys. **64**, 1603 (2001).
[161] W. Poirier, D. Leprat, and F. Schopfer, A resistance bridge based on a cryogenic current comparator achieving sub-10^{-9} measurement uncertainties, IEEE Trans. Instrum. Meas. **70**, 1000314 (2021).
[162] F. Delahaye and B. Jeckelmann, Revised technical guidelines for reliable dc measurements of the quantized hall resistance, Metrologia **40**, 217 (2003).
[163] B. W. Alphenaar, P. L. McEuen, and R. G. Wheeler, Selective equilibration among the current-carrying states in the quantum hall regime, Phys. Rev. Lett. **64**, 677 (1990).
[164] S. Komiyama, H. Hirai, M. Ohsawa, Y. Matsuda, and S. Sasa, Inter-edge-state scattering and nonlinear effects in a two-dimensional electron gas at high magnetic fields, Phys. Rev. B **45**, 11085 (1992).
[165] C. Chaubet, A. Raymond, and D. Dur, Heating of two-dimensional electrons by a high electric field in a quantizing magnetic field: Consequences in landau emission and in the quantum hall effect, Phys. Rev. B **52**, 11178 (1995).
[166] C. Chaubet and F. Geniet, Nonequilibrium occupation of landau levels and universal critical field in the quantum-hall-effect breakdown, Phys. Rev. B **58**, 13015 (1998).
[167] J. Guignard, D. Leprat, D. C. Glattli, F. Schopfer, and W. Poirier, Quantum hall effect in exfoliated graphene affected by charged impurities: Metrological measurements, Phys. Rev. B **85**, 165420 (2012).
[168] P. Roulleau, F. Portier, D. Glattli, P. Roche, A. Cavanna, G. Faini, U. Gennser, and D. Mailly, Finite bias visibility of the electronic mach-zehnder interferometer, Phys. Rev. B **76**, 161309 (2007).
[169] X. K. Yue and Y. Yin, Normal and anomalous electron-hole pairs in a quantum conductor driven by a voltage pulse, Phys. Rev. B **99**, 235431 (2019).
[170] B. I. Halperin, A. Stern, I. Neder, and B. Rosenow, Theory of the fabry-pérot quantum hall interferometer, Phys. Rev. B **83**, 155440 (2011).